

<sup>1</sup> SEARCH FOR EXOTIC HIGGS DECAYS TO LIGHT  
<sup>2</sup> NEUTRAL SCALARS IN FINAL STATES WITH  
<sup>3</sup> BOTTOM QUARKS AND TAU LEPTONS

<sup>4</sup> KA YU STEPHANIE KWAN

<sup>5</sup> A DISSERTATION  
<sup>6</sup> PRESENTED TO THE FACULTY  
<sup>7</sup> OF PRINCETON UNIVERSITY  
<sup>8</sup> IN CANDIDACY FOR THE DEGREE  
<sup>9</sup> OF DOCTOR OF PHILOSOPHY

<sup>10</sup> NOT YET RECOMMENDED FOR ACCEPTANCE  
<sup>11</sup> BY THE DEPARTMENT OF PHYSICS  
<sup>12</sup> ADVISER: ISOBEL OJALVO

<sup>13</sup> MAY 2024

<sup>14</sup>

© Copyright by Ka Yu Stephanie Kwan, 2024.

<sup>15</sup>

All Rights Reserved

## Abstract

Open questions in particle physics may be addressed by the existence of an extended Higgs sector beyond the Standard Model Higgs boson with mass 125 GeV, which was discovered in 2012 at the Large Hadron Collider (LHC) by the CMS and ATLAS experiments. Many properties of a potential extended Higgs sector remain unconstrained by current measurements, making direct searches of exotic Higgs decays a powerful probe of new physics. The decay of the 125 GeV Higgs boson into two light neutral scalar particles ( $h \rightarrow aa$ ) is allowed in extensions of the Standard Model, such as Two Higgs Doublet Models extended with a scalar singlet (2HDM+S). We present a search at CMS for exotic decays of the 125 GeV Higgs boson to two light neutral scalars, which decay to two bottom quarks and two tau leptons ( $h \rightarrow aa \rightarrow bb\tau\tau$ ). This analysis is combined with a different search where the light scalars decay to two bottom quarks and two muons. The results from the  $bb\tau\tau$  analysis and the combined analyses are interpreted in 2HDM+S scenarios. In a different extension of the Standard Model, the Two Real Singlet Model (TRSM), the 125 GeV Higgs boson can decay to two light scalars with unequal mass ( $h \rightarrow a_1a_2$ ). This decay has not been searched for to date at CMS. We present ongoing work on a search for  $h \rightarrow a_1a_2$ , where the  $a_2$  decays into two  $a_1$ , resulting in four bottom quarks and two tau leptons in the final state, in the  $\mu\tau_h$  channel of the  $\tau\tau$  decay. Such searches for rare processes will directly benefit from the increased datasets that will be generated by the High-Luminosity LHC (HL-LHC), which is scheduled to increase the LHC’s number of simultaneous proton-proton collisions by a factor of five to seven. To contribute to the performance of the CMS Level-1 Trigger in selecting collisions with interesting physics, this thesis presents an upgraded algorithm for reconstructing electrons and photons in the barrel calorimeter, which will use information with higher spatial granularity to distinguish genuine electrons and photons from background.

<sup>42</sup>

## Acknowledgements

<sup>43</sup> Placeholder acknowledgements.



# <sup>45</sup> Contents

<sup>46</sup>	Abstract . . . . .	iii
<sup>47</sup>	Acknowledgements . . . . .	iv
<sup>48</sup>	List of Tables . . . . .	xi
<sup>49</sup>	List of Figures . . . . .	xv
<sup>50</sup>	<b>1 Introduction</b>	<b>1</b>
<sup>51</sup>	1.1 History of the Standard Model . . . . .	1
<sup>52</sup>	1.2 The Standard Model as a gauge theory . . . . .	3
<sup>53</sup>	1.3 The Higgs Mechanism . . . . .	6
<sup>54</sup>	1.4 Two-Higgs Doublet Models . . . . .	8
<sup>55</sup>	1.5 Two Real Singlet Model . . . . .	11
<sup>56</sup>	<b>2 The Large Hadron Collider and the CMS Experiment</b>	<b>15</b>
<sup>57</sup>	2.1 The Large Hadron Collider . . . . .	16
<sup>58</sup>	2.2 Luminosity and pile-up . . . . .	17
<sup>59</sup>	2.3 The High-Luminosity LHC . . . . .	20
<sup>60</sup>	2.4 The CMS Detector . . . . .	21
<sup>61</sup>	2.5 Sub-detectors of CMS . . . . .	23
<sup>62</sup>	2.5.1 Inner tracking system . . . . .	23
<sup>63</sup>	2.5.2 ECAL . . . . .	24
<sup>64</sup>	2.5.3 HCAL . . . . .	25

65	2.5.4 Muon detectors . . . . .	27
66	2.5.5 The Level-1 Trigger . . . . .	28
67	2.5.6 The High-Level Trigger . . . . .	32
68	2.5.7 Particle reconstruction . . . . .	33
69	2.5.8 Data storage and computational infrastructure . . . . .	33
70	<b>3 The Phase-2 Upgrade of CMS</b>	<b>35</b>
71	3.1 The High-Luminosity LHC . . . . .	35
72	3.2 The Phase-2 Level-1 Trigger . . . . .	36
73	3.3 Standalone Barrel Calorimeter electron/photon reconstruction . . . . .	39
74	3.3.1 Electron/photon standalone barrel procedure . . . . .	39
75	3.3.2 Electron/photon standalone barrel results . . . . .	44
76	<b>4 Datasets and Monte Carlo samples</b>	<b>48</b>
77	4.1 Datasets used . . . . .	48
78	4.2 Monte Carlo samples . . . . .	49
79	4.3 Embedded samples . . . . .	50
80	<b>5 Object reconstruction and corrections applied</b>	<b>53</b>
81	5.1 Object reconstruction . . . . .	54
82	5.1.1 Taus . . . . .	54
83	5.1.2 Muons . . . . .	57
84	5.1.3 Electrons . . . . .	58
85	5.1.4 Jets . . . . .	60
86	5.1.5 B-flavored jets . . . . .	61
87	5.2 Reconstruction of the di-tau mass . . . . .	62
88	5.2.1 Original SVFit “standalone”: maximum likelihood . . . . .	63
89	5.2.2 “Classic SVFit” with matrix element . . . . .	64
90	5.2.3 FastMTT: optimized SVFit . . . . .	64

91	5.3 Corrections applied to simulation . . . . .	65
92	5.3.1 Tau energy scale . . . . .	66
93	5.3.2 Muon energy scale . . . . .	67
94	5.3.3 Electron energy scale . . . . .	67
95	5.3.4 $\tau_h$ identification efficiency . . . . .	67
96	5.3.5 Trigger efficiencies . . . . .	68
97	5.3.6 Tau trigger efficiencies . . . . .	69
98	5.3.7 Single muon trigger efficiencies . . . . .	70
99	5.3.8 Single electron trigger efficiencies . . . . .	71
100	5.3.9 $e\mu$ cross-trigger efficiencies . . . . .	72
101	5.3.10 Electrons and muons faking $\tau_h$ : energy scales . . . . .	73
102	5.3.11 Electrons and muons faking $\tau_h$ : misidentification efficiencies .	74
103	5.3.12 Electron ID and tracking efficiency . . . . .	75
104	5.3.13 Muon ID, isolation, and tracking efficiencies . . . . .	75
105	5.3.14 Recoil corrections . . . . .	77
106	5.3.15 Drell-Yan corrections . . . . .	78
107	5.3.16 Pile-up reweighing . . . . .	78
108	5.3.17 Pre-firing corrections . . . . .	79
109	5.3.18 Top $p_T$ spectrum reweighing . . . . .	79
110	5.3.19 B-tagging efficiency . . . . .	79
111	5.3.20 Jet energy resolution and jet energy smearing . . . . .	80
112	<b>6 Event selection</b>	<b>81</b>
113	6.1 General procedure for all channels . . . . .	81
114	6.2 Event selection in the $\mu\tau_h$ channel . . . . .	83
115	6.3 Event selection in the $e\tau_h$ channel . . . . .	85
116	6.4 Event selection in the $e\mu$ channel . . . . .	87
117	6.5 Extra lepton vetoes in all channels . . . . .	88

<sup>118</sup>	<b>7 Background estimation</b>	<b>91</b>
<sup>119</sup>	7.1 Z+jets . . . . .	91
<sup>120</sup>	7.2 W+jets . . . . .	92
<sup>121</sup>	7.3 $t\bar{t}$ + jets . . . . .	92
<sup>122</sup>	7.4 Single top . . . . .	93
<sup>123</sup>	7.5 Diboson . . . . .	93
<sup>124</sup>	7.6 Standard Model Higgs . . . . .	93
<sup>125</sup>	7.7 Jet faking $\tau_h$ . . . . .	94
<sup>126</sup>	7.8 QCD multijet background . . . . .	95
<sup>127</sup>	<b>8 Systematic uncertainties</b>	<b>97</b>
<sup>128</sup>	8.1 Uncertainties in the lepton energy scales . . . . .	98
<sup>129</sup>	8.2 Uncertainties from other lepton corrections . . . . .	99
<sup>130</sup>	8.3 Uncertainties from jet energy scale and resolution . . . . .	100
<sup>131</sup>	8.4 Uncertainties from b-tagging scale factors . . . . .	101
<sup>132</sup>	8.5 Uncertainties from MET . . . . .	101
<sup>133</sup>	8.6 Uncertainties associated with samples used . . . . .	102
<sup>134</sup>	8.7 Other uncertainties . . . . .	102
<sup>135</sup>	8.8 Pulls and impacts . . . . .	103
<sup>136</sup>	<b>9 Event categorization and signal extraction</b>	<b>105</b>
<sup>137</sup>	9.1 B-tag jet multiplicity . . . . .	105
<sup>138</sup>	9.2 DNN-based event categorization . . . . .	106
<sup>139</sup>	9.3 Methodology for signal extraction . . . . .	108
<sup>140</sup>	9.3.1 Model building and parameter estimation . . . . .	109
<sup>141</sup>	9.3.2 Hypothesis testing . . . . .	111
<sup>142</sup>	9.3.3 Confidence intervals . . . . .	112
<sup>143</sup>	9.3.4 Profile likelihood ratio . . . . .	113

<sup>144</sup>	9.3.5 Modified frequentist method: $CL_S$	115
<sup>145</sup>	<b>10 Results</b>	<b>116</b>
<sup>146</sup>	10.1 Results from $bb\tau\tau$	116
<sup>147</sup>	10.2 Combination with $bb\mu\mu$ final state	118
<sup>148</sup>	<b>11 Asymmetric exotic Higgs decays</b>	<b>129</b>
<sup>149</sup>	11.1 Signal masses	129
<sup>150</sup>	11.2 Cascade scenario signal studies	130
<sup>151</sup>	11.3 Current control plots for $\mu\tau_h$ channel	132
<sup>152</sup>	<b>12 Conclusion and outlook</b>	<b>136</b>
<sup>153</sup>	<b>A Samples used</b>	<b>138</b>

# <sup>154</sup> List of Tables

<sup>155</sup>	4.1	Expected event composition after selecting two muons in the embedded technique, before additional cuts (i.e. inclusive), and after adding a requirement on the di-muon mass $m_{\mu\mu} > 70$ GeV, or a requirement on the number of b-tag jets in the event. . . . .	52
<sup>156</sup>			
<sup>157</sup>			
<sup>158</sup>			
<sup>159</sup>	5.1	Energy scales applied to genuine hadronic tau decays $\tau_h$ by data-taking year/era and decay mode, along with systematic errors. . . . .	66
<sup>160</sup>			
<sup>161</sup>	5.2	Energy scales and systematic errors applied to genuine muons. . . . .	67
<sup>162</sup>			
<sup>163</sup>	5.3	Energy scales and systematic errors applied to electrons in embedded samples by data-taking year/era. . . . .	67
<sup>164</sup>			
<sup>165</sup>	5.4	Tau ID efficiency for the DeepTau vs. jet medium working point, with central, up, and down values for 2018, binned in the tau $p_T$ . . . . .	68
<sup>166</sup>			
<sup>167</sup>	5.5	Energy scales and up/down systematic uncertainties applied to electrons misidentified as hadronic taus. . . . .	73
<sup>168</sup>			
<sup>169</sup>	5.6	Tau mis-identification efficiency for the DeepTau Tight and Very Loose (VLoose) working points vs. muons in 2018. . . . .	74
<sup>170</sup>			
<sup>171</sup>	5.7	Tau mis-identification efficiency for the DeepTau Tight and Very Loose (VLoose) working points vs. electrons in 2018. . . . .	74

172	6.1	Trigger thresholds used for the leptons in the $bb\mu\mu$ analysis and the 173 $bb\tau\tau$ analysis (the focus of this work). The thresholds for the three $bb\tau\tau$ 174       channels ( $e\mu$ , $e\tau_h$ , and $\mu\tau_h$ ) are listed separately, with some channels 175       and years taking the logical OR of two triggers with different thresholds. . . . .	83
176	6.2	Summary of requirements applied to the leptons in the $bb\mu\mu$ analysis 177       and the $bb\tau\tau$ analysis (the focus of this work). $\Delta R = \sqrt{(\Delta\eta)^2 + (\Delta\phi)^2}$ 178       is a measure of spatial separation. Relative isolation is defined in 179       Eqn. 5.2Muonsequation.5.1.2 and Section 5.1.2Muonssubsection.5.1.2. 180       The b-tag jets are required to pass the listed DeepFlavour working 181       points (WP), which are described in Section 5.1.5B-flavored jetssub- 182       section.5.1.5. In the $bb\tau\tau$ analysis, the required $ \eta $ of the hadronic 183       taus are listed for the single and cross triggers respectively. The $bb\mu\mu$ 184       analysis requires two b-tag jets in all events, while the $bb\tau\tau$ analysis 185       only requires one. . . . .	84
186	6.3	High-Level Trigger (HLT) paths used to select data and simulation 187       events in 2016 for the three $\tau\tau$ channels. . . . .	88
188	6.4	High-Level Trigger (HLT) paths used to select data and simulation 189       events in 2017 for the three $\tau\tau$ channels. . . . .	89
190	6.5	High-Level Trigger (HLT) paths used to select data and simulation 191       events in 2018 for the three $\tau\tau$ channels. In 2018 a HLT trigger path 192       using the hadron plus strips (HPS) tau reconstruction algorithm be- 193       came available. . . . .	90
194	9.1	Event categorization based on DNN scores for events with exactly 1 195       b-tag jet (1bNN), for the three $\tau\tau$ channels and three eras. . . . .	108
196	9.2	Event categorization based on DNN scores for events with 2 b-tag jets 197       (2bNN), for the three $\tau\tau$ channels and three eras. . . . .	109

198	A.1 Data sets used in the $h \rightarrow aa \rightarrow bb\tau\tau$ analysis for the 2016 era. . . . .	139
199	A.2 Data sets used in the $h \rightarrow aa \rightarrow bb\tau\tau$ analysis for the 2017 era. . . . .	140
200	A.3 Data sets used in the $h \rightarrow aa \rightarrow bb\tau\tau$ analysis for the 2018 eras. . . . .	140
201	A.4 Embedded samples used in the analysis for the 2016 era. . . . .	140
202	A.5 Embedded samples used in the analysis for the 2017 era. . . . .	141
203	A.6 Embedded samples used in the analysis for the 2018 era. . . . .	141
204	A.7 Background MC samples used in the analysis for the 2016 era. Samples marked with a $\dagger$ are generated with the powhegV2-madspin-pythia8 tag.	142
205		
206	A.8 Background MC samples used in the analysis for the 2017 era. All samples use powheg, except the DYJets and WJets samples, which use madgraphMLM. Samples marked with a $\dagger$ , $\ddagger$ , or $\ddagger\dagger$ had the tags powhegV2-madspin-pythia8, powheg2_JHUGenV714_pythia8, or powheg_jhugen724_pythia8 respectively. . . . .	143
207		
208		
209		
210		
211	A.9 Background Monte Carlo samples used in the analysis for the 2018 era. All samples listed are generated for 13 TeV collisions and use pythia8. All samples use powheg, except the DYJets and WJets sam- ples, which use madgraphMLM. Samples marked with a $\dagger$ , $\ddagger$ , or $\ddagger\dagger$ , had the tags powhegV2-madspin-pythia8, powheg2_JHUGenV714_pythia8, and powheg_jhugen724_pythia8 respectively. . . . .	144
212		
213		
214		
215		
216		
217	A.10 Signal samples used in the analysis for the 2016 era. All belong to the RunIISummer16MiniAODv3 campaign and are produced with the tags TuneCUETP8M1_13TeV_madgraph_pythia8 PUMoriond17_94X_mcRun2_asymptotic_v3. The second column is the number of events after the generator-level filter is applied, and the third column is the filter efficiency (percentage of all events that pass the generator-level filter). . . . .	145
218		
219		
220		
221		
222		



# <sup>235</sup> List of Figures

236	1.1	Table of Standard Model particles showing the grouping of the fermions		
237		into three generations of matter and the bosons, responsible for carrying		
238		the three fundamental forces in the Standard Model. The masses,		
239		charges, and spins of the particles are shown. The antimatter counter-		
240		parts of the fermions are not shown. The possible interactions between		
241		the fermions and gauge bosons are highlighted. . . . .	3	
242	1.2	An illustration of the Higgs potential. . . . .	8	
243	1.3	Branching ratios of a singlet-like pseudoscalar in Type II 2HDM+S for		
244		$\tan \beta = 0.5$ (left) and $\tan \beta = 5$ (right). . . . .	11	
245	1.4	Benchmark plane BP1 for benchmark scenario 1, for the decay signa-		
246		ture $h_{125} \rightarrow h_1 h_2$ with $h_{125} \equiv h_3$ , defined in the $(M_1, M_2)$ plane. . . .	14	
247	2.1	Aerial view of the Large Hadron Collider (LHC). . . . .	18	
248	2.2	Distribution of the mean number of inelastic collisions per bunch cross-		
249		ing (pile-up) in data, for proton-proton collisions in 2016-2018 . . .	20	
250	2.3	Sketch of particle trajectories of muons, electrons, charged and neutral		
251		hadrons, and photons in a transverse cross-section of the CMS detector.	22	
252	2.4	Cross section of the current Phase-1 CMS tracker. . . . .	24	
253	2.5	Longitudinal view of the CMS detector showing the hadron calorimeter		
254		barrel (HB), endcap (HE), outer (HO), and forward (HF) calorimeters.	26	

255	2.6 Layout of the CMS barrel muon drift tube (DT) chambers in one of	
256	the five wheels. . . . .	28
257	2.7 Dataflow for the Phase-1 Level-1 Trigger. . . . .	29
258	2.8 Schematic of the calorimeter trigger after Long Shutdown 2. The	
259	Layer-1 calorimeter trigger is implemented in CTP7 cards, which send	
260	time-multiplexed outputs to the Layer-2 MP7 cards. The Layer-2	
261	cards handle the data in a round-robin style and the outputs are de-	
262	multiplexed, producing one output data stream to the Global Trigger.	31
263	3.1 Functional diagram of the CMS L1 Phase-2 upgraded trigger design. .	37
264	3.2 Summary of the links between the trigger primitives, the trigger ob-	
265	jects, the Level-1 algorithms, and the physics channels in the Phase-2	
266	menu. . . . .	40
267	3.3 Schematic of the geometry of the Phase-2 ECAL barrel in the Regional	
268	Calorimeter Trigger (RCT), showing the division of the barrel region	
269	into 36 Regional Calorimeter Trigger (RCT) cards ( <i>red</i> ). Each card	
270	spans $17 \times 4$ towers in $\eta \times \phi$ ( <i>green</i> ), and each tower is $5 \times 5$ in single	
271	crystals in $\eta \times \phi$ . Towers in the overlap region ( <i>shaded yellow</i> ) are read	
272	out to both the barrel and endcap. . . . .	41
273	3.4 Schematic of two example RCT cards in the negative eta ( <i>top left</i> )	
274	and positive eta ( <i>bottom left</i> ) regions of the ECAL barrel. Each RCT	
275	card is divided into six regions: five regions are of size $3 \times 4$ towers in	
276	$\eta \times \phi$ ( <i>top right</i> ), and a sixth smaller overlap region of size $2 \times 4$ towers	
277	( <i>bottom right</i> ). Each tower is $5 \times 5$ ( $\eta \times \phi$ ) in crystals. . . . .	42





325	5.3 Hadronic tau leg efficiency of the cross-triggers for $\mu\tau_h$ ( <i>left</i> ) and $e\tau_h$ ( <i>right</i> ) triggers as a function of offline tau $p_T$ for 2016, 2017, and 2018.	70
326		
327	5.4 Trigger efficiencies in data ( <i>top panels</i> ) and ratio of efficiencies af- ter/before a HLT muon reconstruction update ( <i>bottom panels</i> ) for the	
328	muon in the isolated single muon trigger with threshold $p_T > 24$ GeV	
329	in the data-taking year 2018, as functions of the muon $p_T$ ( <i>left</i> ) and	
330	muon $ \eta $ ( <i>right</i> ). . . . .	71
331		
332	5.5 Trigger efficiencies in data and the data/MC ratio for the electron in the single electron trigger with threshold $p_T > 32$ GeV in the data- taking year 2018, as functions of the electron $p_T$ ( <i>left</i> ) and electron $ \eta $ ( <i>right</i> ). . . . .	72
333		
334	5.6 Efficiencies of the electron leg vs. $p_T$ ( <i>left</i> ) and the muon log vs. $\eta$ ( <i>right</i> ), for the HLT path with online thresholds of 12 GeV for the	
335	electron and 23 GeV for the muon, with the data-taking years 2016	
336	through 2018 overlaid. . . . .	73
337		
338	5.7 Efficiencies in data ( <i>top panels</i> ) and the ratio of efficiencies in data/MC ( <i>bottom panels</i> ), for the electron multivariate analysis (MVA) identifi- cation ( <i>left</i> ) and for the Gaussian-sum filter (GSF) tracking ( <i>right</i> ). . .	75
339		
340	5.8 Muon identification efficiencies in 2015 data and MC as a function of	
341	the muon $p_T$ for the loose ID ( <i>left</i> ) and tight ID ( <i>right</i> ) working points.	76
342		
343	5.9 Muon isolation efficiencies in Run-2 data as a function of the muon $p_T$ ( <i>left</i> ) and $ \eta $ ( <i>right</i> ). . . . .	77
344		
345	5.10 Muon tracking efficiencies as a function of $ \eta $ for standalone muons in	
346	Run-2 data ( <i>black</i> ) and Drell-Yan ( <i>blue</i> ) MC simulation. . . . .	78
347		
348	7.1 Leading-order Feynman diagrams of Higgs production. . . . .	94
349		

350	8.1 Top sixty pulls and impacts for the combination of all channels and	
351	years. . . . .	104
352	9.1 Schematic of the Neyman construction for confidence intervals. . . . .	114
353	10.1 Postfit final observed and expected $m_{\tau\tau}$ distributions in the $\mu\tau_h$ chan-	
354	nel, for the 1 b-tag jet and 2 b-tag jet signal and control regions. . . . .	120
355	10.2 Postfit final observed and expected $m_{\tau\tau}$ distributions in the $e\tau_h$ chan-	
356	nel, for the 1 b-tag jet and 2 b-tag jet signal and control regions. . . . .	121
357	10.3 Postfit final observed and expected $m_{\tau\tau}$ distributions in the $e\mu$ channel.	122
358	10.4 Observed 95% CL exclusion limits ( <i>black, solid lines</i> ) and expected 95%	
359	CL and 68% CL limits ( <i>shaded yellow and green</i> ) on the branching	
360	fraction $B(h \rightarrow aa \rightarrow bb\tau\tau)$ in percentages, assuming the Standard	
361	Model production for the 125 GeV Higgs ( $h$ ). Limits are shown for the	
362	$\mu\tau_h$ channel ( <i>top left</i> ), the $e\tau_h$ channel ( <i>top right</i> ), and the $e\mu$ channel	
363	( <i>bottom left</i> ), and lastly the combination of all three channels ( <i>bottom</i>	
364	<i>right</i> ) The dataset corresponds to $138 \text{ fb}^{-1}$ of data collected in the	
365	years 2016-2018 at a center-of-mass energy 13 TeV. . . . .	123
366	10.5 Observed 95% CL upper limits on $B(h \rightarrow aa)$ in %, for the $bb\tau\tau$ final	
367	state ( <i>left</i> ) and $bb\mu\mu$ final state ( <i>right</i> ) using the full Run 2 integrated	
368	luminosity of $138 \text{ fb}^{-1}$ in 2HDM+S type I ( <i>blue</i> ), type II with $\tan\beta =$	
369	$2.0$ ( <i>orange dashed</i> ), type III with $\tan\beta = 2.0$ ( <i>dotted green</i> ), and type	
370	IV with $\tan\beta = 0.6$ ( <i>red dashed</i> ). . . . .	124

371	10.6 Observed 95% CL upper limits on the branching fraction of the 125	
372	GeV Higgs boson to two pseudoscalars, $B(h \rightarrow aa)$ , in percentages,	
373	as a function of the pseudoscalar mass $m_a$ , in 2HDM+S type I ( <i>blue</i> ),	
374	type II with $\tan\beta = 2.0$ ( <i>orange dashed</i> ), type III with $\tan\beta = 2.0$	
375	( <i>dotted green</i> ), and type IV with $\tan\beta = 0.6$ ( <i>red dashed</i> ), for the	
376	combination of $bb\mu\mu$ and $bb\tau\tau$ channels using the full Run 2 integrated	
377	luminosity of $138 \text{ fb}^{-1}$ . . . . .	125
378	10.7 Observed 95% CL upper limits on $\mathcal{B}(h \rightarrow aa)$ in %, for the combination	
379	of $bb\mu\mu$ and $bb\tau\tau$ channels using the full Run 2 integrated luminosity	
380	of $138 \text{ fb}^{-1}$ for Type II ( <i>left</i> ), Type III ( <i>middle</i> ), and Type IV ( <i>right</i> )	
381	2HDM+S in the $\tan\beta$ vs. $m_a$ phase space. . . . .	126
382	10.8 Summary plot of current observed and expected 95% CL limits on the	
383	branching ratio of the 125 GeV Higgs boson to two pseudoscalars, nor-	
384	malized to the Standard Model Higgs production cross-section, $\frac{\sigma(h)}{\sigma_{\text{SM}}} \times$	
385	$B(h \rightarrow aa)$ , in the 2HDM+S type I scenario, obtained at CMS with	
386	data collected at 13 TeV. . . . .	126
387	10.9 Summary plot of current observed and expected 95% CL limits on the	
388	branching ratio of the 125 GeV Higgs boson to two pseudoscalars, nor-	
389	malized to the Standard Model Higgs production cross-section, $\frac{\sigma(h)}{\sigma_{\text{SM}}} \times$	
390	$B(h \rightarrow aa)$ , in the 2HDM+S type II scenario with $\tan\beta = 2.0$ , ob-	
391	tained at CMS with data collected at 13 TeV. . . . .	127
392	10.10 Summary plot of current observed and expected 95% CL limits on the	
393	branching ratio of the 125 GeV Higgs boson to two pseudoscalars, nor-	
394	malized to the Standard Model Higgs production cross-section, $\frac{\sigma(h)}{\sigma_{\text{SM}}} \times$	
395	$B(h \rightarrow aa)$ , in the 2HDM+S type III scenario with $\tan\beta = 2.0$ , ob-	
396	tained at CMS with data collected at 13 TeV. . . . .	128

397	11.1 Generator-level b-flavor jet transverse momenta $p_T$ , for $h \rightarrow a_1 a_2$ cas-	
398	cade scenario in the $4b2\tau$ final state, for mass hypotheses $(m_{a_1}, m_{a_2}) =$	
399	$(100, 15)$ GeV ( <i>left</i> ) and $(40, 20)$ GeV ( <i>right</i> ). In each plot the generator-	
400	level $p_T$ of the leading ( <i>black</i> ), sub-leading ( <i>red</i> ), third ( <i>blue</i> ), and	
401	fourth ( <i>light green</i> ) are overlaid. . . . .	131
402	11.2 Distributions (arbitrary units) of transverse momentum $p_T$ resolution	
403	and $\Delta R$ between the two closest generator-level $b$ jets, treated as one	
404	object, and the nearest reconstructed AK4 jet, for two different $h \rightarrow$	
405	$a_1 a_2$ mass hypotheses $(m_{a_1}, m_{a_2}) = (100, 15)$ GeV ( <i>top left, top right</i> )	
406	and $(40, 20)$ GeV ( <i>bottom left, bottom right</i> ) in the ggH production of	
407	the 125 GeV $h$ . In the $(40, 20)$ GeV mass point, the longer $p_T$ resolution	
408	tail ( <i>bottom left</i> ) indicates that the reconstructed jet underestimates	
409	the generator b-flavor jets' energy, and the significant fraction of events	
410	with larger $\Delta R$ values ( <i>bottom right</i> ) indicate worse matching. . . . .	132
411	11.3 Kinematic properties of the leading muon and $\tau_h$ in the $\mu\tau_h$ channel: $p_T$	
412	( <i>top row</i> ), $\eta$ ( <i>second row</i> ), and $\phi$ ( <i>third row</i> ). The visible 4-momenta	
413	of the muon and $\tau_h$ are summed, giving the visible di-tau mass $m_{\text{vis}}$	
414	and transverse momentum $p_{T,\text{vis}}$ . The errors shown in the figures only	
415	include statistical errors and only several of the full set of systematic	
416	errors (only those associated with the lepton energy scales and $\tau_h$ iden-	
417	tification efficiency). . . . .	134
418	11.4 Kinematic properties of the leading and sub-leading b-tag jets in the	
419	$\mu\tau_h$ final state: jet $p_T$ ( <i>top row</i> ), $\eta$ ( <i>second row</i> ), $\phi$ ( <i>third row</i> ), as well	
420	as the missing transverse energy magnitude and azimuthal direction	
421	( <i>bottom row</i> ). The errors shown in the figures only include statistical	
422	errors and only several of the full set of systematic errors (only those	
423	associated with the lepton energy scales and $\tau_h$ identification efficiency).	135

# <sup>424</sup> Chapter 1

## <sup>425</sup> Introduction

<sup>426</sup> The Standard Model is the current prevailing theoretical framework that encompasses  
<sup>427</sup> all known elementary particles to date and describes their interactions, yet falls short  
<sup>428</sup> of describing open problems in physics. Here, we describe the history of the Standard  
<sup>429</sup> Model and its particle content (Section 1.1), and provide a mathematical motivation of  
<sup>430</sup> the SM as a gauge theory (Section 1.2). We introduce the Higgs mechanism (Section  
<sup>431</sup> 1.3), and outline two groups of theoretical extensions to the Standard Model that  
<sup>432</sup> feature extended Higgs sectors (Sections 1.4 and 1.5).

### <sup>433</sup> 1.1 History of the Standard Model

<sup>434</sup> The building blocks of our modern-day understanding of particle physics were estab-  
<sup>435</sup> lished over the course of many decades by experimental discoveries and theoretical  
<sup>436</sup> advances, culminating in the development of a theoretical framework known as the  
<sup>437</sup> Standard Model (SM). In the 1880s, the electron was the first subatomic particle to  
<sup>438</sup> be identified, through measurements of particles produced by ionizing gas. By the  
<sup>439</sup> 1930s, atoms were known to consist mostly of empty space, with protons and neutrons  
<sup>440</sup> concentrated at the center and orbited by electrons. Spurred by advances in parti-  
<sup>441</sup> cle accelerator technology, the experimental discoveries of the positron, the muon,

and the pion, painted an increasingly complicated picture of particle physics that could not be described solely with atomic physics [1]. Quantum field theory (QFT) began to be developed in the early 20th century as an extension of the conceptual framework of quantum mechanics to electromagnetic fields [2]. In 1927, Dirac coined the name quantum electrodynamics (QED), which was the first part of QFT that was developed. QED quantized the electromagnetic field and supplied a relativistic theory of the electron, and could be applied to concrete physical processes such as the scattering of high-frequency photons by free electrons (Compton scattering), and the production of electron-positron pairs by photons [2]. In the 1940s the QED-only picture was challenged by the realization that the four-fermion theory of weak interactions had infinities at higher orders of perturbation theory which could not be removed via the technique of renormalization [3], i.e. shifting divergences into parts of the theory that do not influence empirical measurements [2].

In the 1950s and 1960s, QFT was extended to describe not only the electromagnetic force, but also the strong and weak force, with the final picture forming the Standard Model. This took place in the development and maturation of three principles: the quark model, the idea of gauge (or local) symmetry, and spontaneously broken symmetry [3]. In the fully fledged QFT, Lagrangians had to be formed that contained new classes of quantum fields, or particles [2].

The particle content of the Standard Model is summarized in Fig. 1.1. Particles are grouped into fermions, which comprise all known matter, and bosons, which mediate the interactions between particles. Fermions consist of quarks and leptons, and are grouped into three generations. For example, the electron belongs to the first generation of leptons. The second and third generation counterparts of the electron are the muon and the tau lepton, and are over 200 and 30,000 times heavier than the electron respectively. The quarks are also organized into three generations (top and bottom quarks, charm and strange quarks, and up and down quarks), and

469 carry fractional electric charge. Bosons are force carriers; the interaction of fermions  
470 with bosons corresponds to fundamental forces. The Standard Model describes the  
471 electromagnetic force, the strong nuclear force, and the weak nuclear force. Through  
472 the strong force, quarks can form composite particles known as hadrons. Familiar  
473 examples of hadrons are the protons and neutrons in the nucleus of an atom.

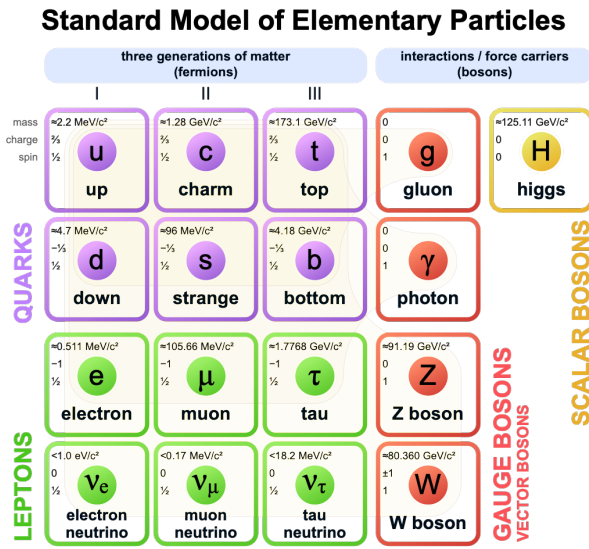


Figure 1.1: Table of Standard Model particles showing the grouping of the fermions into three generations of matter and the bosons, responsible for carrying the three fundamental forces in the Standard Model. The masses, charges, and spins of the particles are shown. The antimatter counterparts of the fermions are not shown. The possible interactions between the fermions and gauge bosons are highlighted.

## 1.2 The Standard Model as a gauge theory

<sup>475</sup> In this section we lay the theoretical foundations of the Standard Model as a gauge  
<sup>476</sup> theory, starting from the principle of gauge invariance (gauge symmetry), with local  
<sup>477</sup> gauge symmetries giving rise to interactions between particles.

<sup>478</sup> Gauge theories of elementary particle interactions originate from a freedom of  
<sup>479</sup> choice in the mathematical description of particle fields which has no effect on the  
<sup>480</sup> particles' physical states [4]. The existence and form of the particles' interactions,

481 can be deduced from the existence of physically indeterminate, gaugable quantities.

482 An example of this gauge invariance is classical physics is the electromagnetic  
483 interaction, where the fundamental field is the four-vector potential  $A^\mu$  [4]. The  
484 physical electromagnetic fields and Maxwell's equations arise from the elements of  
485 the tensor  $F_{\mu\nu}(x) = \partial_\mu A_\nu(x) - \partial_\nu A_\mu(x)$ . Any two choices of  $A^\mu$  that are related by a  
486 transformation of the form

$$A_\mu \rightarrow A_\mu + \partial_\mu \alpha \quad (1.1)$$

487 for any real, differentiable function  $\alpha(x)$ , describe the same physical configuration,  
488 and has no effect on Maxwell's equations. This "redundancy" in the choice of gauge  
489 in Eqn. 1.1 is called a gauge symmetry.

490 One important consequence of gauge symmetry comes from the application of  
491 Noether's theorem, which states that for every global transformation under which the  
492 Lagrangian density is invariant, there exists a conserved quantity. If  $\mathcal{L}(\Psi(x), \partial_\mu \Psi(x))$   
493 is invariant under the transformation of the wave function  $\Psi(x) \rightarrow \Psi'(x)$ , where  
494  $\Psi'(x) = \Psi(x) + \delta\Psi(x)$ , then there exists a conserved current

$$\partial_\mu \left( \frac{\partial \mathcal{L}(x)}{\partial (\partial_\mu \Psi(x))} \delta\Psi(x) \right) = 0 \quad (1.2)$$

495 In classical mechanics, the conservation of linear momentum, angular momentum,  
496 and energy follows from translational invariance, rotational variance, and invariance  
497 under translations in time [4]. Likewise, charge conservation can be shown to arise  
498 from the invariance of the Dirac Lagrangian density  $\mathcal{L}_{\text{Dirac}} = \bar{\Psi}(i\gamma^\mu \partial_\mu - m)\Psi$  under the  
499 particle wavefunction's phase transformation,  $\Psi'(x) = \exp(i\epsilon\chi)\Psi(x)$ . Thus Noether's  
500 theorem establishes a correspondence between a gauge symmetry and a conserved  
501 internal property (e.g. charge or momentum).

502 Interactions between particles arise if we modify the wave function with a phase

503 transformation  $\Psi'(x) = \exp(ie\chi)\Psi(x)$ , and allow the phase  $\chi$  to be a function of  
 504 spacetime [4]. A wave function of the form

$$\Psi'(x) = \exp(ie\chi(x))\Psi(x) \quad (1.3)$$

505 can be verified to *not* be a solution to the Dirac equation for free particles:  $(i\gamma^\mu\partial_\mu -$   
 506  $m)\Psi(x) = 0$ . This necessitates a modified Dirac equation, where the derivative takes  
 507 into account that the vector field  $V(x)$  needs to be compared at two displaced space-  
 508 time points in a curvilinear coordinate system:

$$\mathcal{D}_\mu \equiv \lim_{\Delta x^\mu \rightarrow 0} \frac{V_{||}(x + \Delta x) - V(x)}{\Delta x^\mu} \quad (1.4)$$

509 We define a covariant derivative,

$$D_\mu = \partial_\mu + ieA_\mu \quad (1.5)$$

510 where  $A_\mu(x)$  is a 4-vector potential. Thus the modified Dirac equation reads:

$$(i\gamma^\mu\mathcal{D}_\mu - m)\Psi(x) = 0 \quad (1.6)$$

511 The simultaneous gauge transformation  $A'_\mu(x) = A_\mu(x) - \partial_\mu\chi(x)$  and wavefunction  
 512 transformation  $\Psi'(x) = \exp(ie\chi(x))\Psi(x)$  leaves the covariant-derivative form of the  
 513 Dirac equation (Eqn 1.1) invariant.

514 The generalization of this result is as follows: if a theory is invariant for unitary  
 515 transformations  $U$  of the particle states according to

$$\Psi' = U\Psi \quad (1.7)$$

516 One must define a derivative of the form

$$D^\mu = \partial^\mu + igB^\mu \quad (1.8)$$

517 to keep the theory invariant under Eqn. 1.7. The four-potential  $B^\mu$  represents the  
518 interacting four-potential which must be added to keep the theory invariant.

519 In the case of the Standard Model, the theory is built around the gauge trans-  
520 formations  $G = SU(3) \times SU(2) \times U(1)$ .  $SU(3)$  is associated to the strong force  
521 (subscripted  $C$ );  $SU(2)$  is associated to the weak force (subscripted  $L$ ); and  $U(1)$  is  
522 hypercharge (subscripted  $Y$ ). The gauge-covariant derivative is

$$\mathcal{D}_\mu = \partial_\mu - ig'B_\mu \frac{Y}{2} - igW_\mu^\alpha \frac{\tau_a}{2} - ig_s G_\mu^k \frac{\lambda_k}{2} \quad (1.9)$$

523 • In the  $U(1)_Y$  term,  $B_\mu$  is the weak hypercharge field.

524 • In the  $SU(2)_L$  term,  $W_\mu(x) = (W_\mu^1(x), W_\mu^2(x), W_\mu^3(x))$  are a triplet of four-  
525 potentials.  $\tau/2$  are the Pauli matrices, generators of the  $SU(2)$  transformation.

526 • In the  $SU(3)_C$  term, the gluon (color) field is  $G_\mu$ .  $\lambda_k$  are the Gell-Man matrices,  
527 generators of the  $SU(3)$  transformation.

528 The invariance of the Standard Model under  $SU(3)_C \times SU(2)_L \times U(1)_Y$  requires  
529 massless fermions and massless force carriers.

### 530 1.3 The Higgs Mechanism

531 To introduce mass into the theory, i.e. to change the propagation of the gauge par-  
532 ticles and all the fermions, the physical vacuum cannot have all the symmetries of  
533 the Standard Model Lagrangian [4]. The symmetries of the physical vacuum must  
534 be spontaneously broken, without affecting gauge invariance in the Lagrangian. The

535 Higgs mechanism proposes the existence of a scalar field, or fields, with nonzero vac-  
 536 um expectation values, which reduce the gauge symmetries of the physical vacuum  
 537 from  $SU(3)_C \times SU(2)_L \times U(1)_Y$  down to  $SU(3)_C \times U(1)_{EM}$ .

538 The Higgs field interacts with the gauge bosons and fermions throughout space,  
 539 impeding their free propagation. The resulting broken symmetry correctly predicts  
 540 the mass ratio of the neutral (Z) and charged (W) massive electroweak bosons, and  
 541 predicts that at least one physical degree of freedom in the Higgs field is a particle  
 542 degree of freedom, called the Higgs boson. The location of the minimum of the Higgs  
 543 potential can be constrained from previously measured Standard Model parameters,  
 544 but the shape of the mass distribution of the Higgs boson must be experimentally  
 545 measured.

546 The minimal choice of Higgs field comes from the breaking of  $SU(2)_L \times U(1)_Y$   
 547 down to  $U(1)_{EM}$ . The smallest  $SU(2)$  multiplet is the doublet. The existence of three  
 548 massive electroweak bosons leads the Higgs sector to have at least three degrees of  
 549 freedom. The minimal single-doublet complex scalar Higgs field is

$$\Phi(x) = \begin{pmatrix} \phi^+(x) \\ \phi^0(x) \end{pmatrix} = \frac{1}{\sqrt{2}} \begin{pmatrix} \phi_1^+(x) + i\phi_2^+(x) \\ \phi_1^0(x) + i\phi_2^0(x) \end{pmatrix} \quad (1.10)$$

550 where  $\phi_1^+$ ,  $\phi_2^+$ ,  $\phi_1^0$ , and  $\phi_2^0$  are real (four degrees of freedom). By convention, the  
 551 nonzero vacuum expectation value is assigned to  $\phi_1^0$ .

552 The minimal self-interacting Higgs potential that is invariant under  $SU(2)_L \times$   
 553  $U(1)_Y$  is given by

$$V(\Phi^\dagger \Phi) = -\mu^2 \Phi^\dagger \Phi + \lambda (\Phi^\dagger \Phi)^2, \quad \mu^2 > 0, \lambda > 0 \quad (1.11)$$

554 where  $\lambda$  is the coupling strength of the four-point Higgs interaction. The potential

555 energy is minimized at

$$\Phi_{\min} = \frac{1}{\sqrt{2}} \begin{pmatrix} 0 \\ v \end{pmatrix}, \text{ where } v = \sqrt{\mu^2/\lambda} \quad (1.12)$$

556 Choosing a fixed orientation of  $\langle \Phi \rangle$  out of a continuous set of possible ground states  
 557 spontaneously breaks the symmetry of the physical vacuum, as illustrated in Fig 1.2.

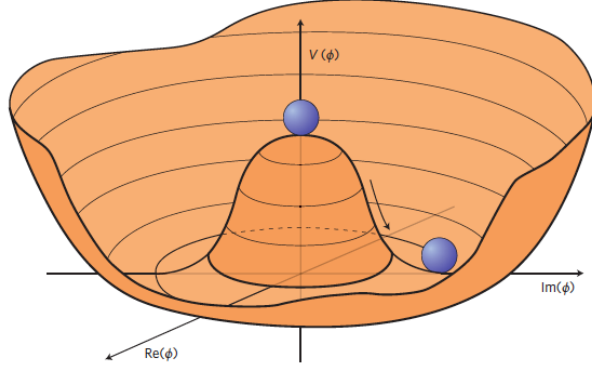


Figure 1.2: An illustration of the Higgs potential [5]. Choosing any of the points at the bottom of the potential breaks spontaneously the rotational  $U(1)$  symmetry.

558 The excitations of the Higgs field with respect to the minimum  $\Phi_{\min}$  are parame-  
 559 terized by

$$\Phi(x) = \exp(i\xi(x) \cdot \tau) \frac{1}{\sqrt{2}} \begin{pmatrix} 0 \\ v + H(x) \end{pmatrix} \quad (1.13)$$

560 Three degrees of freedom are coupled directly to the electroweak gauge bosons; this  
 561 is often referred to as the gauge bosons “eating” the Goldstone bosons to form the  
 562 longitudinal polarizations of the massive spin-1 boson states. The  $H(x)$  excitation is  
 563 in the radial direction and corresponds to the free particle state of the Higgs boson.

## 564 1.4 Two-Higgs Doublet Models

565 One of the simplest possible extensions to the Standard Model is adding a doublet  
 566 to the minimal Higgs sector of the Standard Model, which is a  $SU(2)_L$  doublet  $H$

567 with hypercharge  $Y = +\frac{1}{2}$ , denoted here as  $H \sim 2_{+1/2}$ . These extensions are found  
 568 in several theories such as supersymmetry. A general 2HDM can be extended with a  
 569 light scalar (2HDM+S) to obtain a rich set of exotic Higgs decays [6].

The charges of the Higgs fields are chosen to be  $H_1 \sim 2_{-1/2}$  and  $H_2 \sim 2_{+1/2}$ , which  
 acquire vacuum expectation values  $v_{1,2}$  which are assumed to be real and aligned [6].  
 Expanding about the minima yields two complex and four real degrees of freedom:

$$H_1 = \frac{1}{\sqrt{2}} \begin{pmatrix} v_1 + H_{1,R}^0 + iH_{1,I}^0 \\ H_{1,R}^- + iH_{1,I}^- \end{pmatrix} \quad (1.14)$$

$$H_2 = \frac{1}{\sqrt{2}} \begin{pmatrix} H_{2,R}^+ + iH_{2,I}^+ \\ v_2 + H_{2,R}^0 + iH_{2,I}^0 \end{pmatrix} \quad (1.15)$$

570 The charged scalar and pseudoscalar mass matrices are diagonalized by a rotation  
 571 angle  $\beta$ , defined as  $\tan \beta = v_2/v_1$ . One charged (complex) field and one neutral  
 572 pseudoscalar combination of  $H_{1,2,I}^0$  are eaten by the SM gauge bosons after electroweak  
 573 symmetry breaking [6]. The other complex field yields two charged mass eigenstates  
 574  $H^\pm$ , which are assumed to be heavy. The remaining three degrees of freedom yield  
 575 one neutral pseudoscalar mass eigenstate

$$A = H_{1,I}^0 \sin \beta - H_{2,I}^0 \cos \beta \quad (1.16)$$

576 and two neutral scalar mass eigenstates (where  $-\pi/2 \leq \alpha \leq \pi/2$ )

$$\begin{pmatrix} h \\ H^0 \end{pmatrix} = \begin{pmatrix} -\sin \alpha & \cos \alpha \\ \cos \alpha & \sin \alpha \end{pmatrix} \begin{pmatrix} H_{1,R}^0 \\ H_{2,R}^0 \end{pmatrix} \quad (1.17)$$

577 We assume that the 2HDM is near or in the decoupling limit:  $\alpha \rightarrow \pi/2 - \beta$ , where the  
 578 lightest state in the 2HDM is  $h$ , which we identify as the 125 GeV Higgs particle [6].  
 579 In this limit, the fermion couplings of  $h$  become identical to the Standard Model

580 Higgs, while the gauge boson couplings are very close to Standard Model-like for  
581  $\tan \beta \gtrsim 5$ . All of the properties of  $h$  can be determined by just two parameters:  $\tan \beta$   
582 and  $\alpha$ , and the fermion couplings to the two Higgs doublets.

583 2HDM can be extended by a scalar singlet (2HDM+S) [6]:

$$S = \frac{1}{\sqrt{2}}(S_R + iS_I) \quad (1.18)$$

584 If this singlet only couples to the Higgs doublets  $H_{1,2}$  and has no direct Yukawa  
585 couplings, all of its couplings to SM fermions result from mixing with  $H_{1,2}$ . Under  
586 these simple assumptions, exotic Higgs decays  $h \rightarrow ss \rightarrow X\bar{X}Y\bar{Y}$  or  $h \rightarrow aa \rightarrow$   
587  $X\bar{X}Y\bar{Y}$ , and  $h \rightarrow aZ \rightarrow X\bar{X}Y\bar{Y}$  are permitted, where  $s(a)$  is a (pseudo)scalar mass  
588 eigenstate mostly composed of  $S_R(S_I)$ , and  $X, Y$  are Standard Model fermions or  
589 gauge bosons. There are two pseudoscalars in the 2HDM+S, and the mostly singlet-  
590 like pseudoscalar can be chosen to be the one lighter than the SM-like Higgs. For  
591  $m_a < m_h - m_Z \sim 35$  GeV, the exotic Higgs decay  $h \rightarrow Za$  is possible, and for  
592  $m_a < m_h/2 \approx 63$  GeV, the exotic Higgs decay  $h \rightarrow aa$  is possible.

593 In 2HDM, and by extension 2HDM+S, there are four types of fermion couplings  
594 commonly discussed in the literature that forbid flavor-changing neutral currents at  
595 tree level [6]. These are referred to as Type I (all fermions couple to  $H_2$ ), Type II  
596 (MSSM-like,  $d_R$  and  $e_R$  couple to  $H_1$ ,  $u_R$  to  $H_2$ ), Type III (lepton-specific, leptons  
597 and quarks couple to  $H_1$  and  $H_2$  respectively) and Type IV (flipped, with  $u_R$ ,  $e_R$   
598 coupling to  $H_2$  and  $d_R$  to  $H_1$ ). The exact branching ratios of the pseudoscalars to  
599 Standard Model particles vary depending on the 2HDM+S model and the value of  
600  $\tan \beta$  (e.g. Fig. 1.3).

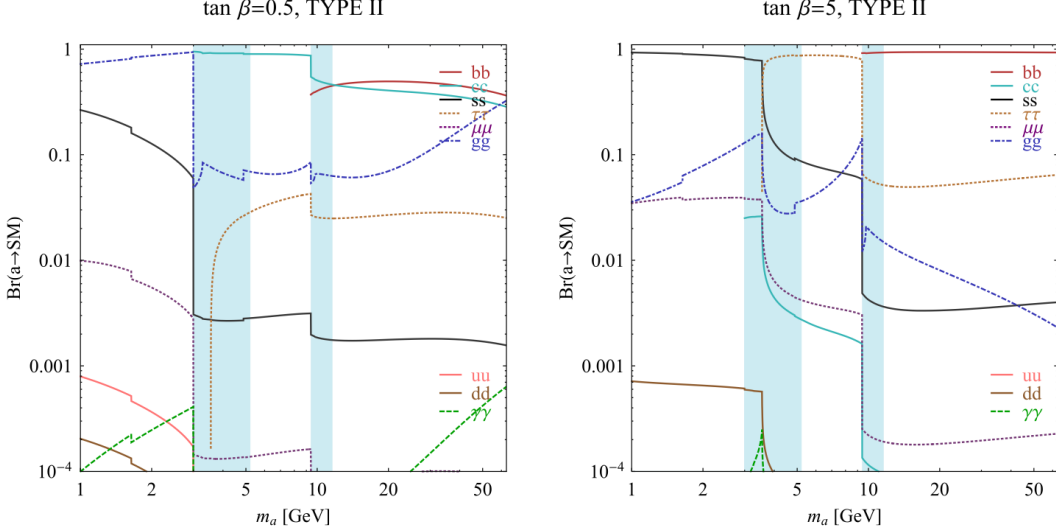


FIG. 7 (color online). Branching ratios of a singletlike pseudoscalar in the 2HDM + S for type-II Yukawa couplings. Decays to quarkonia likely invalidate our simple calculations in the shaded regions.

Figure 1.3: Branching ratios of a singlet-like pseudoscalar in Type II 2HDM+S for  $\tan\beta = 0.5$  (left) and  $\tan\beta = 5$  (right) from [6], showing the dependence of the branching ratios on  $\tan\beta$ , as well as the prominence of the branching ratios to  $bb$  and  $\tau\tau$ , the channels searched for in the analysis presented here.

## 1.5 Two Real Singlet Model

The two real singlet model (TRSM) adds two real singlet degrees of freedom to the Standard Model. These are written as two real singlet fields  $S$  and  $X$ . Depending on the vacuum expectation values acquired by the scalars, different phases of the model can be realized [7]. To reduce the number of free parameters, two discrete  $\mathbb{Z}_2$  symmetries are introduced. The fields are decomposed as

$$\Phi = \begin{pmatrix} 0 \\ \frac{\phi_h + v}{\sqrt{2}} \end{pmatrix}, S = \frac{\phi_S + v_S}{\sqrt{2}}, X = \frac{\phi_X + v_X}{\sqrt{2}} \quad (1.19)$$

To achieve electroweak-breaking symmetry,  $v = v_{SM} \sim 246$  GeV is necessary. If the vacuum expectation values  $v_S, v_X \neq 0$  the  $\mathbb{Z}_2$  are spontaneously broken, and the fields  $\phi_{h,S,X}$  mix into three physical scalar states. This is called the broken phase and leads to the most interesting collider phenomenology.

611        The mass eigenstates  $h_{1,2,3}$  are related to the fields  $\phi_{h,S,X}$  through a  $3 \times 3$  orthogonal  
612        mixing matrix denoted  $R$ . The mass eigenstates are assumed to be ordered  $M_1 \leq$   
613         $M_2 \leq M_3$ .  $R$  is parameterized by the three mixing angles  $\theta_{hS}$ ,  $\theta_{hX}$ ,  $\theta_{SX}$ . The nine  
614        parameters of the scalar potential can be expressed in terms of the three physical  
615        Higgs masses, the three mixing angles, and the three vacuum expectation values.

616        After fixing one of the Higgs masses to the mass of the observed Higgs boson, and  
617        fixing the Higgs doublet vacuum expectation value to its Standard Model value, there  
618        are seven remaining free parameters of the TRSM [7].

619        In one benchmark scenario of TRSM [7], the heaviest scalar state  $h_3$  is identified  
620        with the 125 GeV Higgs,  $h_{125}$ , and it can decay asymmetrically  $h_{125} \rightarrow h_1 h_2$ , which  
621        we also denote  $h \rightarrow a_1 a_2$  to highlight the similarity with the symmetric decay  $h \rightarrow aa$   
622        typically interpreted in 2HDM+S as discussed. The parameter values in TRSM are  
623        chosen such that the coupling of  $h_3$  to Standard Model particles are nearly identical  
624        to the Standard Model predictions.

625        In benchmark scenario 1 (benchmark plane 1, or BP1) (Fig. 1.4) [7], the maximal  
626        branching ratios for  $h_3 \rightarrow h_1 h_2$  reach up to 7 – 8% which translates into a signal  
627        rate of around 3 pb. These maximal branching ratios are reached in the intermediate  
628        mass state for  $h_2$ ,  $M_2 \sim 60 – 80$  GeV. For  $M_2 < 40$  GeV, although phase space opens  
629        up significantly for light decay products, the branching ratio becomes smaller.

630        If the decay channel  $h_2 \rightarrow h_1 h_1$  is kinematically open (i.e.  $M_2 > 2M_1$ ), it is the  
631        dominant decay mode leading to a significant rate for the  $h_1 h_1 h_1$  final state, in a  
632        “cascade” decay. In BP1,  $BR(h_2 \rightarrow h_1 h_1) \simeq 100\%$  above the red line in Fig. 1.4. If,  
633        in addition,  $M_1 \gtrsim 10$  GeV, the  $h_1$  decays dominantly to  $b\bar{b}$  leading to a sizable rate  
634        for the  $b\bar{b}b\bar{b}b\bar{b}$  final state as shown in Fig. 1.4 (*bottom right*).

635        If the  $h_2 \rightarrow h_1 h_1$  decay is kinematically closed (i.e.  $M_2 < 2M_1$ ), both scalars decay  
636        directly to Standard Model particles, with branching ratios identical to a Standard  
637        Model-like Higgs boson, i.e. with the  $b\bar{b}b\bar{b}$  final state dominating, as shown in Fig. 1.4

<sub>638</sub> (*bottom left*), while at smaller masses, combinations with  $\tau$  leptons and eventually  
<sub>639</sub> final states with charm quarks and muons become relevant [7].

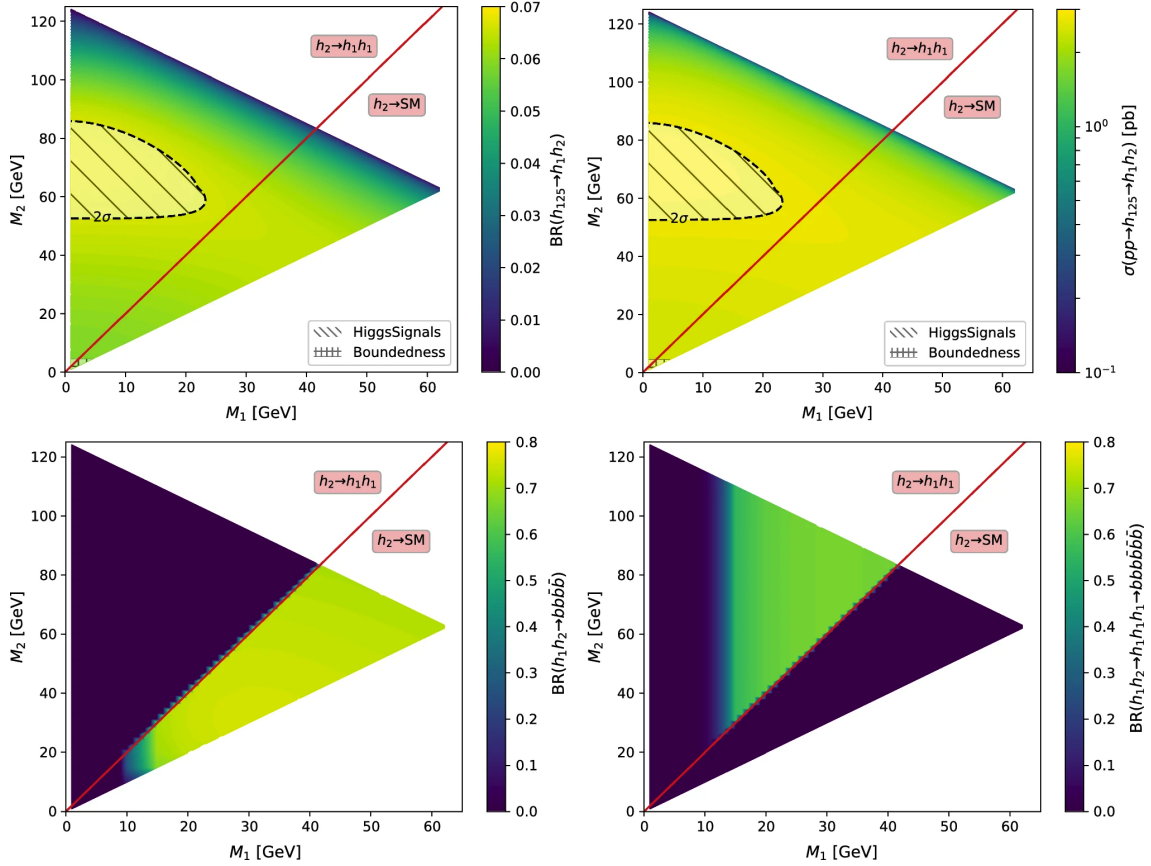


Figure 1.4: Benchmark plane BP1 for benchmark scenario 1 from [7], for the decay signature  $h_{125} \rightarrow h_1 h_2$  with  $h_{125} \equiv h_3$ , defined in the  $(M_1, M_2)$  plane. The color code shows  $\text{BR}(h_3 \rightarrow h_1 h_2)$  (*top left*) and the 13 TeV LHC signal rate for  $pp \rightarrow h_3 \rightarrow h_1 h_2$  (*top right*). The red line separates the region  $M_2 > 2M_1$ , where  $\text{BR}(h_2 \rightarrow h_1 h_1) \sim 100\%$ , from the region  $M_2 < 2M_1$ , where  $\text{BR}(h_2 \rightarrow F_{SM}) \sim 100\%$ . The *bottom left* and *right* show the branching ratio of the  $h_1 h_2$  into (respectively)  $b\bar{b}b\bar{b}$ , and through a  $h_2 \rightarrow h_1 h_1$  cascade to  $b\bar{b}b\bar{b}b\bar{b}$ . The hatched region indicates where the decay rate slightly exceeds the  $2\sigma$  upper limit inferred from the LHC Higgs rate measurements, though the region depends on the parameter choices and experimental searches should cover the whole mass range.

640 **Chapter 2**

641 **The Large Hadron Collider and the**  
642 **CMS Experiment**

643 This chapter introduces the key aspects of the CERN Large Hadron Collider (LHC)  
644 and the Compact Muon Solenoid (CMS) experiment where the work for this thesis was  
645 conducted. Section 2.1 describes the history of accelerator developments at CERN  
646 that led to the construction of the LHC, the current LHC configuration, and the  
647 largest experiments located at the LHC. The concepts of beam luminosity and pile-  
648 up, which are critical for understanding and measuring high-energy particle collisions,  
649 are described in Section 2.2 and discussed in the context of the High-Luminosity  
650 LHC (HL-LHC) upgrade in Section 2.3. Lastly, Section 2.4 describes the design  
651 and function of CMS and its subdetectors, and terminates in a description of data  
652 processing at CMS, beginning from online event filtering in the Level-1 Trigger, to  
653 processing in the High-Level Trigger, to offline particle reconstruction, and finally  
654 long-term storage and processing of measured events.

## 655 2.1 The Large Hadron Collider

656 CERN, the European Organization for Nuclear Research, is an international organiza-  
657 tion based in Meyrin, Switzerland which operates the world's largest particle physics  
658 laboratory, and is the site of the Large Hadron Collider (LHC) [8]. The very first  
659 accelerator built at CERN was the 600 MeV Synchrocyclotron (SC), which initially  
660 provided beams for CERN's first experiments. The newer and more powerful Proton  
661 Synchrotron (PS), which could accelerate particles to an energy of 28 GeV, began op-  
662 erations in 1959 and is still in use today. The first hadron collider at CERN was the  
663 Intersecting Storage Rings (ISR), which consisted of two interlaced rings each with a  
664 diameter of 200. The ISR collided protons at a center-of-mass energy of 62 GeV and  
665 began measuring collisions in 1971. In 1968 CERN began to accelerate heavy ions  
666 in the Super Proton Synchrotron (SPS), which is 7 kilometers in circumference and  
667 was the first of CERN's giant underground rings to be built. The SPS became the  
668 forefront of CERN's particle physics program in 1976, and in 1981 was converted into  
669 a proton-antiproton collider. The final and largest underground ring constructed at  
670 CERN was the Large Electron-Positron (LEP) collider, which was commissioned in  
671 July 1989 and hosted 5176 magnets and 128 accelerating cavities located around a  
672 27-kilometer circumference. Over 11 years of research, four detectors, ALEPH, DEL-  
673 PHI, L3, and OPAL measured the collisions, with collision energies reaching up to  
674 209 GeV in the year 2000. In November 2000, LEP was closed down to make way for  
675 the construction of the LHC in the same tunnel.

676 In its current configuration, the LHC accelerator complex at CERN is a suc-  
677 cession of machines that accelerate particles in stages until they reach their final energy  
678 of 6.5 TeV per beam [9] [10]. In Linear accelerator 4 (Linac4), negative hydrogen  
679 ions (hydrogen atoms with an additional electron) are accelerated to 160 MeV, and  
680 stripped of their two electrons, leaving only protons, before entering the Proton Syn-  
681 chrotron Booster (PSB). These protons are accelerated to 2 GeV, then to 26 GeV in

682 the Proton Synchrotron (PS), and 450 GeV in the Super Proton Synchrotron (SPS).  
683 The protons are transferred to the two beam pipes of the Large Hadron Collider  
684 (LHC). The LHC is a 27-kilometer ring of superconducting magnets, inside which  
685 one beam circulates clockwise and the other counterclockwise. Each LHC ring takes  
686 4 minutes and 20 seconds to fill, and it takes about 20 minutes for the protons to  
687 reach their maximum energy. During normal operating conditions, beams circulate  
688 for many hours inside the LHC ring.

689 The beams of particles in the LHC are made to collide at a center-of-mass energy  
690 of up to 14 TeV, at four positions at particle detector experiments located around  
691 the ring: ATLAS, CMS, ALICE, and LHCb. An aerial view of the four major  
692 experiments' locations is shown in Fig. 2.1 [11]. ATLAS and CMS are the two  
693 general-purpose detectors with broad physics programmes spanning Standard Model  
694 measurements and searches for signatures of new physics [12] [13]. The two experi-  
695 ments use different technical solutions and different magnet system designs. ALICE  
696 is a general-purpose detector dedicated to measuring LHC heavy-ion collisions, and  
697 is designed to address the physics of strongly interacting matter, and the properties  
698 of quark-gluon plasma [14]. The LHCb experiment specializes in investigating CP vi-  
699 olation through measuring the differences in matter and antimatter, by using a series  
700 of subdetectors to detect mainly forward particles close to the beam direction [15].

## 701 **2.2 Luminosity and pile-up**

702 In order to search for rare processes, such as those resulting from a Higgs, W, or Z  
703 boson, a large number of parton interactions per second are required at the LHC.  
704 The number of events generated per second by the LHC collisions is given by

$$N_{event} = \mathcal{L} \cdot \sigma_{event} \quad (2.1)$$

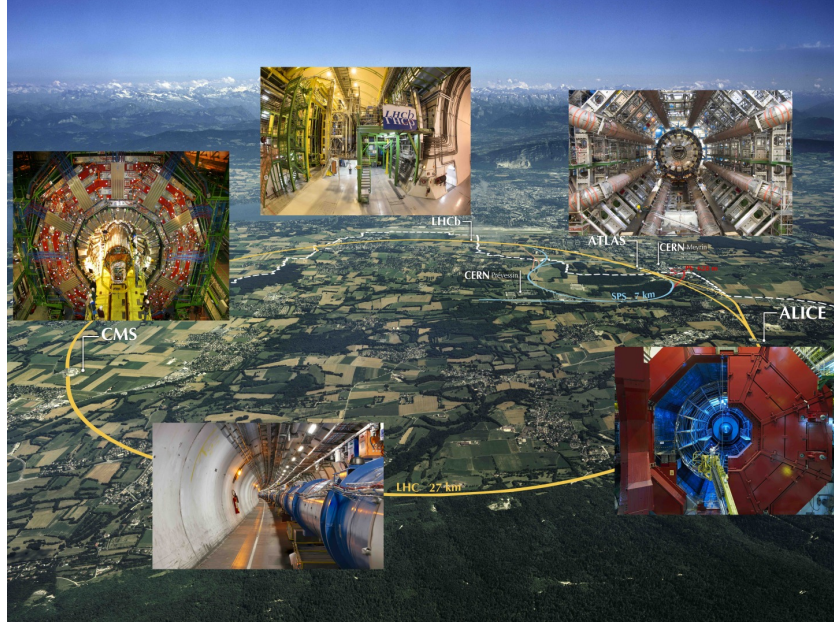


Figure 2.1: Aerial view of the Large Hadron Collider (LHC) spanning the border of France and Switzerland, and the four major experiments located around the ring: CMS (Compact Muon Solenoid), LHCb (LHC beauty), ATLAS (A Toroidal LHC Apparatus), and ALICE (A Large Ion Collider Experiment) [11].

where  $\sigma_{event}$  is the cross-section for the event under study, and  $\mathcal{L}$  the instantaneous luminosity. The instantaneous luminosity is measured in units of  $\text{cm}^{-2} \text{ s}^{-1}$ , and depends only on the beam parameters, and can be written for a Gaussian beam distribution as:

$$\mathcal{L} = \frac{N_b^2 n_b f_{rev} \gamma_r}{4\pi \epsilon_n \beta^*} F \quad (2.2)$$

where the parameters are as defined, along with some example typical nominal values in Phase-1 of the LHC [16] [17]:

- $N_b$  is the number of particles per bunch ( $N_b \approx 1.15 \times 10^{11}$  protons per bunch)
- $n_b$  is the number of bunches per beam (maximum 2808),
- $f_{rev}$  is the revolution frequency ( $\approx 11 \text{ kHz}$ ),
- $\gamma_r$  is the relativistic gamma factor,

- $\epsilon_n$  is the normalized transverse beam emittance (area in a transverse plane occupied by the beam particles),
  - $\beta^*$  is the beta function at the collision point ( $\beta^* = 0.55$  m),
  - and  $F$  is the geometric luminosity reduction factor due to the crossing angle at the interaction points ( $F \approx 0.84$  for Phase-1. Note that complete overlap would give  $F = 1$ ).

721 Peak luminosity at interaction points 1 and 5 reach values of  $\sim 1.0 \times 10^{34} \text{ cm}^{-2} \text{ s}^{-1}$ ,  
 722 with peak luminosity per bunch crossing reaching  $\sim 3.56 \times 10^{34} \text{ cm}^{-2} \text{ s}^{-1}$ .

Per Eqn. 2.1, the integrated luminosity over time is proportional to the number of events produced, and the size of LHC datasets is commonly presented in terms of integrated luminosity. Collider operation aims to optimize the integrated luminosity. Thus the exploration of rare events in the LHC collisions requires both high beam energies and high beam intensities.

The interaction vertex corresponding to the hard scattering of the protons is called the primary interaction vertex, or primary vertex (PV). The LHC’s nominal beam luminosities are sufficiently large for multiple proton-proton collisions to occur in the same time window of 25 nanoseconds in which proton bunches collide [18]. To measure a proton-proton collision, the primary vertices must be separated from overlapping collisions, called “pile-up” collisions.

The pile-up is defined as the average number of  $pp$  collisions per bunch crossing, and can be estimated from the inelastic  $pp$  cross section of  $\sigma_{\text{inel}} = 68.6$  millibarns at a center-of-mass energy of  $\sqrt{s} = 13$  TeV [19]:

$$\text{Pile-up} = \frac{\mathcal{L} \times \sigma_{\text{inel}}}{n_b \cdot f} \sim 22 \quad (2.3)$$

<sup>737</sup> A distribution of pile-up in the data-taking years 2016-2018 is shown in Fig. 2.2.

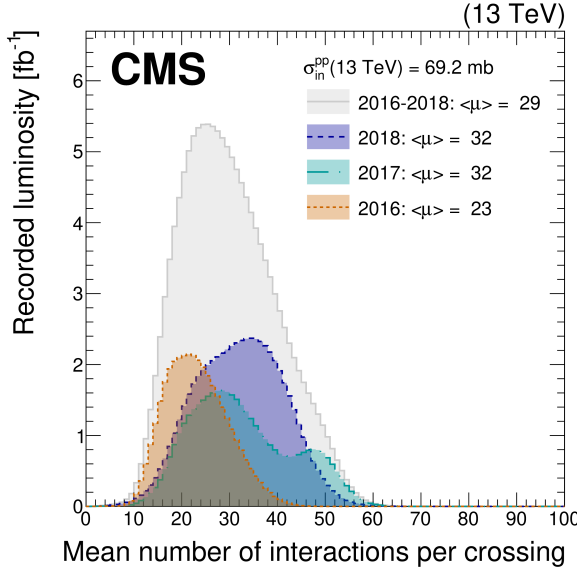


Figure 2.2: Distribution of the mean number of inelastic collisions per bunch crossing (pile-up) in data [18], for proton-proton collisions in 2016 (*dotted orange*), 2017 (*dotted light blue*), 2018 (*dotted dark blue*), and integrated over 2016-2018 (*solid grey*). A cross-section of inelastic proton-proton collisions of 69.2 mbarns is assumed. In the running conditions of the High-Luminosity LHC, pile-up will reach unprecedented levels of up to 200 per bunch crossing [20].

These multiple collisions will lead to higher occupancies in the detector, and particles originating from the pile-up interactions can be confused with those originating from the primary vertex. Thus, higher luminosities create more intense pile-up conditions, posing a greater challenge to detector performance and particle reconstruction and identification.

## 2.3 The High-Luminosity LHC

The High-Luminosity LHC (HL-LHC) is a major upgrade of the LHC scheduled to take place in the late 2020s, that will increase the instantaneous luminosity by a factor of five beyond the original design value, and the integrated luminosity by a factor of ten [20]. This will be accomplished through accelerator technological advances: for instance, reduction of the interaction point  $\beta^*$  from 0.55 m down to 0.15

749 m by installation of new final-focusing magnets, and improvements in the geometric  
750 luminosity loss factor  $F \approx 1$  through the installation of crab cavities that optimize  
751 the orientation of colliding bunches. A further discussion of the HL-LHC upgrades  
752 for the CMS detector follows in Chapter 3.

## 753 2.4 The CMS Detector

754 We give a brief overview of the Compact Muon Solenoid (CMS) experiment here  
755 and discuss each of the subdetectors in more detail in the following sections. The  
756 CMS experiment was conceived to study proton-proton and lead-lead collisions at  
757 a center-of-mass energy of 14 TeV (5.5 TeV nucleon-nucleon) and at luminosities up  
758 to  $10^{34} \text{ cm}^{-2} \text{ s}^{-1}$  ( $10^{27} \text{ cm}^{-2} \text{ s}^{-1}$ ) [21] [22]. Starting from the beam interaction region  
759 at the center of the CMS detector, particles first pass through a silicon pixel and  
760 strip tracker, in which charged-particle trajectories (tracks) and origins (vertices)  
761 are reconstructed from signals (hits) in the sensitive layers. The tracker, electro-  
762 magnetic calorimeter (ECAL), and hadronic calorimeter (HCAL) are immersed in a  
763 high-magnetic-field superconducting solenoid that bends the trajectories of charged  
764 particles. After passing through the tracker, electrons and photons are then absorbed  
765 in the electromagnetic calorimeter (ECAL) comprised of lead-tungstate scintillating-  
766 crystals. The corresponding electromagnetic showers are detected as clusters of energy  
767 recording in neighboring cells, from which the direction and energy of the particles can  
768 be determined. Charged and neutral hadrons may initiate a hadronic shower in the  
769 ECAL as well, which is then fully absorbed in the hadron calorimeter (HCAL). The  
770 resulting clusters are used to estimate their direction and energies. Muons and neu-  
771 trinos pass through the calorimeters with little to no interactions. Neutrinos escaped  
772 undetected; muons produce hits in additional gas-ionization chamber muon detectors  
773 housed in the iron yoke of the flux-return. A sketch of example particle interactions

in a transverse slice of the CMS detector is shown in Fig. 2.3. The collision data is recorded with the use of the Level-1 (L1) trigger (discussed in greater detail in 2.5.5), the High-Level Trigger (HLT), and data acquisition systems ensuring high efficiency in selecting physics events of interest.

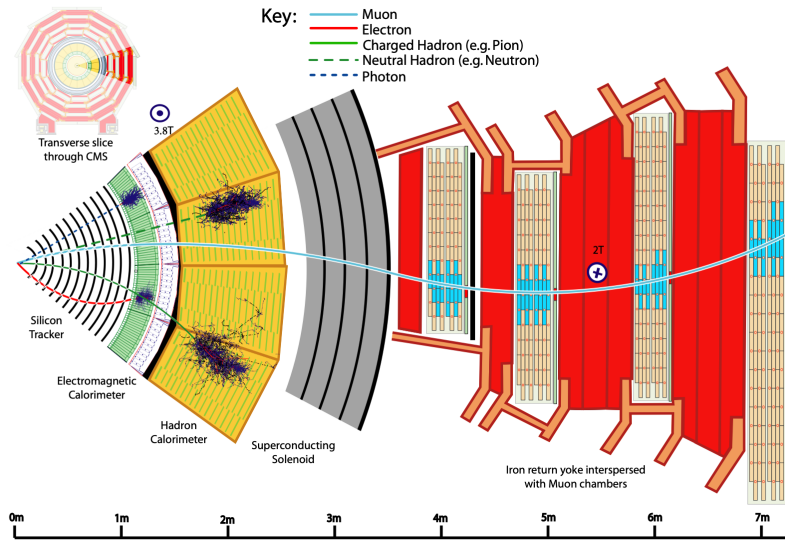


Figure 2.3: Sketch of particle trajectories of muons, electrons, charged and neutral hadrons, and photons in a transverse cross-section of the CMS detector [22].

CMS uses a right-handed coordinate system [21]. The origin is centered at the nominal collision point inside the experiment. The  $x$  axis points towards the center of the LHC, and the  $y$  axis points vertically upwards. The  $z$  axis points along the beam direction. The azimuthal angle,  $\phi$ , is measured from the  $x$  axis in the  $x$ - $y$  plane, and the radial coordinate in this plane is denoted by  $r$ . The polar angle,  $\theta$ , is measured from the  $z$  axis. The pseudorapidity,  $\eta$ , is defined as  $\eta = -\ln \tan(\theta/2)$ . The momentum and energy transverse to the beam direction, denoted by  $p_T$  and  $E_T$  respectively, are computed from the  $x$  and  $y$  components. The momentum imbalance in the transverse plane is called the missing transverse momentum, and its magnitude is denoted by  $E_T^{\text{miss}}$ .

## 2.5 Sub-detectors of CMS

This section details the sub-detectors of CMS that operate to identify and precisely measure muons, electrons, photons, and jets over a large energy range.

### 2.5.1 Inner tracking system

The CMS Tracker performs robust tracking and detailed vertex reconstruction in the 4 T magnetic field of the superconducting solenoidal magnet. The primary sensors used in the tracker are  $p^+$  on  $n$ -bulk devices, which allow high voltage operation and are radiation-resistant [23] [24]. The active envelope of the CMS Tracker extends to a radius of 115 cm, over a length of approximately 270 cm on each side of the interaction point [23]. Charged particles in the region  $|\eta| \lesssim 1.6$  benefit from the full momentum measurement precision. In this region, a charged particle with  $p_T$  of 1000 GeV has a sagitta of  $\sim 195 \mu\text{m}$ . The Tracker acceptance extends further to  $|\eta| = 2.5$ , with a reduced radius of approximately 50 cm.

The high magnetic field of CMS causes low  $p_T$  charged particles to travel in helical trajectories with small radii. The majority of events contain particles with a steeply falling  $p_T$  spectrum, resulting in a track density which rapidly decreases at higher radii.

A schematic view of the current Phase-1 CMS tracker [25], including the pixel detector, is shown in Fig. 2.4. The Phase-1 pixel detector consists of three barrel layers (BPIX) at radii of 4.4 cm, 7.3 cm, and 10.2 cm, and two forward/backward disks (FPIX) at longitudinal positions of  $\pm 34.5$  cm and  $\pm 46.5$  cm, and extending in radius from about 6 cm to 15 cm. These pixelated detectors produce 3D measurements along the paths of charged particles with single hit resolutions between 10-20  $\mu\text{m}$ .

After the pixel and on their way out of the tracker, particles pass through the silicon strip tracker which reaches out to a radius of 130 cm (Fig. 2.4). The sensor el-

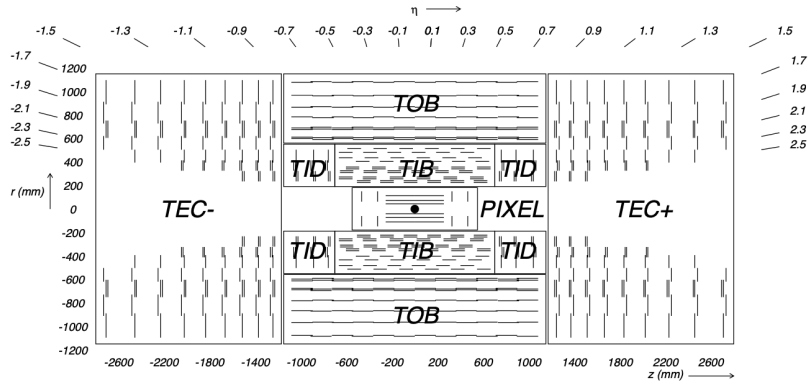


Figure 2.4: Cross section of the current Phase-1 CMS tracker [25]. Each line represents a detector module. Double lines indicate back-to-back modules which deliver two-dimensional (stereo) hits in the strip tracker.

ements in the strip tracker are single-sided  $p$ -on- $n$  type silicon micro-strip sensors [21].  
 The silicon strip detector consists of four inner barrel (TIB) layers assembled in shells,  
 with two inner endcaps (TID), each composed of three small discs. The outer barrel  
 (TOB) consists of six concentric layers. Two endcaps (TEC) close off the tracker on  
 either end.

### 2.5.2 ECAL

The electromagnetic calorimeter (ECAL) of CMS measures electromagnetic energy deposits with high granularity. One of the driving criteria in the design was the capability of detecting the Standard Model Higgs boson decay to two photons (in fact, the channel in which the 125 GeV Higgs boson was discovered at CMS). ECAL is a hermetic homogeneous calorimeter comprised of 61,200 lead tungstate ( $\text{PbWO}_4$ ) crystals mounted in the central barrel, with 7,324 crystals in each of the two endcaps [21]. A preshower detector is located in front of the endcap crystals. Avalanche photodiodes (APDs) are used as photodetectors in the barrel and vacuum phototriodes (VPTs) in the endcaps.

The design of the ECAL is driven by the behaviour of high-energy electrons, which

predominantly lose energy in matter via bremsstrahlung, and high-energy photons by  $e^+e^-$  pair production. The characteristic amount of matter traversed for these interactions is the radiation length  $X^0$ , usually measured in units of g cm $^{-2}$ . The radiation length is also the mean distance over which a high-energy electron loses all but  $1/e$  of its energy via bremsstrahlung [26]. Thus high granularity in  $\eta$  and  $\phi$ , and the length of the ECAL crystals, is designed to capture the shower of  $e/\gamma$  produced by electrons and photons.

The barrel part of the ECAL (EB) covers the pseudorapidity range  $|\eta| < 1.479$  [21]. The barrel granularity is 360-fold in  $\phi$  and  $(2 \times 85)$ -fold in  $\eta$ . The crystal cross-section corresponds to approximately  $0.0174 \times 0.0174$  in  $\eta - \phi$  or  $22 \times 22$  mm $^2$  at the front face of the crystal, and  $26 \times 26$  mm $^2$  at the rear face. The crystal length is 230 mm, corresponding to  $25.8 X_0$ .

The ECAL read-out acquires the signals of the photodetectors [21]. At each bunch crossing, digital sums representing the energy deposit in a trigger tower, comprising  $5 \times 5$  crystals in  $\eta \times \phi$ , are generated and sent to the Level-1 trigger system (detailed in Section 2.5.5).

### 2.5.3 HCAL

The hadronic calorimeter (HCAL) of CMS measures hadronic energy, which is key to characterizing the presence of apparent missing transverse energy which could arise from hadron jets and neutrinos or exotic particles [21]. A schematic of the components of HCAL are shown in Fig. 2.5. The HCAL barrel (HB) and endcaps (HE) are located outside of the tracker and the ECAL, spanning a radius of 1.77 m (outer extent of ECAL) up to 2.95 m (inner extent of the magnet coil). An outer hadron calorimeter (HO) is placed outside the solenoid to complement the barrel calorimeter. Beyond  $|\eta| = 3$ , the forward hadron calorimeter (HF) at 11.2 m from the interaction point extend the pseudorapidity coverage to  $|\eta| = 5.2$ .

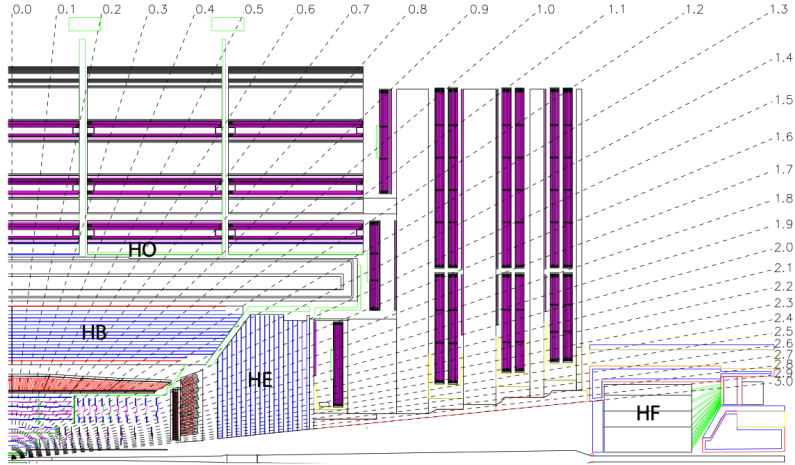


Figure 2.5: Longitudinal view of the CMS detector showing the hadron calorimeter barrel (HB), endcap (HE), outer (HO), and forward (HF) calorimeters from [21].

855        The HB is a sampling calorimeter covering the pseudorapidity range  $|\eta| < 1.3$  [21].  
 856        It consists of 36 identical azimuthal wedges which form two half-barrels (HB+ and HB-  
 857      ), with a segmentation of  $(\Delta\eta, \Delta\phi) = (0.087, 0.087)$ . The HE covers pseudorapidity  
 858       $1.3 < |\eta| < 3$ . The HB and endcap HE calorimeters are sampling calorimeters which  
 859      use brass as the absorber and plastic scintillator as the active material. Light from  
 860      the plastic scintillator is wavelength-shifted and captured in optic fibers which are  
 861      read out by front-end electronics [27].

862        The HF is a Cherenkov calorimeter based on a steel absorber and quartz fibers  
 863      which run longitudinally through the absorber and collect Cherenkov light, primarily  
 864      from the electromagnetic component of showers developed in the calorimeter [27].  
 865      Photomultiplier tubes are used to collect light from the quartz fibers. The HF is  
 866      designed to survive in the harsh radiation conditions and high particle flux of the for-  
 867      ward region. On average, 760 GeV per proton-proton interaction is deposited into the  
 868      two forward calorimeters, compared to only 100 GeV for the rest of the detector [21].  
 869      Furthermore, this energy has a pronounced maximum at the highest rapidities.

870 **2.5.4 Muon detectors**

871 The CMS muon system is designed to have the capability of reconstructing the mo-  
872 mentum and charge of muons over the kinematic range of the LHC, since muons are a  
873 powerful handle on signatures of interesting processes over the high background rate  
874 of the LHC [21]. For instance, the decay of the Standard Model Higgs boson into  
875  $ZZ$ , which in turn decay to 4 leptons, can be reconstructed with high 4-particle mass  
876 resolution if all the leptons are muons, since muons are less affected than electrons  
877 by radiative losses in the tracker material.

878 The muon system consists of a cylindrical barrel section and two planar endcap  
879 regions [21]. The barrel muon detector consists of drift tube (DT) chambers covering  
880 the pseudorapidity region  $|\eta| < 1.2$  (Fig. 2.6). The DTs can be used as tracking  
881 detectors due to the barrel region's characteristic low neutron-induced backgrounds,  
882 low muon rate, and relatively uniform 4T magnetic field contained in the steel yoke.

883 In the two endcap regions, the muon rates and background levels are high and the  
884 magnetic field is large and non-uniform [21]. Here, the muon system uses cathode  
885 strip chambers (CSCs) to identify muons between  $0.9 < |\eta| < 2.4$ . The cathode strips  
886 of each chamber run radially outwards and provide a precision measurement in the  
887  $r - \phi$  bending plane. The anode wires run approximately perpendicular to the strips  
888 and are read out in order to measure  $\eta$  and the beam-crossing time of a muon.

889 In addition to the DT and CSC, a dedicated trigger system consisting of resistive  
890 plate chambers (RPCs) in the barrel and endcap regions provide a fast, independent,  
891 and highly-segmented trigger with a sharp  $p_T$  threshold over a large portion of the  
892 pseudorapidity range ( $|\eta| < 1.6$ ) of the muon system [21]. RPCs have good time  
893 resolution but coarser position resolution compared to the DTs or CSCs. The RPCs  
894 also play a role in resolving ambiguities in reconstructing tracks from multiple hits in  
895 a chamber.

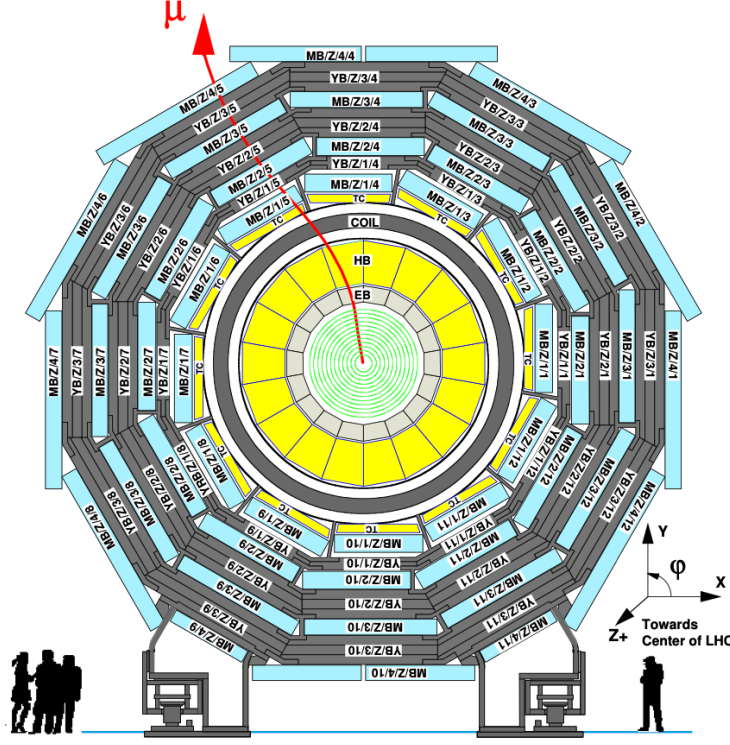


Figure 2.6: Layout of the CMS barrel muon drift tube (DT) chambers in one of the five wheels from [21]. The DTs are organized in 12 sectors of the yoke barrel (YB). In each of the 12 sectors of the yoke, there are 4 muon chambers per wheel (MB1, MB2, MB3, and MB4).

### 2.5.5 The Level-1 Trigger

The design performance of the LHC corresponds to an instantaneous luminosity of  $10^{34} \text{ cm}^{-2} \text{ s}^{-1}$  with a 25 ns bunch crossing rate, giving an average pile-up (number of simultaneous events) of 25 per bunch crossing [28]. However, during Run 2, in 2017 and 2018 the LHC was able to surpass this goal with a mean number of 32 interactions per bunch crossing, and reaching over 50 interactions in short periods (Fig. 2.2). The large number of events from inelastic collisions (minimum bias events) per bunch crossing, combined with the small cross-sections of possible physics discovery signatures, necessitates a sophisticated event selection system for filtering this large event rate, as it is impossible to save all events. This data filtering system is imple-

mented by CMS in two stages. The first stage is the Level-1 (L1) Trigger, which is deployed in custom electronic hardware systems and is responsible for reducing the event rate to around 100 kHz. The second stage is the High-Level Trigger (HLT) which is described in Section 2.5.6. This section describes the Phase-1 configuration of the Level-1 Trigger.

The L1 Trigger data flow of Phase-1 is shown in Fig. 2.7 [28], with organization into the L1 calorimeter trigger, the L1 muon trigger, and the L1 Global Trigger (GT).

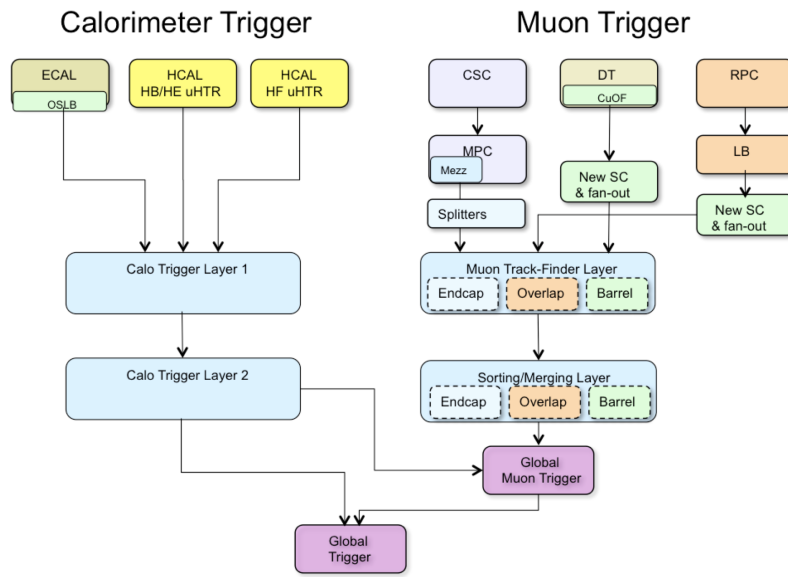


Figure 2.7: Dataflow for the Phase-1 Level-1 Trigger [28], which is implemented in custom hardware and is responsible for reducing the event rate from the LHC bunch crossing frequency of 400 MHz (bunch crossings every 25 ns) to a maximum rate of 100 kHz. In Phase-1, the Level-1 Trigger has access to information from the calorimeter and muon detectors.

The L1 calorimeter trigger begins with trigger tower energy sums formed by the ECAL, HCAL, and HF Trigger Primitive Generator (TPG) circuits from the individual calorimeter cell energies. In the original configuration, the ECAL energies were accompanied by a bit indicating the transverse extent of the electromagnetic energy deposits, and the HCAL energies were accompanied by a bit indicating the presence of minimum ionizing energy [29]. During Long Shutdowns 1 and 2 (LS1

919 and LS2), HF was upgraded to provide finer granularity information to the trigger,  
920 and the HCAL barrel and endcap front-end electronics were upgraded to provide  
921 high-precision timing information and depth segmentation information.

922 In the original design of the L1 calorimeter trigger, the trigger primitives are pro-  
923 cessed by the Regional Calorimeter Trigger (RCT, upgraded to Calo Layer 1 after  
924 LS2) which finds isolated and non-isolated electron/photon candidates [28]. At this  
925 stage, electrons/photons candidates are treated together since they cannot be defini-  
926 tively distinguished at this stage due to lack of tracking information in the L1 trigger.  
927 The Global Calorimeter Trigger (GCT, upgraded to Calo Layer 2 after LS2) sorts  
928 further the candidate electrons/photons, finds jets (classified as central, forward, and  
929 tau) using the  $E_T$  sums and performs calibration of the clustered jet energies, and  
930 calculates global quantities such as missing  $E_T$ . It sends the top four candidates of  
931 each type to the Global Trigger [28].

932 During LS2 and before Run-2, the legacy calorimeter trigger was upgraded to be  
933 more flexible, maintainable, and performant [30] [31] [32]. These upgrades included  
934 the replacement of legacy VME-based electronics with the microTCA modern tele-  
935 coms standard, and system-wide usage of the latest generation of FPGAs, Xilinx  
936 Virtex 7. Parallel copper links were replaced in almost all cases with serial optical  
937 links, allowing link speeds to increase from 1 Gb/s to 10 Gb/s [30]. A schematic of  
938 the current calorimeter trigger is shown in Fig. 2.8. The calorimeter Layer-1 is imple-  
939 mented in 18 Calorimeter Trigger Processor (CTP7) boards, with each card spanning  
940 4 out of 72 towers in  $\phi$  and all of  $\eta$ . Tower-level operations are performed in Layer-1,  
941 such as the sum of ECAL and HCAL energies, energy calibration, and the compu-  
942 tation of the ratio of HCAL to ECAL energies. The Layer-1 cards each transmit 48  
943 output links at 10 Gb/s to the nine Layer-2 Master Processor cards (MP7) cards,  
944 which host calorimeter algorithms that find particle candidates and compute global  
945 energy sums. Each MP7 takes 72 input links and has access to the whole event at

trigger tower granularity, such that the algorithms are fully pipelined and start processing as soon as the minimum amount of data is received. The trigger candidates are sent to a demultiplexer (demux) board, also a MP7, which formats the data for the upgraded Global Trigger, also called the microGT ( $\mu$ GT).

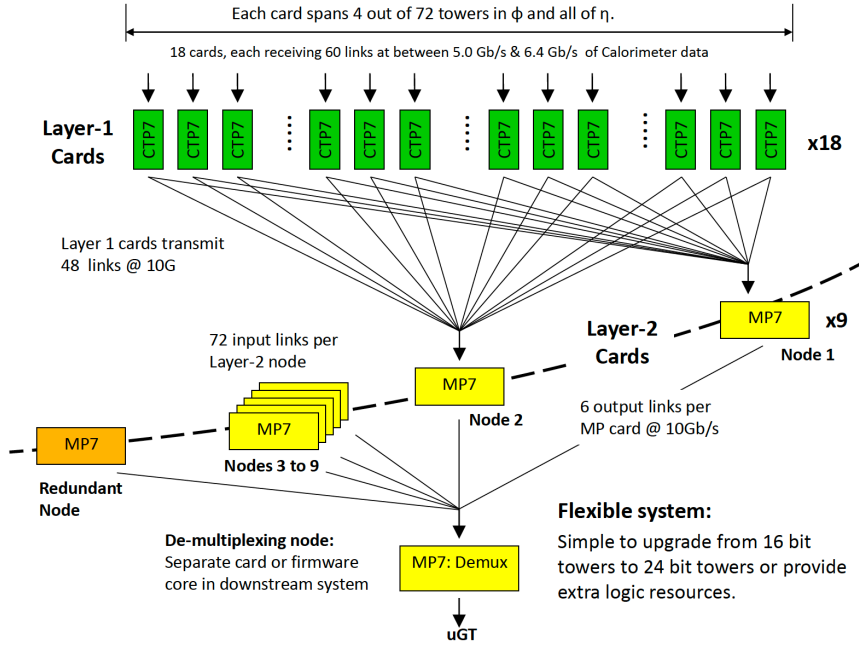


Figure 2.8: Schematic of the calorimeter trigger after Long Shutdown 2 [30]. The Layer-1 calorimeter trigger is implemented in CTP7 cards, which send time-multiplexed outputs to the Layer-2 MP7 cards. The Layer-2 cards handle the data in a round-robin style and the outputs are de-multiplexed, producing one output data stream to the Global Trigger.

Each of the L1 muon triggers has its own trigger logic [29]. The RPC strips are connected to a Pattern Comparator Trigger (PACT), which forms trigger segments that are used to build tracks and calculate  $p_T$ . The RPC logic also provides some hit data to the CSC trigger system to resolve ambiguities caused by two muons in the same CSC. The CSCs form local charged tracks (LCTs) from the cathode strips, which are combined with the anode wire information. LCTs are combined into full muon tracks and assigned  $p_T$  values.

The Global Muon Trigger (GMT) sorts the RPC, DT, and CSC muon tracks,

958 converts these tracks to the same  $\eta$ ,  $\phi$ , and  $p_T$  scale, and validates the muon sign [29].  
959 It improves the trigger efficiency by merging muon candidates that were detected  
960 in two complementary sub-systems (i.e. DT+RPC, or CSC+RPC). The GMT also  
961 contains logic to correlate the found muon tracks with an  $\eta-\phi$  grid of quiet calorimeter  
962 towers to determine if the muons are isolated, as well as logic to remove duplicate  
963 candidates originating in the overlap regions from both DT and CSC systems. The  
964 final collection of muons are sorted based on their initial quality, correlation, and  $p_T$ ,  
965 and the top four muons are sent to the Global Trigger [29].

966 The Global Trigger (GT) receives information from the GCT and GMT, and  
967 makes the Level-1 Accept (L1A) decision to either discard or accept the bunch cross-  
968 ing [29]. This is accomplished by sorting ranked trigger objects that are accompanied  
969 by positional information in  $\eta$  and  $\phi$ , permitting the trigger to applying criteria with  
970 thresholds that can vary based on the location of the trigger objects, and/or to re-  
971 quire trigger objects to be close to or opposite from each other. The GT L1A decision  
972 arrives at the detector front end with a  $3.8\ \mu\text{s}$  latency after the interaction at a rate  
973 which is required to be less than 100 kHz, and triggers a full readout of the detector  
974 for further processing.

### 975 **2.5.6 The High-Level Trigger**

976 The HLT is implemented in software running on a large computer farm of fast com-  
977 mercial processors [33] [34]. The algorithms in HLT have access to full data from  
978 all CMS sub-detectors, including the tracker, with full granularity and resolution.  
979 The HLT reconstruction software is similar to what is used offline for full CMS data  
980 analysis. As a result, the HLT can calculate quantities with a resolution compara-  
981 ble to the final detector resolution, compared to the L1 Trigger. The HLT performs  
982 more computationally-intensive algorithms, such as combining tau-jet candidates in  
983 the calorimeter with high- $p_T$  stubs in the tracker, to form a hadronic tau trigger. The

984 maximum HLT input rate from the L1 Trigger is 100 kHz, and the HLT output rate  
985 is approximately 100 Hz.

986 The HLT contains trigger paths, each corresponding to a dedicated trigger [35].  
987 A path consists of several steps implemented as software modules. Each HLT trigger  
988 path must be seeded by one or more L1 trigger bits: the first module always looks  
989 for a L1 seed, consisting of L1 bit(s) and L1 object(s). Each module performs a well-  
990 defined task such as unpacking (raw to digitized quantities), reconstruction of physics  
991 objects (electrons, muons, jet, missing transverse energy, etc.), making intermediate  
992 decisions that trigger more detailed reconstruction modules, and calculating the final  
993 decision for the trigger path. If an intermediate filter decision is negative, the rest of  
994 the path is not executed, and the trigger rejects the event.

### 995 **2.5.7 Particle reconstruction**

996 To build a description of the physics objects present in the particle collision, the  
997 basic elements from the detector layers (tracks and clusters of energy) are correlated  
998 to identify each particle in the final state. Measurements from different sub-detectors  
999 are combined to reconstruct the particle properties. This approach is called particle-  
1000 flow (PF) reconstruction [22]. Key to the success of the PF reconstruction is the  
1001 fine spatial granularity of the detector layers. Coarse-grained detectors can cause  
1002 the signals from different particles to merge, especially within jets. However, if the  
1003 subdetectors are sufficiently segmented to separate individual particles, it becomes  
1004 possible to produce a global event description that identifies all physics objects with  
1005 high efficiencies and resolution.

### 1006 **2.5.8 Data storage and computational infrastructure**

1007 The LHC generates over 15 petabytes (15 million gigabytes) of data every year, neces-  
1008 sitating a flexible computing system that can be accessed by researchers working at

1009 the four main LHC experiments: ALICE, ATLAS, CMS, and LHCb. The Worldwide  
1010 LHC Computing Grid (WLCG) [36] is a global collaboration of computer centers that  
1011 links thousands of computers and storage systems in over 170 centers across 41 coun-  
1012 tries. These centers are arranged in “tiers”, and provide near real-time access to users  
1013 processing, analyzing, and storing LHC data. One of the final stages of data analy-  
1014 sis at LHC experiments is large-scale data processing taking place over distributing  
1015 computing, for instance, with the use of Condor [37], a distributed, scalable, flexible  
1016 batch processing system which accepts a computing job, allocates a resource to it,  
1017 executes it, and returns the result back to a user transparently.

1018 **Chapter 3**

1019 **The Phase-2 Upgrade of CMS**

1020 This chapter gives an overview of the High-Luminosity LHC upgrade of the LHC in  
1021 Section 3.1, and the upgrades for the Phase-2 CMS Level-1 (L1) Trigger in Section  
1022 3.2. One of the major upgrades is the new availability of calorimeter crystal-level  
1023 information to the L1 calorimeter trigger, compared to the current trigger which only  
1024 has access to tower-level information (a tower being 5 by 5 in crystals). To capitalize  
1025 on the increased spatial granularity of this information, an upgraded algorithm is  
1026 presented which reconstructs and identifies electron and photon candidates in the the  
1027 Layer-1 Calorimeter Trigger. A description of the algorithm and a validation of its  
1028 performance in Phase-2 conditions is given in Section 3.3.

1029 **3.1 The High-Luminosity LHC**

1030 In order to sustain and extend the LHC’s physics discovery program and maintain  
1031 operability for a decade or more, the LHC is undergoing a major upgrade to the High-  
1032 Luminosity LHC (HL-LHC). In its final configuration, the HL-LHC will deliver a peak  
1033 luminosity of  $7.5 \times 10^{34} \text{ cm}^{-2} \text{ s}^{-1}$ , potentially leading to total integrated luminosity  
1034 of  $4000 \text{ fb}^{-1}$  after ten years of operations, scheduled to begin in 2027 [38]. This  
1035 integrated luminosity is about ten times the predicted luminosity reach of the LHC

1036 in its initial configuration. To enable the CMS experiment to continue operations and  
1037 data-taking and to maximize the discovery potential of the unprecedented amount  
1038 of data, the CMS detector is undergoing Phase-2 upgrades in order to perform high-  
1039 precision measurements and searches for physics beyond the Standard Model in the  
1040 intense running conditions of the HL-LHC.

## 1041 **3.2 The Phase-2 Level-1 Trigger**

1042 To achieve the goals of the HL-LHC program and to ensure the collection of information-  
1043 rich datasets in the HL-LHC, the Phase-2 upgrade of the CMS Level-1 Trigger [38]  
1044 must be upgraded in conjunction with the CMS sub-detectors and their readouts, to  
1045 maintain physics selectivity. The HL-LHC will produce an intense hadronic environ-  
1046 ment corresponding to 200 simultaneous collisions per beam crossing, necessitating  
1047 comprehensive upgrades of the trigger system outlined below.

1048 In order to cope with the increased pile-up and high occupancies of the HL-LHC,  
1049 the latency of the L1 trigger system (time available to produce a L1 Accept signal) will  
1050 be increased significantly from  $3.8 \mu\text{s}$  to  $12.5 \mu\text{s}$ , with an increased maximum output  
1051 bandwidth of 750 kHz [38]. With the increased latency, in addition to information  
1052 from calorimeters and muon detectors (as in the Phase-1 system), information from  
1053 the new tracker and high-granularity endcap calorimeter can also be included at L1  
1054 for the first time. This is illustrated in the functional diagram of the architecture of  
1055 the Phase-2 trigger system in Fig. 3.1.

1056 The key feature of the Phase-2 L1 Trigger is the introduction of a correlator layer,  
1057 where algorithms produce higher-level trigger objects by combining information from  
1058 sub-detectors, with a selectivity approaching that of offline reconstruction in the  
1059 HLT [38]. Four independent data processing paths (grouped together in Fig. 3.1) are  
1060 implemented: tracking, calorimetry, muon systems, and particle-flow techniques:

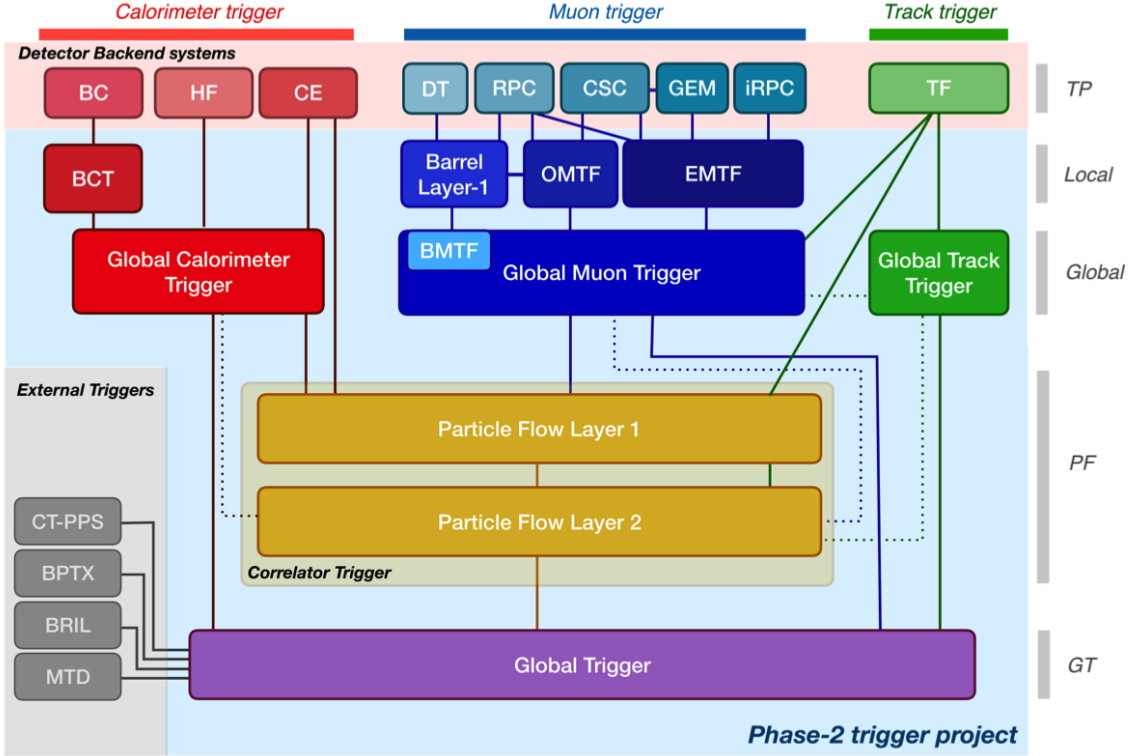


Figure 3.1: Functional diagram of the CMS L1 Phase-2 upgraded trigger design [38], showing the four trigger paths: calorimeter, muon, track, and Particle Flow. For the first time, tracking information will be available as early as the L1 Trigger.

- **Calorimeter Trigger path:** (red, Fig. 3.1) A barrel calorimeter trigger (BCT) and the HGCAL backend are used to process crystal-level information from the calorimeters to produce high-resolution clusters and identification variables used for later processing. Outputs from the BCT, HGCAL, and the HF are sent to a global calorimeter trigger (GCT), where calorimeter-only objects such as  $e/\gamma$  candidates, hadronically decaying tau lepton candidates, jets, and energy sums are built.
- **Track Trigger path:** (green, Fig. 3.1) Tracks from the Outer Tracker are reconstructed in the track finder (TF) processors as part of the detector backend. A global track trigger (GTT) will reconstruct the primary vertices of the event, along with tracker-only based objects, such as jets and missing transverse momentum.

- **Muon Trigger path:** (*blue*, Fig. 3.1) Trigger primitives are processed by muon track finder algorithms, again separated into the barrel (barrel muon track finder, BMTF), overlap (overlap muon track finder, OMTF), and endcap (endcap muon track finder, EMTF). Standalone muons and stubs containing information such as position, bend angle, and timing, as well as L1 tracks, are sent to the global muon trigger (GMT).
- **Particle-Flow Trigger path:** (*yellow*, Fig. 3.1) The correlator trigger (CT) aims to approach the performance of offline Particle Flow, and is implemented in two layers. “Layer-1” produces the particle-flow candidates from matching calorimeter clusters and tracks. “Layer 2” builds and sorts final trigger objects and applies additional identification and isolation criteria.

The outputs from the above trigger paths are combined in the Global Trigger (GT) (*purple*, Fig. 3.1), which calculates the final trigger decision (Level-1 Accept), transmitting it to the Trigger Control and Distribution System (TCDS), which distributes it to the detector backend systems, initiating the readout to the DAQ. The GT also provides the interface to external triggers (*grey*, Fig. 3.1), such as triggers for the precision proton spectrometer (PPS), beam position and timing monitors (BPTX), and luminosity and beam monitoring (BRIL) detectors [38]. The design of the Phase-2 Level-1 Trigger allows for future inclusion of triggering information, for instance information about minimum ionizing particles (MIPs) from the MIP Timing Detector (MTD) [39].

### **3.3 Standalone Barrel Calorimeter electron/photon reconstruction**

The reconstruction and identification of electrons and photons ( $e/\gamma$ ) begin with the trigger primitives of the barrel ECAL and HCAL detectors and endcap HGCAL calorimeters, covering the pseudorapidity region  $|\eta| < 3$ . The barrel and endcap regions of the detector are intrinsically different enough to warrant different approaches to  $e/\gamma$  reconstruction. This work presents a firmware-based emulator for the standalone  $e/\gamma$  reconstruction in the barrel calorimeter (Fig. 3.2). “Standalone” refers to the fact that the tracker information is not used in this particular reconstruction chain. This firmware-based emulator is based on the parallelized, computational logic that will be deployed in the firmware of the Phase-2 Level-1 trigger. The emulator uses fixed-precision integers to represent all values, such as in the computation of cluster energies, and closely mimics the firmware logic which uses arrays and performs computations in flattened loops. It represents an improved, more realistic understanding of the trigger, compared to the previous emulator which used idealized logic such as vector operations, and floats to represent all values [38].

#### **3.3.1 Electron/photon standalone barrel procedure**

In Phase-2, the upgrade of both on-detector and off-detector electronics of the barrel calorimeters’ trigger primitive generator (TPG) will enable the streaming of single crystal data from the on-detector to the backend electronics. Currently in Phase-1, the ECAL and HCAL TPGs is restricted to providing lower-granularity information of trigger tower sums of  $5 \times 5$  crystals to the Level-1 Trigger [38]. A schematic of the geometry of the ECAL barrel in the Phase-2 Regional Calorimeter Trigger (RCT) is shown in Fig. 3.3. The barrel is spanned by 36 RCT cards, each spanning  $17 \times 4$  towers in  $\eta \times \phi$ . Each RCT card is subdivided into five “regions” as shown in Fig.

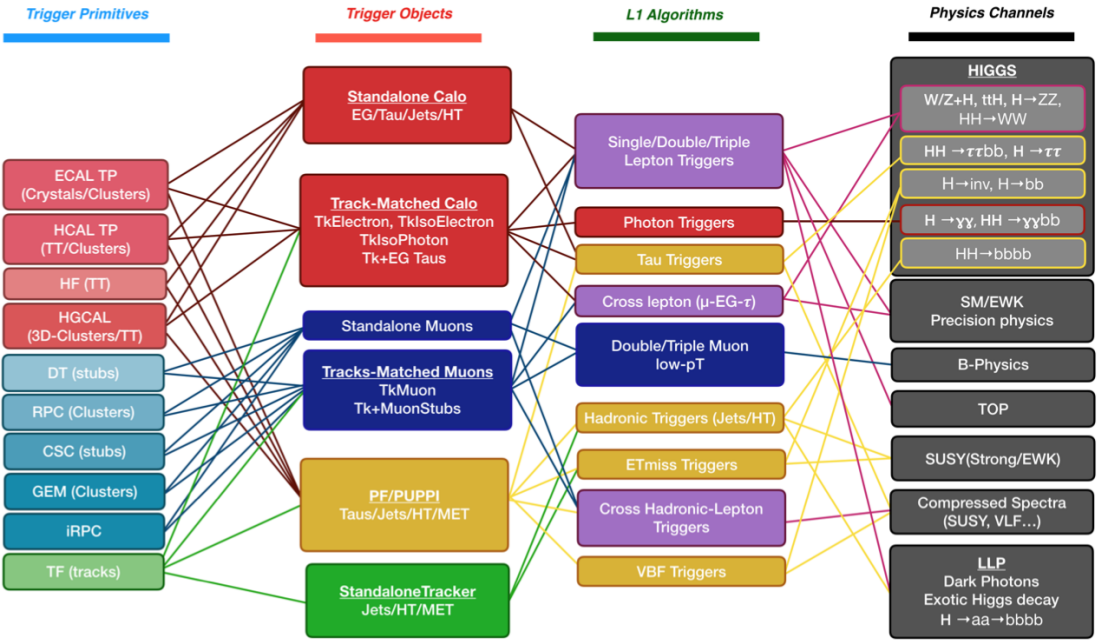


Figure 3.2: Summary of the links between the trigger primitives (*first column*), the trigger objects (*second column*), the Level-1 algorithms used in the menu (*3rd column*), and the physics channels (*4th column*), from [38], where a full description of the Phase-2 L1 algorithms can be found. This work focuses on developments for the Standalone Calorimeter electron and photon ("EG") reconstruction algorithm.

1119     3.4. After initial clustering and processing, the outputs of the RCT card are sent to  
 1120     the Global Calorimeter (GCT) trigger, which is processed in three cards as shown in  
 1121     Fig. 3.5. The reconstruction algorithm is detailed below.

1122     The standalone barrel algorithm for reconstructing and identifying electrons and  
 1123     photons in the Phase-2 Level-1 Trigger takes as input the digitized response of each  
 1124     crystal of the barrel ECAL, with a granularity  $0.0175 \times 0.0175$  in  $\eta \times \phi$ , which is 25  
 1125     times higher than the input to the Phase-1 trigger, which consisted of trigger towers  
 1126     with a granularity of  $0.0875 \times 0.0875$ . In HCAL the tower size of  $0.0875 \times 0.0875$   
 1127     is unchanged. The trigger algorithm is designed to closely reproduce the algorithm  
 1128     used in the offline reconstruction, with limitations and simplifications due to trigger  
 1129     latency.

1130     In the RCT, an initial requirement of  $p_T > 0.5$  GeV is imposed on the input

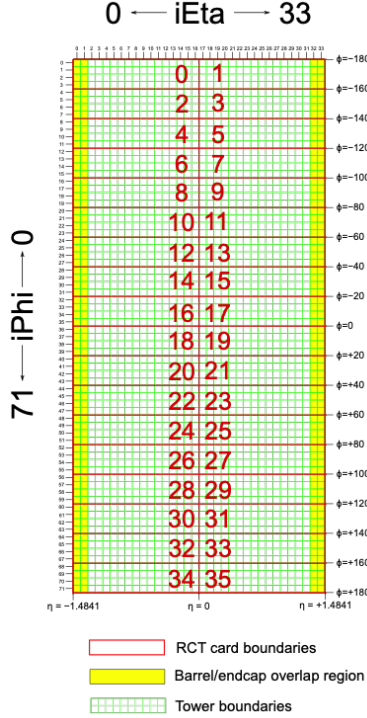


Figure 3.3: Schematic of the geometry of the Phase-2 ECAL barrel in the Regional Calorimeter Trigger (RCT), showing the division of the barrel region into 36 Regional Calorimeter Trigger (RCT) cards (*red*). Each card spans  $17 \times 4$  towers in  $\eta \times \phi$  (*green*), and each tower is  $5 \times 5$  in single crystals in  $\eta \times \phi$ . Towers in the overlap region (*shaded yellow*) are read out to both the barrel and endcap.

trigger primitives (i.e. energies from the ECAL crystals and HCAL towers) to reject contribution from pile-up. In one of the regions inside a RCT card (Fig. 3.4), the crystal containing the highest energy deposit is identified as the seed crystal, as shown in Fig. 3.6. The energy in the crystals in a window of size  $3 \times 5$  in  $\eta \times \phi$  around the seed cluster is added into a cluster. The energy is considered “clustered”. The process is repeated with the remaining “unclustered” energy, until up to four clusters are produced in the region.

To improve  $e/\gamma$  identification and to reduce background contributions, identification and reconstruction algorithms are implemented at this stage:

- Shower shape: The energy deposit sums around the seed crystal is computed in windows of size  $2 \times 5$  and  $5 \times 5$  (Fig. 3.6, *dashed lines*), with true  $e/\gamma$  clusters

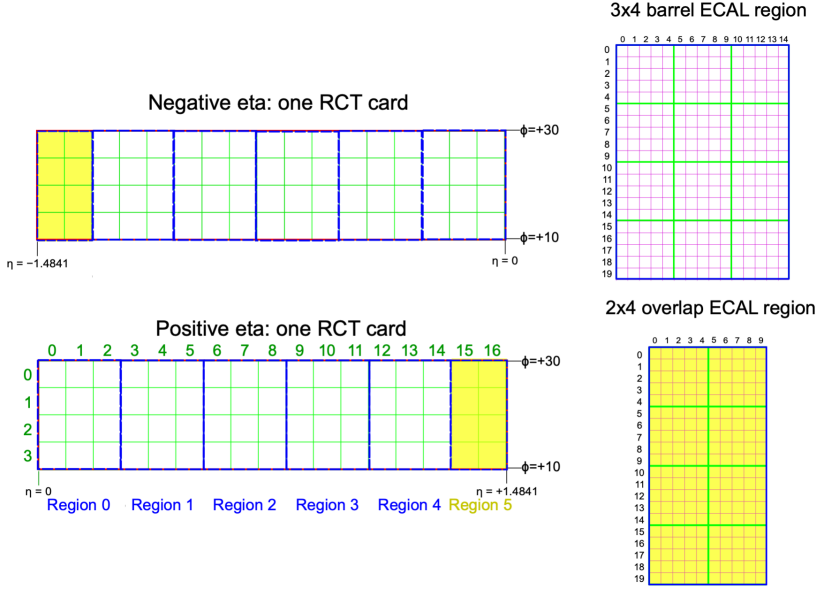


Figure 3.4: Schematic of two example RCT cards in the negative eta (*top left*) and positive eta (*bottom left*) regions of the ECAL barrel. Each RCT card is divided into six regions: five regions are of size  $3 \times 4$  towers in  $\eta \times \phi$  (*top right*), and a sixth smaller overlap region of size  $2 \times 4$  towers (*bottom right*). Each tower is  $5 \times 5$  ( $\eta \times \phi$ ) in crystals.

1142 tending to produce showers that deposit most of their energy in a  $2 \times 5$  region.

- 1143 • Bremsstrahlung recovery:  $e/\gamma$  tend to spread in the  $\phi$  direction due to charged  
 1144 particles being bent by the magnetic field of the CMS solenoid. If sufficient  
 1145 energy comparable to the core  $3 \times 5$  cluster is found in the adjacent  $3 \times 5$   
 1146 windows (Fig. 3.6, *shaded yellow*), the energy is added to the core cluster and  
 1147 no longer considered unclustered energy.

1148 After parallel processing in the regions, the clusters in a RCT card are stitched  
 1149 together if they are located directly along the borders of a region (Fig. 3.3). The  
 1150 remaining unclustered ECAL energy is summed into ECAL towers.

1151 From each RCT card, the twelve highest-energy clusters, as well as any remaining  
 1152 unclustered energy, are sent to the GCT. Since each GCT card has information from  
 1153 sixteen RCT cards (Fig. 3.5), final stitching across the boundaries of the RCT cards  
 1154 is performed. One more identification algorithm is performed at this stage:

## GCT/“Layer 2”

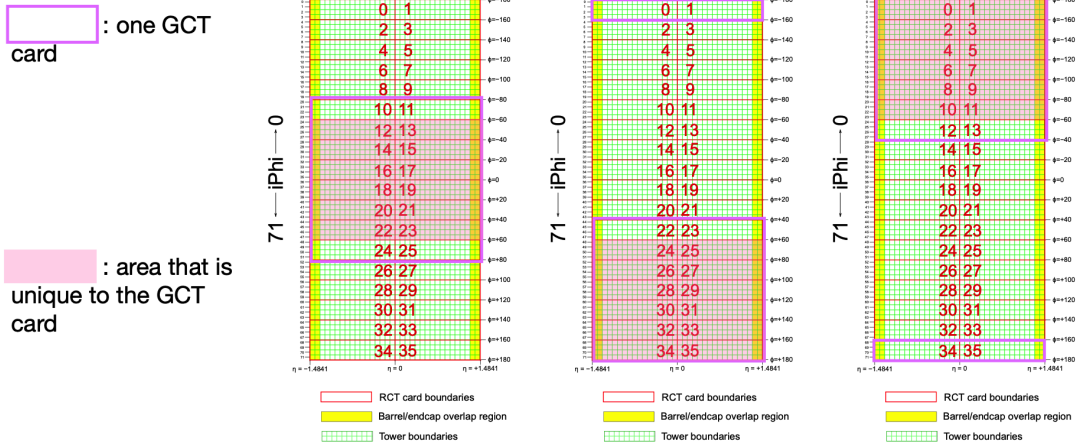


Figure 3.5: Schematic of the Phase-2 ECAL barrel in the Global Calorimeter Trigger (GCT), which will process the outputs of the Regional Calorimeter Trigger (RCT) in three GCT cards (*purple borders*). Each card in the GCT processes the equivalent of sixteen RCT cards, with the center twelve RCT cards being unique to that GCT card (*shaded pink*), and the remaining four RCT cards overlapping with one other GCT card.

- Isolation: One handle to reject backgrounds from e.g. pile-up, comes from the tendency for background to be spread more uniformly across a large area in the detector, whereas genuine  $e/\gamma$  are expected to produce showers concentrated in the  $3 \times 5$  crystal window. The energy sum in a large window of  $7 \times 7$  in towers is computed and used to reject background.

Flags that provide discrimination power between genuine  $e/\gamma$  and background, are computed using the relative isolation and shower shape quantities. The standalone working point (WP) is defined as the logical OR of the relative isolation and shower shape flags.

The information of the clusters in the event, including their energies, crystal-level position, the relative isolation flag, the shower shape flag, the standalone WP, and the ratio of the HCAL over ECAL energies, are sent in 64 bits to the Correlator Trigger and the Global Trigger. The towers in the event are computed as the sum of all unclustered energy in the ECAL with the corresponding HCAL energy at each

### 3x4 barrel ECAL region

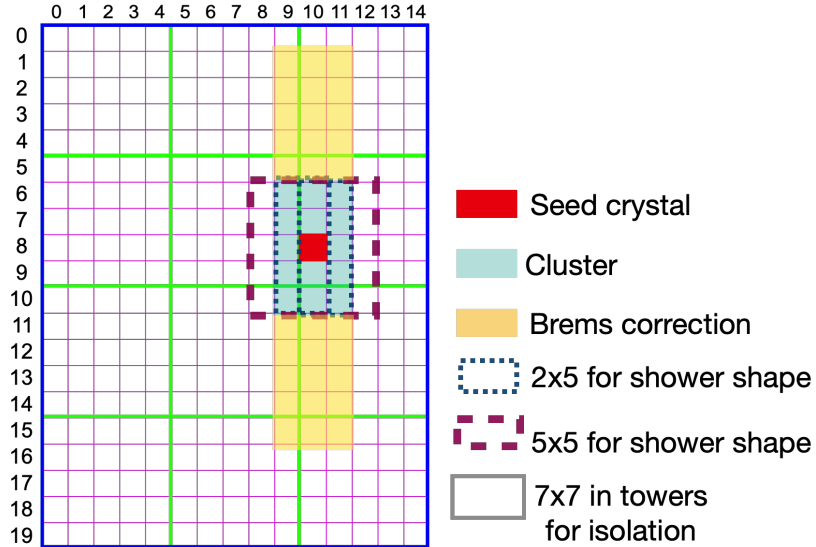


Figure 3.6: Illustration of an example electron/photon ( $e/\gamma$ ) cluster in the Phase-2 Level-1 Trigger standalone barrel  $e/\gamma$  reconstruction, in a region of  $15 \times 20$  crystals ( $3 \times 4$  towers) in  $\eta \times \phi$ . Each small pink square is one crystal, the highest-granularity ECAL trigger primitives available to the L1 Trigger in Phase-2. The core cluster consists of the energy sum in a  $3 \times 5$  window of crystals (*shaded light blue*), centered around the seed crystal (*red*). The presence of energy lost to bremsstrahlung radiation is checked in the adjacent  $3 \times 5$  windows in the  $\phi$  direction (*shaded light yellow*). The ratio of the total energies in windows of size  $2 \times 5$  and  $5 \times 5$  in crystals (*dashed dark blue and dark red*) around the seed crystal, is computed and compared to the core cluster energy to obtain shower shape flags. Lastly, the isolation, defined as the sum of the energy in a large window of size  $7 \times 7$  in towers (not shown in figure) is computed, and compared to the core cluster energy to obtain isolation flags.

<sup>1169</sup> tower location, and their energies are sent to the Correlator Trigger.

#### <sup>1170</sup> 3.3.2 Electron/photon standalone barrel results

<sup>1171</sup> The performance of the current emulator of the standalone barrel  $e/\gamma$  algorithm in  
<sup>1172</sup> Phase-2 conditions is quantified in efficiencies and rates. Efficiency is the fraction of  
<sup>1173</sup> true electrons that the algorithm can reconstruct and identify, and is evaluated in  
<sup>1174</sup> a Monte Carlo simulated sample containing electrons with transverse momentum  $p_T$   
<sup>1175</sup> ranging from 1 to 100 GeV. The efficiencies of the current and previous emulators as

1176 a function of the electron generator-level  $p_T$  are shown in Fig. 3.7.

1177 The rates are the event rates that this reconstruction and identification algorithm  
1178 would obtain if it were deployed in a trigger, assuming that proton-proton collisions  
1179 are occurring at the 40 MHz event rate of the HL-LHC. The rate is reported as a  
1180 function of the minimum energy threshold required by the trigger, and is estimated  
1181 using a simulated sample of minimum bias events, i.e. generic proton-proton colli-  
1182 sions without any specific physics selections. The rates for the current and previous  
1183 emulator are shown in Fig. 3.8.

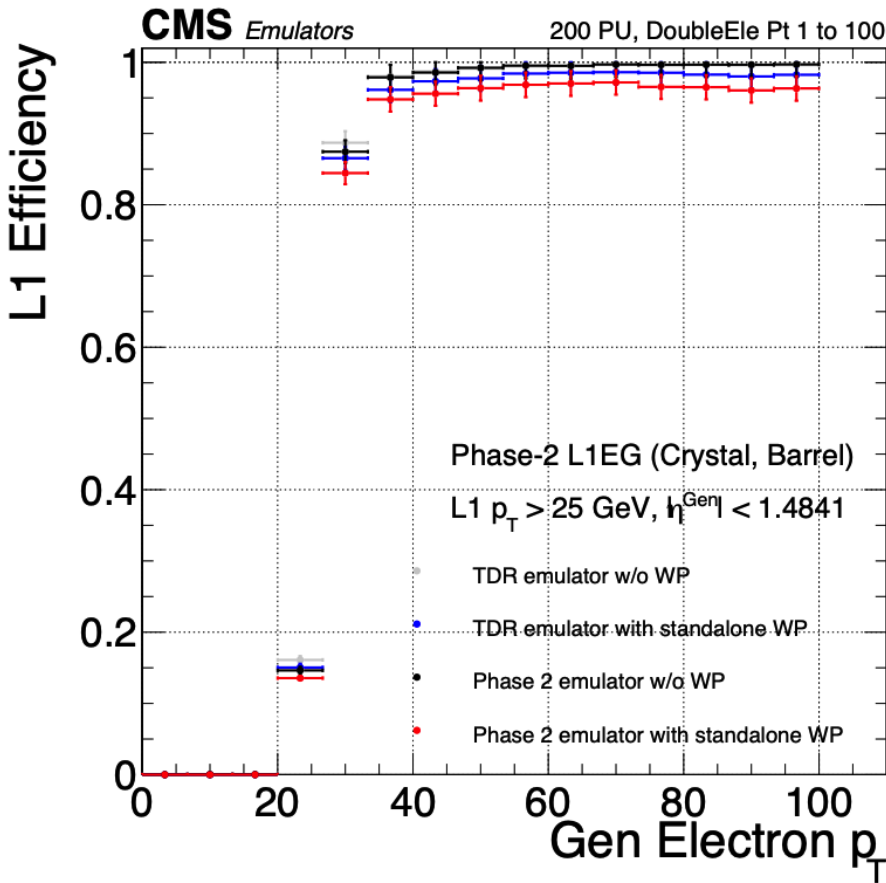


Figure 3.7: Efficiencies of the current and previous emulators of the standalone barrel  $e/\gamma$  algorithm for the Phase-2 Level-1 Trigger, evaluated in a simulated sample containing electrons, as a function of the electron's generator-level transverse momentum  $p_T$ . The standalone working point (WP) is defined as the logical OR of the isolation flag and shower shape flag. The efficiencies with and without requiring the standalone WP, are shown for the current emulator (labeled “Phase 2”, *black, red*) and the previous emulator (labeled “TDR”, *dark blue, grey*).

1184       The current emulator is incorporated into the full Phase-2 L1 menu, allowing an  
1185       estimate of the rates produced by the standalone  $e/\gamma$  barrel trigger path and all  
1186       other algorithms in the L1 Trigger. All rates are estimated with the assumption of  
1187       an average pile-up of 200 and event rate of 40 MHz. The standalone working point  
1188       single  $e/\gamma$  path with requirements on the  $e/\gamma$  candidate to have  $|\eta| < 2.4$ , offline  $p_T$   
1189       to be greater than 51 GeV, and online  $p_T$  to be greater than 41 GeV, is projected to  
1190       have a rate of around 23 kHz. The standalone working point double  $e/\gamma$  path with  
1191       requirements on the two  $e/\gamma$  candidates to have  $|\eta| < 2.4$ , offline  $p_T$  greater than 37  
1192       and 24 GeV, and online  $p_T$  greater than 29 and 18 GeV, is projected to give a rate of  
1193       around 6 kHz. For both paths, the objects efficiency plateau is 99%.

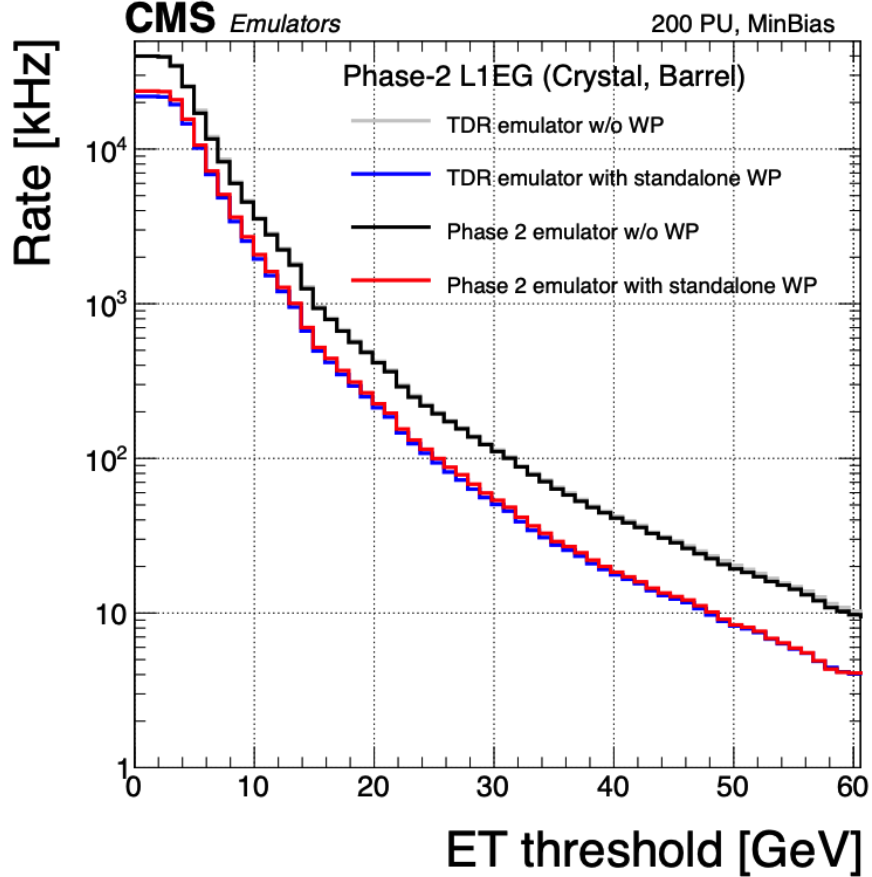


Figure 3.8: Rates in kHz of the current Phase-2 and previous (“TDR”) emulators of the standalone barrel  $e/\gamma$  algorithm for the Phase-2 Level-1 Trigger, evaluated on a minimum bias (MinBias) sample with 200 pile-up (PU), measured as a function of the minimum energy ( $E_T$ ) required of the reconstructed  $e/\gamma$  object in each event. The standalone working point (standalone WP) is defined to be the logical OR of the isolation flag and the shower shape flag. The rates with and without requiring the standalone WP, are shown for the current emulator (labeled “Phase 2”, *black, red*) and the previous emulator (labeled “TDR”, *dark blue, grey*).

1194 **Chapter 4**

1195 **Datasets and Monte Carlo samples**

1196 The search for the exotic decay of the 125 GeV Higgs boson to two light neutral scalars  
1197 decaying to a pair of bottom quarks and a pair of tau leptons ( $h \rightarrow aa \rightarrow bb\tau\tau$ ) is  
1198 based on proton-proton collision data at a center-of-mass energy 13 TeV collected  
1199 in Run-2 of data-taking, spanning the data-taking years 2016, 2017, and 2018. The  
1200 datasets used and the triggers used to collect the data are described in Section 4.1.  
1201 Section 4.2 describes the Monte Carlo simulated samples that are used to model the  
1202  $h \rightarrow aa \rightarrow bb\tau\tau$  signal and background Standard Model processes. Lastly, in order  
1203 to obtain a better description of Standard Model backgrounds that contain two tau  
1204 leptons, a data-Monte Carlo hybrid technique is used to generate embedded samples  
1205 which model processes with genuine  $\tau\tau$  in the final state, as detailed in Section 4.3.  
1206 All samples are listed in Appendix A.

1207 **4.1 Datasets used**

1208 The  $h \rightarrow aa \rightarrow bb\tau\tau$  analysis [40] is based on proton-proton collision data at a center-  
1209 of-mass energy of 13 TeV collected in full Run-2 (2016-18) with the CMS detector.  
1210 The data analyzed corresponds to a total integrated luminosity of  $138 \text{ fb}^{-1}$  ( $36.33 \text{ fb}^{-1}$   
1211 for 2016,  $41.53 \text{ fb}^{-1}$  for 2017, and  $59.74 \text{ fb}^{-1}$  for 2018) [41] [42] [43]. The cumulative

1212 delivered and recorded luminosity versus time for 2015-2018 is shown in Fig. 4.1.

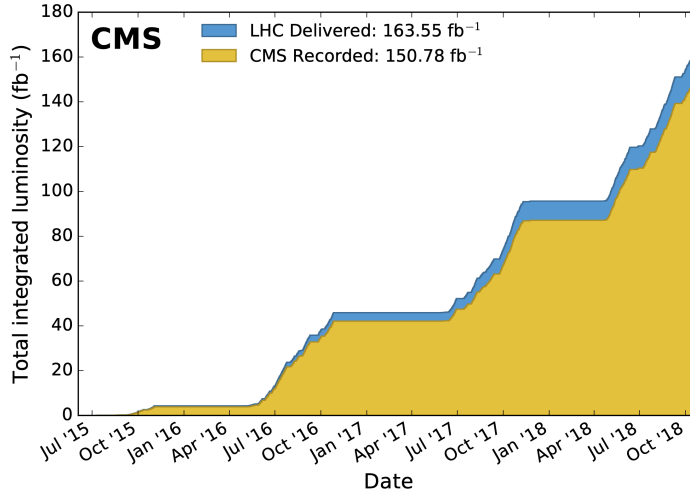


Figure 4.1: Cumulative delivered and recorded luminosity versus time for 2015-2018 at CMS, in proton-proton collision data only, at nominal center-of-mass energy [44].

1213 Data collected with the single muon trigger is used for the  $\mu\tau_h$  channel. For the  
1214  $e\tau_h$  channel, data collected with the single electron trigger is used; and for the  $e\mu$   
1215 channel, data collected with the electron + muon trigger is used. A more in-depth  
1216 discussion of the triggers used follows in a later section. The datasets are listed in  
1217 Appendix A in Tables A.1, A.2, and A.3.

## 1218 4.2 Monte Carlo samples

1219 Modeling and computing observables originating from arbitrary physics processes at  
1220 the tree level and at next-to-leading order (NLO) is performed by Monte Carlo (MC)  
1221 event generators, such as Powheg and MadGraph5\_amCNLO [45] [46]. The informa-  
1222 tion generated, e.g. the computation of the differential cross sections and kinematics  
1223 of the final state particles, is saved in a compressed file and used to generate MC sam-  
1224 ples that are used in physics analyses. The samples are digitized using GEANT4 [47],  
1225 a platform used at the LHC and other facilities to comprehensively simulate the

passage of particles through matter. The digitized samples are passed through the same detector reconstruction as real data events collected in the detector. The MC background samples used in this analysis for 2016-2018 are listed in Appendix A in Tables A.7, A.8, and A.9.

The samples for modeling the signal ( $h \rightarrow aa \rightarrow 2b2\tau$  and  $h \rightarrow a_1a_2$ ) in the 2HDM+S and TRSM are generated at tree-level, for a range of masses of the light neutral scalar  $a$ . For  $h \rightarrow aa$ , the mass hypotheses for the  $a$  range from  $m_a = (12\text{ GeV}, 62.5\text{ GeV})$ . For  $h \rightarrow a_1a_2$ , the mass hypotheses for the two light scalars span combinations of  $m_{a1}$ ,  $m_{a2}$  ranging from  $(12\text{ GeV}, 62.5\text{ GeV})$  for the two scalars. The MC signal samples used in this analysis for 2016-2018 are listed in Appendix A in Tables A.10, A.11 and A.12.

### 4.3 Embedded samples

An important background for Higgs boson studies and searches for additional Higgs bosons is the decay of  $Z$  bosons into pairs of  $\tau$  leptons ( $Z \rightarrow \tau\tau$ ). An embedded technique was developed in the context of Standard Model Higgs to  $\tau\tau$  measurements, to model  $Z \rightarrow \tau\tau$  decays, and was expanded to also model all Standard Model processes that contain  $\tau\tau$  [48]. The embedded technique has since been used successfully at CMS for the Standard Model  $H \rightarrow \tau\tau$  measurement, as well as searches for minimal supersymmetric extensions to the Standard Model (MSSM) [49] [50].

The advantage of the embedded technique is that aspects of the event that are difficult to model and describe are directly taken from data, resulting in a better data description than can be achieved with only the  $Z \rightarrow \tau\tau$  simulation [48]. The simulation must be tuned extensively to accurately model aspects of the data, such as time-dependent pile-up profiles, the production of additional jets, e.g. in multijet and vector boson fusion topologies, the number of reconstructed primary interaction

1251 vertices, and the missing transverse momentum  $p_T^{\text{miss}}$ . Since all events with genuine  
 1252  $\tau\tau$  are estimated with samples made with the embedded technique (referred to as  
 1253 embedded samples from here on), events in Monte Carlo simulation with genuine  $\tau\tau$   
 1254 are not used, in order to avoid double-counting.

1255 Fig. 4.2 shows a schematic of how embedded samples are produced. Data events  
 1256 containing  $Z \rightarrow \mu\mu$  decays are selected. In these events, all energy deposits of the  
 1257 recorded muons are removed, and are replaced with simulated tau leptons with the  
 1258 same kinematic properties as the removed muons. This results in a hybrid data format  
 1259 containing information from both observed and simulated events, as illustrated in Fig.  
 1260 4.2 [48]. The embedded samples used for the years 2016-2018 are listed in Appendix  
 1261 A in Tables A.4, A.5, and A.6.

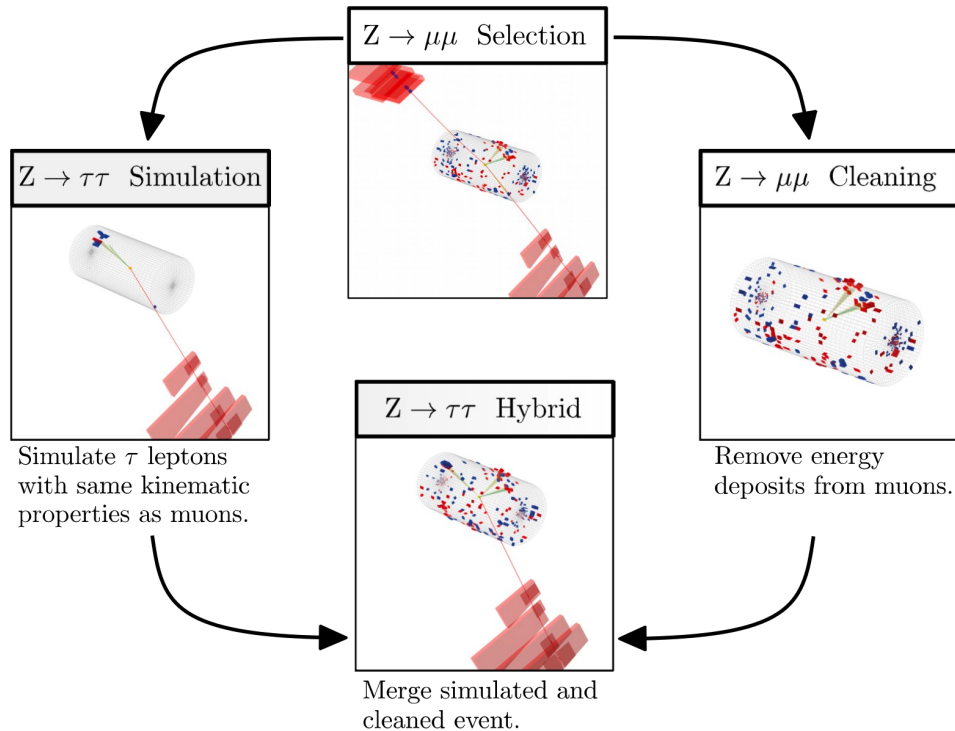


Figure 4.2: Schematic view of the four main steps of the embedding technique for  $\tau$  leptons, as described in Section 4.3 [48]. A  $Z \rightarrow \mu\mu$  event is selected in data ( $Z \rightarrow \mu\mu$  selection), all of the energy deposits associated with the muons are removed ( $Z \rightarrow \mu\mu$  cleaning), and two  $\tau$  leptons and their decays are simulated in an empty detector ( $Z \rightarrow \tau\tau$  simulation). Lastly, all energy deposits of the simulated  $\tau$  decays are combined with the data event ( $Z \rightarrow \tau\tau$  hybrid).

1262 In the selection step of the embedded technique, events are selected with one of a  
 1263 set of  $\mu\mu$  trigger paths, which require  $p_T > 17(8)$  GeV for the leading (sub-leading)  
 1264 muons, and a minimum requirement between 3.8 and 8.0 GeV on the invariant di-  
 1265 muon mass  $m_{\mu\mu}$  [48]. The offline reconstructed muons must match the objects at  
 1266 trigger level and also have offline  $p_T > 17(8)$  GeV. They must have  $|\eta| < 2.4$  and be  
 1267 located at a distance  $|d_z| < 0.2$  cm to the primary vertex along the beam axis. To form  
 1268 a Z boson candidate, each muon is required to originate from a global muon track.  
 1269 The muon pairs must have opposite charges with an invariant mass of  $m_{\mu\mu} > 20$  GeV.  
 1270 If more than two di-muon pairs are found, the pair with the invariant mass closest to  
 1271 the Z boson mass (91.19 GeV) is chosen.

1272 This selection is designed to be tight enough to ensure a high purity of genuine  
 1273  $\mu\mu$  events, and also loose enough to minimize biases of the embedded event samples.  
 1274 Isolation requirements are avoided, since they would introduce a bias towards less  
 1275 hadronic activity in the vicinities of the embedded leptons that will appear more  
 1276 isolated than expected in data. The selection results in an expected mixture of events  
 1277 summarized in Table 4.1 from [48].  $Z \rightarrow \mu\mu$  is the dominant process modeled by the  
 1278 embedded technique, with  $t\bar{t}$ , QCD, and diboson and single top processes becoming  
 1279 more significant when considering events with b-tag jets.

Process	Fraction (%)		
	Inclusive	$m_{\mu\mu} > 70$ GeV	$N(\text{b-tag jets}) > 0$
$Z \rightarrow \mu\mu$	97.36	99.11	69.25
QCD	0.84	0.10	2.08
$t\bar{t}$	0.78	0.55	25.61
$Z \rightarrow \tau\tau$	0.71	0.05	0.57
Diboson, single t	0.17	0.17	2.35
W+jets	0.08	0.02	0.14

Table 4.1: Expected event composition after selecting two muons in the embedded technique [48], before additional cuts (i.e. inclusive, *column 2*), and after adding a requirement on the di-muon mass  $m_{\mu\mu} > 70$  GeV (*column 3*), or a requirement on the number of b-tag jets in the event (*column 4*).

<sub>1280</sub> **Chapter 5**

<sub>1281</sub> **Object reconstruction and**  
<sub>1282</sub> **corrections applied**

<sub>1283</sub> In the data processing workflow, data events and simulated events are analyzed to  
<sub>1284</sub> reconstruct physics objects of interest, and algorithms for distinguishing genuine par-  
<sub>1285</sub> ticle candidates from background, are employed. Section 5.1 describes the physical  
<sub>1286</sub> properties of the most important objects in the  $h \rightarrow aa \rightarrow bb\tau\tau$  analysis: taus,  
<sub>1287</sub> muons, electrons, jets, and jets originating from b-quarks (b-flavor jets), as well as  
<sub>1288</sub> their reconstruction and identification in CMS. In this analysis, the full energy and  
<sub>1289</sub> momentum of the two tau leptons ( $m_{\tau\tau}$ ) is estimated from the measured (i.e. visible)  
<sub>1290</sub> components of the tau leptons using the SVFit/FastMTT algorithm, which is de-  
<sub>1291</sub> scribed in Section 5.2. Corrections are applied to the simulated samples at the object  
<sub>1292</sub> level and the event level to account for known discrepancies between simulations and  
<sub>1293</sub> the data that the simulations are intended to model. These corrections are listed and  
<sub>1294</sub> detailed in Section 5.3.

1295    **5.1 Object reconstruction**

1296    **5.1.1 Taus**

1297    The tau ( $\tau$ ) is the heaviest known lepton. With a rest mass of 1776.86 MeV, it can  
1298    decay to not only electrons and muons, but also hadrons. In two thirds of the cases,  $\tau$   
1299    leptons decay hadronically, typically into one or three charged mesons (predominantly  
1300     $\pi^+$ ,  $\pi^-$ ), often accompanied by neutral pions (that decay  $\pi^0 \rightarrow \gamma\gamma$ ), and a  $\nu_\tau$ . These  
1301    hadronic decays are denoted  $\tau_h$ . In the remainder of the decays, the tau decays to  
1302    the lighter leptons (electron or muon), termed leptonic decays. The mean lifetime of  
1303    the  $\tau$  is  $\tau = 290 \times 10^{-15}$  seconds, corresponding to  $c\tau = 87.03 \mu\text{m}$ , which is short  
1304    enough that taus decay in the CMS detector before reaching the detector elements,  
1305    but also long enough that some decay length variables can help with hadronic tau  
1306    identification. The tau's largest decay branching ratios (proportional to probability  
1307    of decay) are listed below [26]:

- 1308        • 17.8% decay to  $e^- \bar{\nu}_e \nu_\tau$
- 1309        • 17.4% decay to  $\mu^- \bar{\nu}_\mu \nu_\tau$
- 1310        • 25.5% decay to  $\pi^- \pi^0 \nu_\tau$  ( $\rho^-$  resonance at 770 MeV)
- 1311        • 10.8% decay to  $\pi^- \nu_\tau$
- 1312        • 9.3% decay to  $\pi^- \pi^0 \pi^0 \nu_\tau$  ( $a_1^-$  resonance at 1200 MeV)
- 1313        • 9.0% decay to  $\pi^- \pi^- \pi^+ \nu_\tau$  ( $a_1^-$  resonance at 1200 MeV)

1314    In all cases, at least one neutrino is produced. The neutrinos escape undetected  
1315    from the CMS detector, resulting in missing transverse energy. Charged hadrons leave  
1316    tracks in the tracking detector before being absorbed in the hadronic calorimeter; in  
1317    CMS tau reconstruction terminology, they are often called “prongs”, i.e. the dominant

<sub>1318</sub>  $\tau_h$  decay modes are termed “1 prong” ( $\pi^\pm$ ), “1 prong +  $\pi^0$ (s)”, and “3-prong”. Neutral  
<sub>1319</sub> pions decay to two photons which lose their energy in the electromagnetic calorimeter.  
<sub>1320</sub> Taus that decay to electrons and muons, are typically triggered on and reconstructed  
<sub>1321</sub> as electrons and muons respectively.

<sub>1322</sub> **Hadron plus strips (HPS) reconstruction of  $\tau_h$**

<sub>1323</sub> At CMS, hadronically decaying tau leptons are reconstructed with the hadron plus  
<sub>1324</sub> strips (HPS) algorithm [51] [52]. The HPS algorithm capitalizes on photon conversions  
<sub>1325</sub> in the CMS tracker material, which originate from the neutral pion ( $\pi^0$ ) decaying  
<sub>1326</sub> to two photons. The bending of electron/positron tracks due to the CMS solenoid  
<sub>1327</sub> magnetic field leads to a spread of the neutral pions’ calorimeter signatures in the  $\phi$   
<sub>1328</sub> direction. This motivates the reconstruction of photons in “strips”: objects that are  
<sub>1329</sub> built out of PF photons and electrons. The strip reconstruction starts with centering  
<sub>1330</sub> a strip on the most energetic electromagnetic particle in a PF jet. Among other  
<sub>1331</sub> electromagnetic particles located in a window of size  $\Delta\eta = 0.05$  and  $\Delta\phi = 0.20$   
<sub>1332</sub> around the strip center, the most energetic one is associated with the strip and its  
<sub>1333</sub> momentum is added to the strip momentum. This is repeated iteratively until no  
<sub>1334</sub> further particles can be associated. Lastly, strips satisfying a requirement of  $p_T^{\text{strip}} > 1$   
<sub>1335</sub> GeV are combined with charged hadrons to reconstruct individual  $\tau_h$  decay modes,  
<sub>1336</sub> where  $h$  stands for both  $\pi$  and  $K$ :

- <sub>1337</sub> • *Single hadron:*  $h^- \nu_\tau$  and  $h^- \pi^0 \nu_\tau$  decay modes, in which the neutral pions have  
<sub>1338</sub> too little energy to be reconstructed as strips.
- <sub>1339</sub> • *One hadron + one strip:*  $h^- \pi^0 \nu_\tau$  decay modes, where the photons from the  $\pi^0$   
<sub>1340</sub> decay are close together in the calorimeter.
- <sub>1341</sub> • *One hadron + two strips:*  $h^- \pi^0 \nu_\tau$  decay modes, where the photons from the  $\pi^0$   
<sub>1342</sub> decay are well separated.

- 1343       • *Three hadrons:*  $h^-h^+h^-\nu_\tau$  decay modes. The three charged hadrons are re-  
1344              quired to originate from the same secondary vertex.

1345 The  $h^-\pi^0\pi^0\nu_\tau$  and  $h^-h^+h^-\pi^0\nu_\tau$  decay modes do not have their own treatment are  
1346 reconstructed with the above topologies.

1347 In the HPS algorithm, the direction of the reconstructed tau momentum  $\vec{p}^{\tau_h}$   
1348 is required to fall within a distance of  $\Delta R = 0.1$  from the original PF jet. All  
1349 charged hadrons and strips are required to be contained within a cone of size  $\Delta R =$   
1350  $(2.8 \text{ GeV})/p_T^{\tau_h}$ , from the  $\tau_h$  as reconstructed by the HPS.

1351 All charged hadrons are assumed to be pions, and they are required to be consis-  
1352 tent with the masses of the intermediate meson resonances (if applicable), with the  
1353 following allowed windows for candidates: 50-200 MeV for  $\pi^0$ , 0.3-1.3 GeV for  $\rho$ , and  
1354 0.8-1.5 GeV for  $a_1$ . If the  $\tau_h$  decay is compatible with more than one hypothesis, the  
1355 one giving the highest  $p_T^{\tau_h}$  is chosen. Lastly, an isolation requirement is applied: aside  
1356 from the  $\tau_h$  decay products, no charged hadrons or photons can be present within  
1357 an isolation cone of size  $\Delta R = 0.5$  around the direction of the  $\tau_h$ . The outputs of  
1358 the HPS algorithm are the reconstructed decay mode and the visible four-momentum  
1359 (i.e. the four-momenta of all decay products excluding the neutrinos).

1360 **DeepTau for identifying  $\tau_h$**

1361 The identification of  $\tau_h$  candidates in CMS has historically been divided into separate  
1362 discriminators against jets, electrons, and muons. Discriminators versus jets and  
1363 electrons use information from derived quantities, such as the  $p_T$  sum of particles  
1364 near the  $\tau_h$  axis. Building on the previous multivariate analysis (MVA) classifier [53]  
1365 based on a boosted decision tree (BDT), DeepTau is a more recent classifier based on a  
1366 deep neural network (DNN) that simultaneously discriminates against jets, electrons,  
1367 and muons. The DNN uses a combination of high-level inputs, similar to previous  
1368 algorithms, and also uses convolutional layers in  $\eta$ - $\phi$  space to process information

1369 from all reconstructed particles near the  $\tau_h$  axis. Convolutional layers are based on  
1370 the principle that an image can be processed independently of its position.

1371 The final DeepTau discriminators against jets, muons, and electrons are given by

$$D_\alpha(y) = \frac{y_\tau}{y_\tau + y_\alpha} \quad (5.1)$$

1372 where  $y_\tau$  ( $y_\alpha$ ) are estimates of the probabilities for the  $\tau_h$  candidate to come from  
1373 a genuine  $\tau_h$  (jet,  $\mu$ ,  $e$ ). Working points for each discriminator with different  $\tau_h$   
1374 identification efficiencies are defined for  $D_e$ ,  $D_\mu$ , and  $D_{\text{jet}}$ , for usage in physics analyses  
1375 and derivation of data-to-simulation corrections [54].

### 1376 5.1.2 Muons

1377 Muons are the next lightest lepton after taus, with a mass of 105.66 MeV and a  
1378 mean lifetime of  $\tau = 2.20 \times 10^{-6}$  seconds, or  $c\tau = 658.64$  m. At CMS, muons are  
1379 identified with requirements on the quality of the track reconstruction and on the  
1380 number of measurements in the tracker and the muon systems [55]. In the standard  
1381 CMS reconstruction, tracks are first reconstructed independently in the inner tracker  
1382 (tracker track) and in the muon system (standalone-muon track). Next, these tracks  
1383 are processed in two different methods.

1384 The first is Global Muon reconstruction (outside-in) [55], which fits combined hits  
1385 from the tracker track and standalone-muon track, using the Kalman-filter technique.  
1386 At large transverse momenta,  $p_T \gtrsim 200$  GeV, the global-muon fit can improve the  
1387 momentum resolution compared to the tracker-only fit.

1388 The second is Tracker Muon reconstruction (inside-out) [55], which starts with  
1389 tracker tracks with  $p_T > 0.5$  GeV and total momentum  $p_T > 2.5$  GeV. These tracks  
1390 are extrapolated outwards to the muon system and matched to detector segments  
1391 there, taking into account the magnetic field, expected energy losses, and multiple

1392 Coulomb scattering in the detector material. Tracker Muon reconstruction is more  
 1393 efficient than the Global Muon reconstruction at low momenta,  $p \lesssim 5$  GeV, because  
 1394 it only requires a single muon segment in the muon system, whereas Global Muon  
 1395 reconstruction typically requires segments in at least two muon stations.

1396 To further suppress fake muons from decay in flight, isolation cuts are used. A  
 1397 relative isolation variable is defined to quantify the energy flow of particles near the  
 1398 muon trajectory. A relative isolation is defined similarly for muons and electrons:

$$I^\ell \equiv \frac{\sum_{\text{charged}} p_T + \max\left(0, \sum_{\text{neutral}} p_T - \frac{1}{2} \sum_{\text{charged, PU}} p_T\right)}{p_T^\ell} \quad (5.2)$$

1399 where  $\sum_{\text{charged}} p_T$  is the scalar sum of the  $p_T$  of the charged particles originating from  
 1400 the primary vertex and located in a cone of size  $\Delta R = \sqrt{(\Delta\eta)^2 + (\Delta\phi)^2} = 0.4(0.3)$   
 1401 centered on the direction of the muon (electron). The sum  $\sum_{\text{neutral}} p_T$  is the equivalent  
 1402 for neutral particles. The sum  $\sum_{\text{charged, PU}} p_T$  is the scalar sum of the  $p_T$  of the  
 1403 charged hadrons in the cone originating from pile-up vertices. The factor 1/2 comes  
 1404 from simulation estimations, which find that the ratio of neutral to charged hadron  
 1405 production in the hadronization process of inelastic  $pp$  collisions is 1/2. Thus the  
 1406 subtracted term is intended to subtract contribution from pile-up, from the neutral  
 1407 particle contribution to the isolation sum. Finally, this is divided by the lepton  
 1408 transverse momentum,  $p_T^\ell$ .

### 1409 **5.1.3 Electrons**

1410 Electrons are the lightest lepton with a mass of 0.511 MeV. At CMS, electrons are  
 1411 reconstructed by associating a track reconstructed in the silicon tracking detector  
 1412 with a cluster of energy in the ECAL. Performance is maximized via a combination  
 1413 of a stand-alone approach and the complementary global particle-flow approach [56].

1414 In the stand-alone approach, the electron energy, which is typically spread over

several crystals of the ECAL, is clustered with the “hybrid” algorithm in the barrel and the “multi- $5 \times 5$ ” in the endcaps [56]. The hybrid algorithm collects energy in a small window in  $\eta$  and an extended window in  $\phi$ . It identifies a seed crystal, and adds arrays of  $5 \times 1$  crystals in  $\eta \times \phi$  in a range of  $N = 17$  crystals in both directions of  $\phi$ , if their energies exceed a minimum threshold, thus forming a supercluster (SC). In the endcap, crystals are not arranged in an  $\eta \times \phi$  geometry; instead clusters are build around seed crystals in clusters of  $5 \times 5$  crystals that can partly overlap. Nearby clusters are grouped into a supercluster, and energy is recovered from associated deposits in the preshower.

In the PF reconstruction [56], PF clusters are reconstructed by aggregating around a seed all contiguous crystals with energies two standard deviations above the electronic noise observed at the beginning of a data-taking run. The energy of a given crystal can be shared among two or more clusters.

The electron track reconstruction is performed in two ways [56]: the ECAL-based seeding, which begins with the SC energy and positioning, and the tracker-based seeding (part of the PF reconstruction algorithm), which uses tracks reconstructed from the general algorithm for charged particles, extrapolated towards the ECAL and matched to an SC. Kalman filter (KF) tracks with a small number of hits or that are not well-fitted, are re-fitted with a dedicated Gaussian sum Filter (GSF).

A global identification variable [56] is defined using a multivariate analysis (MVA) technique that combines information on track observables (kinematics, quality of the KF track and GSF track), the electron PF cluster observables (shape and pattern), and the association between the two (geometric and kinematic observables). For electrons seeded only through the tracker-based approach, a weak selection is applied on this MVA variable. For electrons seeded through both approaches, a logical OR is taken.

Electron isolation, i.e. the presence of energy deposits near the electron trajectory,

1442 is a separate key handle in rejecting significant background. Compared to isolated  
 1443 electrons, electrons from misidentified jets or genuine electrons within a jet resulting  
 1444 from semileptonic decays of  $b$  or  $c$  quarks tend to have significant energy deposits  
 1445 near the primary trajectory [56]. Offline analyses benefit from the PF technique  
 1446 for defining isolation, which sums the PF candidates reconstructed located within a  
 1447 specified isolation cone around the electron candidate, as in Eqn. 5.2.

#### 1448 5.1.4 Jets

1449 The vast majority of processes of interest at the LHC contains quarks or gluons in  
 1450 the final state, but these particles cannot be observed directly. In a process called  
 1451 hadronization, they fragment into spatially-grouped collections of particles called jets,  
 1452 which can be detected in the tracking and calorimeter systems. Hadronization and  
 1453 the subsequent decays of unstable hadrons can produce hundreds of nearby particles  
 1454 in the CMS detector. Jets are reconstructed by the PF algorithm (PF jets), or from  
 1455 the sum of the ECAL and HCAL energies deposited in the calorimeter towers (Calo  
 1456 jets). In PF jets, typically used in offline analyses, jets are built using the anti- $k_T$   
 1457 (AK) clustering algorithm [57]. The anti- $k_T$  algorithm iterates over particle pairs and  
 1458 finds the two that are closest in a distance measure  $d$ , and determines whether to  
 1459 combine them:

$$d_{ij} = \min(p_{T,i}^{-2}, p_{T,j}^{-2}) \frac{\Delta_{ij}^2}{R^2}, \text{ combine when } d_{ij} < p_{T,i}^{-2}; \text{ stop when } d_{ij} > p_{T,i}^{-2} \quad (5.3)$$

1460 where  $\Delta_{ij}^2 = (\eta_i - \eta_j)^2 + (\phi_i - \phi_j)^2$  and  $p_{T,i}$ ,  $\eta_i$ ,  $\phi_i$  are the transverse momentum, rapid-  
 1461 ity, and azimuthal angle of particle  $i$ . The power  $-2$  means that higher-momentum  
 1462 particles are clustered first, leading to jets that tend to be centered on the hardest  
 1463 (highest  $p_T$ ) particle.

1464 There are several methods to remove contributions of pile-up collisions from jet

1465 clustering [58]:

- 1466 • Charged hadron subtraction (CHS), which removes all charged hadron candi-  
1467 dates associated with a track that is not associated with the primary vertex.
- 1468 • PileUp Per Particle Identification (PUPPI), which weighs input particles based  
1469 on their likelihood of arising from pile-up. QCD particles tend to have a collinear  
1470 structure, compared to soft diffuse radiation coming from pile-up. The local  
1471 shape for charged pile-up, used as a proxy for all pile-up particles, is used on an  
1472 event-by-event basis to calculate a weight for each particle. PUPPI is deployed  
1473 in Run-2 and is more performant than CHS in high pile-up scenarios.

### 1474 5.1.5 B-flavored jets

1475 Jets that arise from bottom-quark hadronization (b-flavor jets) have overwhelming  
1476 background from processes involving jets from gluons (g) and light-flavor quarks (u, d,  
1477 s), and from c-quark fragmentation. The ability to identify b-flavor jets, or b-tagging,  
1478 exploits the b hadrons' relatively large masses, long lifetimes, and daughter particles  
1479 with hard momentum spectra [57].

1480 The impact parameter (IP) of a track is the 3-dimensional distance between the  
1481 track and the primary vertex (PV) at the point of closest approach. The IP is positive  
1482 if the track originates from the decay of particles travelling along the jet axis. The  
1483 resolution of the IP depends on the  $p_T$  and  $\eta$  of the track, motivating the use of the  
1484 impact parameter significance  $S_{\text{IP}}$  (ratio of the IP to its estimated uncertainty) as an  
1485 observable [57].

1486 Because of the large but finite lifetimes of the b hadrons, b hadrons tend to  
1487 travel a short distance before decaying at a secondary vertex (SV), which can be  
1488 measured and reconstructed separately from the primary vertex due to the excellent  
1489 position resolution of the pixel detector [57]. Previous b-tagging algorithms (e.g.

1490 CSV, cMVAv2, and DeepCSV) have capitalized on variables such as the presence of  
1491 a SV, the flight distance and direction (computed from the vector between the PV  
1492 and the SV), and kinematics of the system of associated secondary tracks (e.g. track  
1493 multiplicity, mass, and energy).

1494 The DeepJet (formerly known as DeepFlavour) algorithm [59] is a deep-neural-  
1495 network multi-classification algorithm, which uses 16 properties of up to 25 charged  
1496 and 6 properties of 25 neutral particle-flow jet constituents, as well as 17 properties  
1497 from up to 4 secondary vertices associate with the jet. Compared to the previous clas-  
1498 sifying algorithm DeepCSV, DeepJet has been demonstrated to have higher efficiency  
1499 with lower misidentification probability in Phase-1 data [60].

## 1500 5.2 Reconstruction of the di-tau mass

1501 The final signal extraction is done to the total di-tau ( $\tau\tau$ ) mass, which is estimated  
1502 from the visible  $\tau\tau$  mass using the FastMTT algorithm [61]. FastMTT is based on the  
1503 SVFit algorithm, originally developed for the Standard Model  $H \rightarrow \tau\tau$  analysis [62].  
1504 Both the SVFit algorithms, and the FastMTT algorithm, are described below, to give  
1505 a complete picture of how the algorithms attempt to reconstruct the true invariant  
1506 mass of a Higgs or  $Z$  boson decay.

1507 To specify a hadronic  $\tau$  decay, six parameters are needed [62]: the polar and  
1508 azimuthal angles of the visible decay product system in the  $\tau$  rest frame, the three  
1509 boost parameters from the  $\tau$  rest frame to the laboratory frame, and the invariant  
1510 mass  $m_{\text{vis}}$  of the visible decay products. For a leptonic  $\tau$  decay, two neutrinos are  
1511 produced, and a seventh parameter, the invariant mass of the two-neutrino system, is  
1512 necessary. The unknown parameters are constrained by four observables that are the  
1513 components of the four-momentum of the system formed by the visible decay products  
1514 of the  $\tau$  lepton, measured in the laboratory frame. The remaining unconstrained

1515 parameters for hadronic and leptonic  $\tau$  decays are thus:

- 1516 • The fraction of the  $\tau$  energy in the laboratory frame carried by the visible decay  
1517 products,
- 1518 •  $\phi$ , the azimuthal angle of the  $\tau$  direction in the laboratory frame,
- 1519 •  $m_{\nu\nu}$ , the invariant mass of the two-neutrino system in leptonic  $\tau$  decays (for  
1520 hadronic  $\tau$  decays,  $m_{\nu\nu}$  is set to 0).

1521  $E_x^{\text{miss}}$  and  $E_y^{\text{miss}}$ , the  $x$  and  $y$  components of the missing transverse energy  $E_T^{\text{miss}}$   
1522 provide two further constraints.

### 1523 5.2.1 Original SVFit ‘‘standalone’’: maximum likelihood

1524 In one of the original versions of SVFit, called ‘‘standalone’’ SVFit [62], a maximum  
1525 likelihood fit method is used to reconstruct the mass  $m_{\tau\tau}$  by combining the measured  
1526 observables  $E_x^{\text{miss}}$  and  $E_y^{\text{miss}}$  with a likelihood model that includes terms for the  $\tau$   
1527 decay kinematics and the  $E_T^{\text{miss}}$  resolution [62]. The likelihood function  $f(\vec{z}, \vec{y}, \vec{a}_1 \vec{a}_2)$   
1528 of the parameters  $\vec{z} = (E_x^{\text{miss}}, E_y^{\text{miss}})$  in an event is constructed, where the remaining  
1529 parameters are the kinematics of the two  $\tau$  decays, denoted  $\vec{a}_1 = (x_1, \phi_1, m_{\nu\nu,1})$  and  
1530  $\vec{a}_2 = (x_2, \phi_2, m_{\nu\nu,2})$ , and the four-momenta of the visible decay products with the  
1531 measured values  $\vec{y} = (p_1^{\text{vis}}, p_2^{\text{vis}})$ .

1532 The likelihood  $f$  is the product of three likelihood functions. The first two likelihood  
1533 functions model the decay parameters  $\vec{a}_1$  and  $\vec{a}_2$  of the two  $\tau$  leptons. For leptonic  
1534 decays, the likelihood function is modeled using matrix elements for  $\tau$  decays,  
1535 and integrated over the allowed phase space  $0 \leq x \leq 1$  and  $0 \leq m_{\nu\nu} \leq m_\tau \sqrt{1-x}$ . For  
1536 hadronic  $\tau$  decays, a model based on the two-body phase space is used and integrated  
1537 over  $m_{\text{vis}}^2/m_{\tau\tau}^2 \leq x \leq 1$ . The third likelihood function quantifies the compatibility of  
1538 a  $\tau$  decay hypothesis with the reconstructed  $\vec{E}_T^{\text{miss}}$  in an event, assuming the neutrinos  
1539 are the only source of missing transverse energy. The expected  $\vec{E}_T^{\text{miss}}$  resolution

1540 is represented by a covariant matrix, estimated on an event-by-event basis using a  
1541 significance algorithm [63].

### 1542 5.2.2 “Classic SVFit” with matrix element

1543 Classic SVFit is an improved algorithm of the original “standalone” SVFit using the  
1544 formalism of the matrix element (ME) method [61]. In the ME method, an estimate  
1545 for the unknown model parameter  $\Theta$  (here, the mass  $m_{\tau\tau}$ ) is obtained by maximizing  
1546 the probability density  $\mathcal{P}$ . The key ingredients of the probability density are the  
1547 squared modulus of the matrix element  $|\mathcal{M}(\mathbf{p}, \Theta)|^2$  and the transfer function  $W(\mathbf{y}|\mathbf{p})$   
1548 (probability density to observe the measured observables  $\mathbf{y}$  given the phase space  
1549 point  $\mathbf{p}$ ). The best estimate  $m_{\tau\tau}$  is obtained by computing the probability density  $\mathcal{P}$   
1550 for a range of mass hypotheses and finding the value of  $m_{\tau\tau}$  that maximizes  $\mathcal{P}$ .

1551 Distributions illustrating the performance of the classic matrix element SVFit  
1552 algorithm are shown in Fig. 5.1 from [61], showing the di-tau mass after and before  
1553 application of SVFit to recover energy lost to neutrinos. The SVFit algorithm is  
1554 found to improve the sensitivity of the Standard Model  $H \rightarrow \tau\tau$  analysis performed  
1555 by CMS by about 30%, compared to performing the same analysis using only the  
1556 visible mass  $m_{\text{vis}}$ .

### 1557 5.2.3 FastMTT: optimized SVFit

1558 FastMTT [64] is a further simplification to the matrix element method of Classic  
1559 SVFit which has comparable performance but is about 100 times faster. FastMTT  
1560 drops the matrix element component of the computation without significant impact  
1561 on the final mass resolution, and simplifies the computation of the transfer functions.  
1562 The opening angle of the  $\tau$  decay products with respect to the initial  $\tau$  momenta ap-  
1563 proaches 0 for  $\tau$  with high  $\gamma = E_\tau/m_\tau$ , with typical  $\tau$  decays from the Z boson decays  
1564 already satisfying this condition. In this collinear approximation, the dimensionality

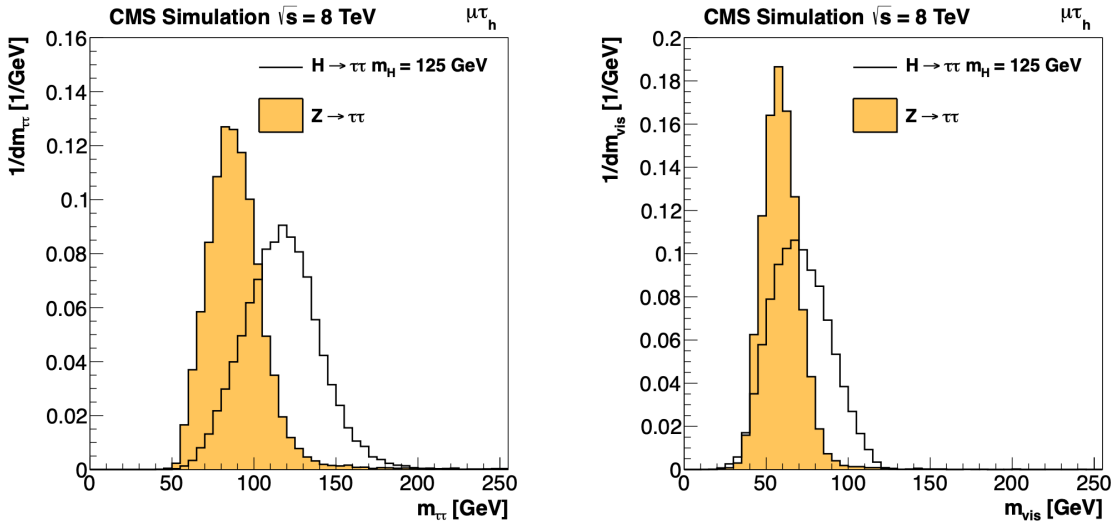


Figure 5.1: Distributions from [61], of  $m_{\tau\tau}$  after reconstruction with the original SVFit algorithm (*left*), and before SVFit with only the visible tau decay products (*right*), for  $H \rightarrow \tau\tau$  signal events of mass  $m_H = 125$  GeV (*black line*) and the  $Z/\gamma^* \rightarrow \tau\tau$  background (*orange, solid*), in the decay channel  $\tau\tau \rightarrow \mu\tau_h$ .

1565 of the transfer function can be reduced in the computation of FastMTT, while still  
1566 yielding similar results to Classic SVFit [64].

### 1567 5.3 Corrections applied to simulation

1568 Corrections are applied to simulated samples to account for known effects in the event  
1569 modeling and reconstruction and data-taking, and are intended to bring simulations  
1570 in closer agreement with data. Corrections fall into two broad categories: *energy*  
1571 *scale corrections* applied to physics objects, and *event-level corrections*. Energy scale  
1572 corrections are multiplicative factors applied to the energy and transverse momentum  
1573  $p_T$  of simulated objects (e.g. leptons or jets), and bring the average reconstructed en-  
1574 ergies of simulated particles into better agreement with those of objects reconstructed  
1575 from data. Event-level corrections are applied as a per-event multiplicative weight,  
1576 and account for effects such as mis-modeling in simulations of the underlying physics  
1577 process, or changing detector operating conditions during data-taking. Event-level

1578 corrections change the shapes of the distributions of all the physical observables.

1579 Uncertainties in scale factors and corrections are also sources of systematic errors  
1580 in the analysis, detailed in Chapter 8. Systematic uncertainties in the tau, muon, and  
1581 electron energy scales can shift the  $p_T$  of the leptons up or down, which can change  
1582 whether events pass or fail the offline  $p_T$  thresholds for the trigger paths described in  
1583 the previous section, i.e. change the number of events in the signal region.

### 1584 5.3.1 Tau energy scale

1585 An energy scale is applied to the transverse momentum  $p_T$  and mass of the hadronic  
1586 tau  $\tau_h$  in the  $\mu\tau_h$  and  $e\tau_h$  channels, to correct for a deviation of the average recon-  
1587 structed  $\tau_h$  energy from the generator-level energy of the visible  $\tau_h$  decay products.  
1588 These correction factors are derived centrally [53], by fitting to events in  $e\tau_h$  and  $\mu\tau_h$   
1589 final states in  $Z/\gamma^*$  events separately for the  $h^\pm$ ,  $h^\pm\pi^0$ , and  $h^\pm h^\mp h^\pm$  decays. The  
1590 values used are shown in Table 5.1.

1591 When applying the energy scale to the  $\tau_h$ , the 4-momentum of the missing trans-  
1592 verse energy (MET) is adjusted such that the total 4-momenta of the  $\tau_h$  and the MET  
1593 remains unchanged [65].

Tau energy scale factor				
Decay mode	2018	2017	2016 pre-VFP	2016 post-VFP
0	$0.991 \pm 0.008$	$0.986 \pm 0.009$	$0.987 \pm 0.01$	$0.993 \pm 0.009$
1	$1.004 \pm 0.006$	$0.999 \pm 0.006$	$0.998 \pm 0.006$	$0.991 \pm 0.007$
10	$0.998 \pm 0.007$	$0.999 \pm 0.007$	$0.984 \pm 0.008$	$1.001 \pm 0.007$
11	$1.004 \pm 0.009$	$0.996 \pm 0.01$	$0.999 \pm 0.011$	$0.997 \pm 0.016$

Table 5.1: Energy scales applied to genuine hadronic tau decays  $\tau_h$  by data-taking year/era and decay mode, along with systematic errors.

1594 **5.3.2 Muon energy scale**

1595 An energy scale is applied to the  $p_T$  and mass of genuine muons from  $\tau$  decays in the  
1596  $e\mu$  and  $\mu\tau_h$  channels [66]. The applied values are the same for MC and embedded  
1597 samples and are shown in Table 5.2. Following the SM  $H \rightarrow \tau\tau$  analysis, Rochester  
1598 corrections are not applied, and instead prescriptions from [67] are followed.

Muon energy scale factor	
Eta range	Value for all years
$ \eta  \in [0.0, 1.2)$	$1.0 \pm 0.004$
$ \eta  \in [1.2, 2.1)$	$1.0 \pm 0.009$
$ \eta  \in [2.1, 2.4)$	$1.0 \pm 0.027$

Table 5.2: Energy scales and systematic errors applied to genuine muons. The values are the same for MC and embedded for all years [68] [67].

1599 **5.3.3 Electron energy scale**

1600 Corrections to the electron energy scale are applied to genuine  $e$  from  $\tau$  decays, and  
1601 are binned in two dimensions by electron  $p_T$  and  $\eta$  for barrel vs. endcap [69]. The  
1602 scale factors are binned in  $p_T$  and  $\eta$  for MC samples: e.g. values for 2018 are shown  
1603 in Fig. 5.2 from [70]. For embedded samples the electron energy scale is taken as  
1604 only binned in  $\eta$  (Table 5.3).

Electron energy scale factor for embedded samples			
Eta range	2018	2017	2016
$ \eta  \in [0.0, 1.479)$	$0.973 \pm 0.005$	$0.986 \pm 0.009$	$0.9976 \pm 0.0050$
$ \eta  \in [1.479, 2.4)$	$0.980 \pm 0.0125$	$0.887 \pm 0.0125$	$0.993 \pm 0.0125$

Table 5.3: Energy scales and systematic errors applied to electrons in embedded samples, binned in the electron  $\eta$ , by data-taking year [71] [72] [73].

1605 **5.3.4  $\tau_h$  identification efficiency**

1606 The  $\tau_h$  identification efficiency can differ in data and MC [65]. Recommended correc-  
1607 tions are provided by the Tau POG, and we use the medium DeepTau vs. jet working

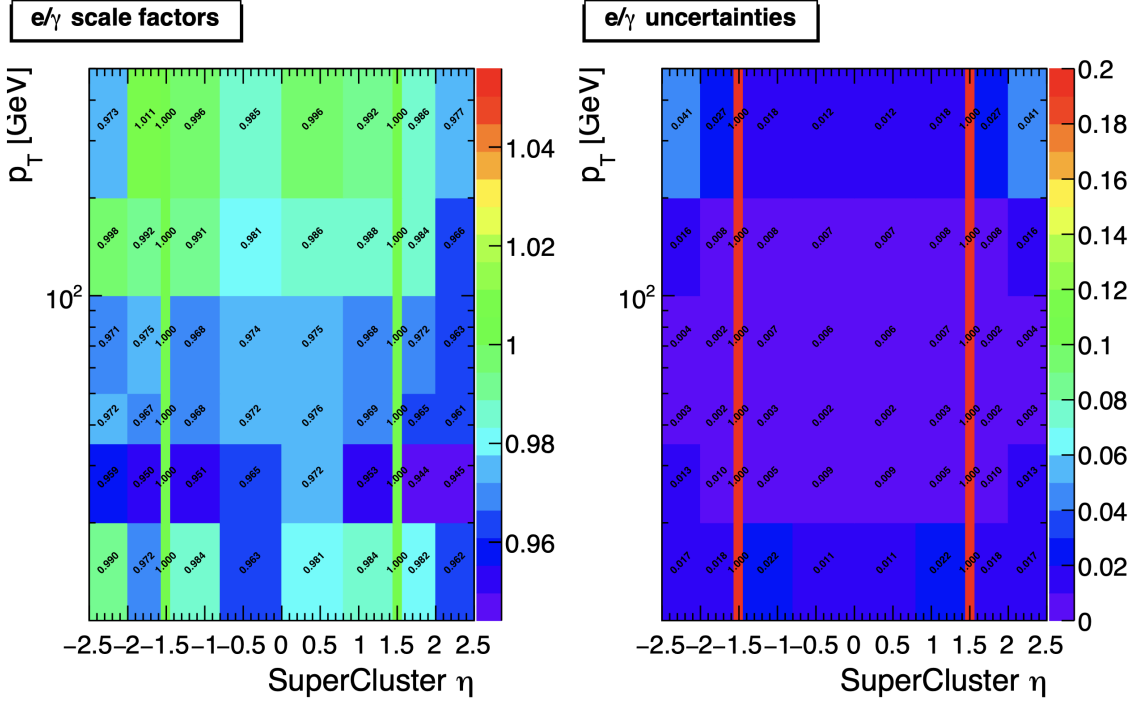


Figure 5.2: Electron/photon energy scale factors (*left*) and corresponding uncertainties (*right*) binned in the electron  $\eta$  and  $p_T$ , for the data-taking year 2018 [70].

1608 point values. The identification efficiency is measured in  $Z \rightarrow \tau\tau$  events in the  $\mu\tau_h$   
 1609 final state, and is binned in  $p_T$  due to clear  $p_T$  dependence of the DeepTau ID.

Tau ID efficiency for DeepTau Medium vs. jet WP in 2018						
$p_T$ (GeV)	< 20	(20, 25]	(25, 30]	(30, 35]	(35, 40]	(40, 500]
Central value	0	0.945	0.946	0.916	0.921	1.005
Up value	0	1.001	0.981	0.946	0.950	1.035
Down value	0	0.888	0.981	0.883	0.893	0.953

Table 5.4: Tau ID efficiency for the DeepTau vs. jet medium working point, with central, up, and down values for 2018, binned in the tau  $p_T$  [65].

### 1610 5.3.5 Trigger efficiencies

1611 Scale factors are applied to correct for differences in trigger efficiencies between MC  
 1612 and embedded vs. data, with values taken from tools provided by the Standard Model  
 1613  $H \rightarrow \tau\tau$  working group which uses the same trigger paths [68]. In the following

1614 sections we review relevant trigger efficiencies in data, which form the basis of the  
1615 trigger efficiency corrections applied to MC and embedded.

1616 **5.3.6 Tau trigger efficiencies**

1617 The efficiencies in data of the single- $\tau_h$  leg in  $\mu\tau_h$ ,  $e\tau_h$ , and di- $\tau_h$  triggers is computed  
1618 centrally per using a Tag and Probe (TnP) method [74] which is outlined here. In  
1619 this method,  $Z \rightarrow \tau\tau \rightarrow \mu\tau_h$  are selected in data and a Drell-Yan simulated sample  
1620 ( $Z \rightarrow \ell\ell, \ell = e, \mu, \tau_h$ ) with high purity. Cuts are applied to reject events not in this  
1621 final state, e.g. suppressing  $Z \rightarrow \mu\mu$  by vetoing events with a single loose ID muon.  
1622 An isolated muon candidate (the tag) with online  $p_T > 27$  GeV and  $|\eta| < 2.1$  is  
1623 identified and matched to an offline  $\mu$ . An offline  $\tau_h$  candidate (the probe) is selected,  
1624 which is separated from the tag  $\mu$ , and has  $p_T > 20$  GeV and  $|\eta| < 2.1$ . The probe  
1625  $\tau_h$  must pass anti-muon and anti-electron discriminators to avoid fakes from muons  
1626 and electrons, and must pass the medium MVA tau isolation to suppress fakes from  
1627 QCD jets. The trigger efficiency in the TnP method is calculated as

$$\text{Efficiency} = \frac{\text{Number of events passing the TnP selection with fires the HLT path}}{\text{Number of events passing the TnP selection}} \quad (5.4)$$

1628 The efficiencies for the hadronic tau legs in the relevant channels of this analyses  
1629 ( $\mu\tau_h$  and  $e\tau_h$ ) as a function of the offline tau  $p_T$  and  $\eta$ , are shown for data taken in  
1630 2016, 2017, and 2018 in Figures 5.3a and 5.3b [74] [75]. In both figures, the different  
1631 HLT thresholds and differences in the L1 seed result in higher efficiencies in 2016 and  
1632 differences in shapes of the 2016 efficiencies compared to 2017 and 2018. The low  
1633 pile-up in 2016 also leads to higher efficiencies in that year.

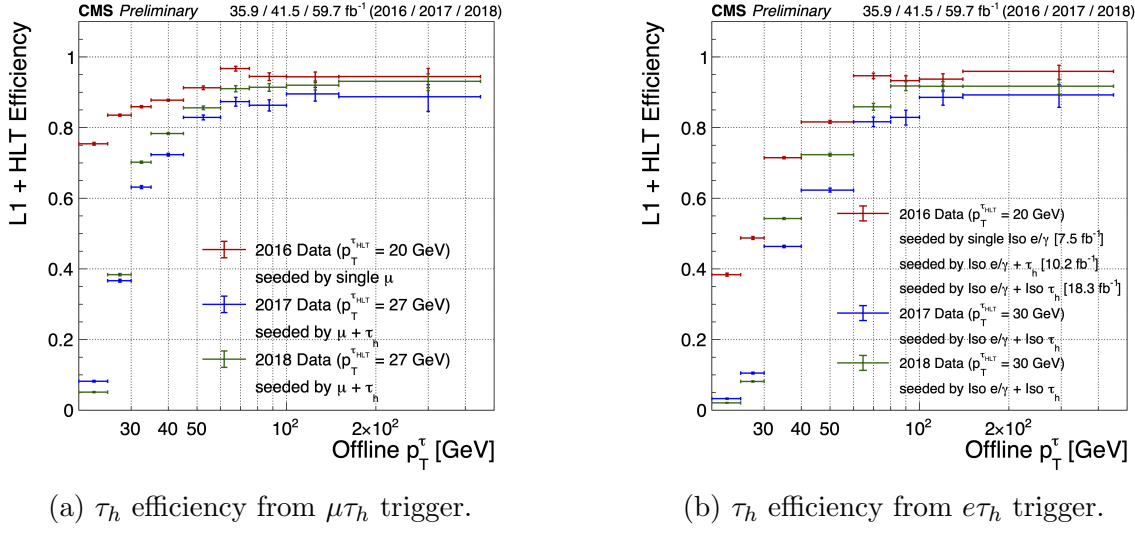
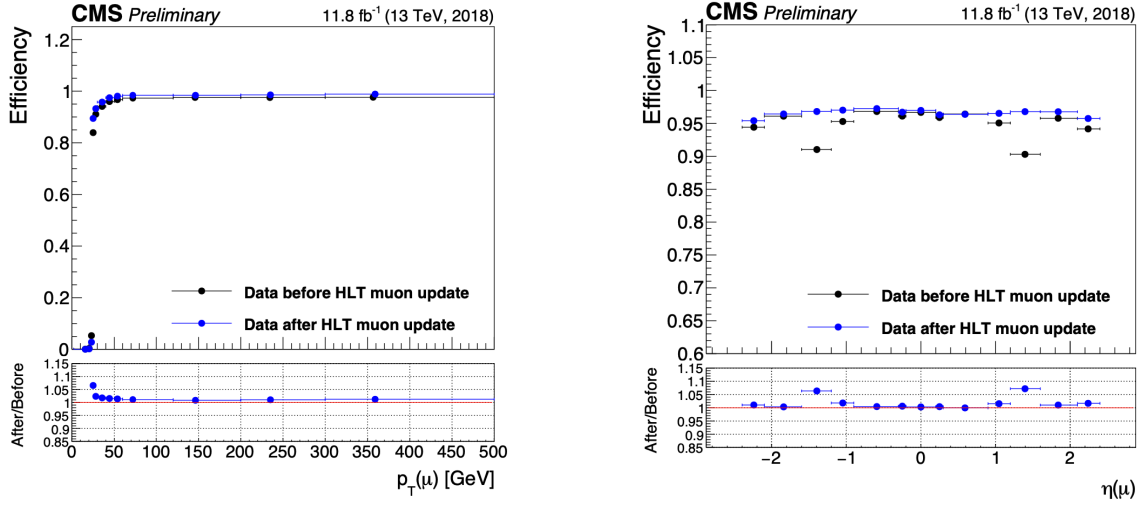


Figure 5.3: Hadronic tau leg efficiency of the cross-triggers for  $\mu\tau_h$  (left) and  $e\tau_h$  (right) triggers as a function of offline tau  $p_T$  for the years 2016 (red), 2017 (blue) and 2018 (green), from [75]. HLT  $p_T$  thresholds and L1 seeds are indicated in the legends.

### 5.3.7 Single muon trigger efficiencies

The efficiencies for the single isolated muon trigger with  $p_T > 24 \text{ GeV}$  used in this analysis, is shown for the data-taking year 2018 in Fig. 5.4a as a function of the muon  $p_T$  and as a function of the muon  $|\eta|$  in Fig. 5.4b from [76]. The data is split with respect to a HLT muon reconstruction update that was deployed on 15/05/2018. A small asymmetry in efficiencies between negative and positive  $\eta$  in Fig. 5.4b is due to disabled muon chambers (CSCs). The efficiencies shown are estimated using a Tag and Probe method using  $Z \rightarrow \mu\mu$  events, with the tag being an offline muon with  $p_T > 29 \text{ GeV}$  and  $|\eta| < 2.4$  passing a tight ID criteria, and the probe is an online (L1) trigger object with  $\Delta R < 0.3$  and passing tight ID and Particle Flow based isolation requirements with  $p_T > 26 \text{ GeV}$ .



(a) Muon efficiency vs  $p_T$  for SingleMuon.

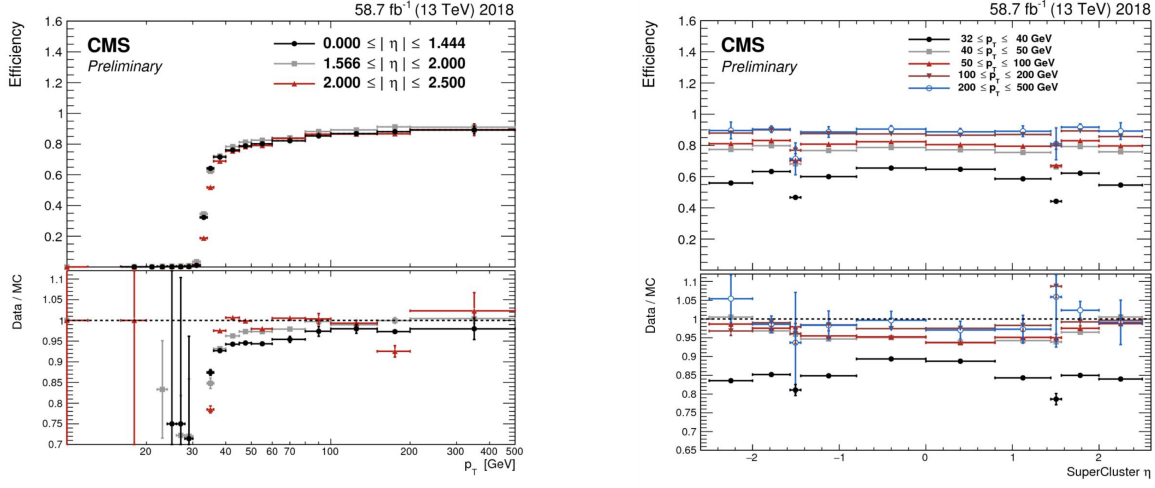
(b) Muon efficiency vs  $|\eta|$  for SingleMuon.

Figure 5.4: Trigger efficiencies in data (*top panels*) and ratio of efficiencies after/before a HLT muon reconstruction update (*bottom panels*) for the muon in the isolated single muon trigger with threshold  $p_T > 24$  GeV in the data-taking year 2018, as functions of the muon  $p_T$  (*left*) and muon  $|\eta|$  (*right*). Only statistical errors are shown [76].

### 1645 5.3.8 Single electron trigger efficiencies

1646 The efficiencies in data, and the ratio between data and MC, of the single electron  
 1647 HLT trigger with  $p_T$  threshold 32 GeV used in this analysis are shown for 2018,  
 1648 as a function of the electron  $p_T$  in Fig. 5.5a and of the electron  $|\eta|$  in Fig. 5.5b,  
 1649 from [77]. In the Tag and Probe method used for the 2018 dataset, the tag is an  
 1650 offline reconstructed electron with  $|\eta| \leq 2.1$  and not in the barrel and endcap overlap  
 1651 region, with  $p_T > 35$  GeV with tight isolation and shower shape requirements, firing  
 1652 the tag trigger. The probe is an offline reconstructed electron with  $|\eta| \leq 2.5$  with  
 1653  $E_T^{\text{ECAL}} > 5$  GeV with no extra identification criteria [77].

1654 The disagreement between data and MC, particularly at low transverse momentum,  
 1655 is in part due to detector effects that are difficult to simulate, such as crys-  
 1656 tal transparency losses in the ECAL and the evolution of dead regions in the pixel  
 1657 tracker [77].



(a) Electron efficiency vs  $p_T$  for single electron.

(b) Electron efficiency vs  $|\eta|$  for single electron.

Figure 5.5: Trigger efficiencies in data, and the data/MC ratio for the electron in the single electron trigger with threshold  $p_T > 32$  GeV in the data-taking year 2018, as functions of the electron  $p_T$  (*left*) and electron  $|\eta|$  (*right*) [77]. In the plot vs.  $p_T$ , the region  $1.442 \leq |\eta| \leq 1.566$  is not included as it corresponds to the transition between barrel and endcap parts of the ECAL.

### 1658 5.3.9 $e\mu$ cross-trigger efficiencies

1659 The efficiencies of the electron and muons for the cross-trigger with leading muon  
 1660 used in the  $e\mu$  channel are shown for data in 2016, 2017, and 2018 in Figures 5.6a and  
 1661 5.6b [78]. These efficiencies were measured centrally using a Tag and Probe in events  
 1662 with  $Z$  to dileptons with the same flavor and opposite charge, where the tags are an  
 1663 isolated muon or electron, and the probe (offline) candidate is required to satisfy the  
 1664 same lepton selection as that of the tag candidate, be matched within  $\Delta R < 0.1$  with  
 1665 a corresponding online trigger object, and also to pass the cross-trigger. The trigger  
 1666 efficiency is then:

$$\text{Efficiency} = \frac{\text{Events passing lepton pair selections and probe passing trigger}}{\text{Events passing lepton pair selections}} \quad (5.5)$$

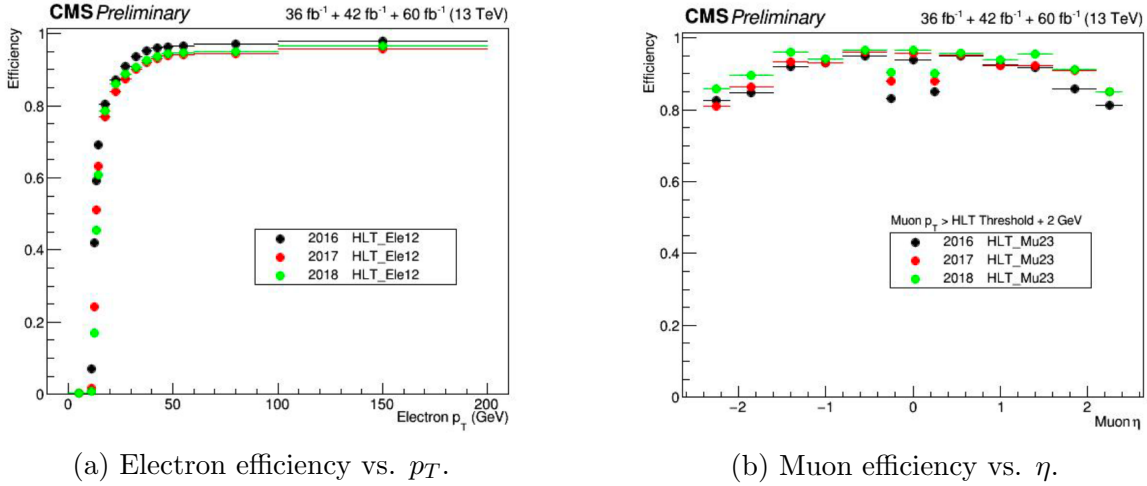


Figure 5.6: Efficiencies of the electron leg vs.  $p_T$  (*left*) and the muon leg vs.  $\eta$  (*right*), for the HLT path with online thresholds of 12 GeV for the electron and 23 GeV for the muon, for the data-taking years 2016 (*black*), 2017 (*red*), and 2018 (*green*) [78].

### 1667 5.3.10 Electrons and muons faking $\tau_h$ : energy scales

1668 Energy scales for electrons misidentified as hadronic tau decays ( $e$  faking  $\tau_h$ ) are  
 1669 provided by the Tau POG, and were measured in the  $e\tau_h$  channel with the visible  
 1670 invariant mass of the electron and hadronic tau system [68]. This energy scale is  
 1671 applied for  $\tau_h$  with  $p_T > 20$  GeV regardless of which DeepTau vs. electron working  
 1672 point was used. Values for 2018 are shown in Table 5.5.

Electrons faking $\tau_h$ energy scale factor in 2018	
Reconstructed decay mode of the fake $\tau_h$	Central value and (up, down) shifts
0	1.01362 (+0.00474, -0.00904)
1	1.01945 (+0.01598, -0.01226)
10	0.96903 (+0.0125, -0.03404)
11	0.985 (+0.04309, -0.05499)

Table 5.5: Energy scales and up/down systematic uncertainties applied to electrons misidentified as hadronic taus for 2018, binned in decay mode of the fake  $\tau_h$  [68].

1673 No nominal energy scale is applied for muons mis-reconstructed as  $\tau_h$ , and the  
 1674 uncertainty is treated as  $\pm 1\%$  and uncorrelated in the reconstructed decay mode [68].

1675    **5.3.11 Electrons and muons faking  $\tau_h$ : misidentification effi-**  
 1676    **ciencies**

1677    Corrections on identification efficiencies are applied to genuine electrons and muons  
 1678    misidentified as  $\tau$  to account for differences in data and MC.

1679    The specific values depend on the vs. electron and vs. muon discriminator working  
 1680    points used. For misidentified  $\mu \rightarrow \tau_h$ , the scale factors are split into different  $|\eta|$   
 1681    regions, determined by the CMS muon and tracker detector geometries, as shown in  
 1682    Table 5.6 for 2018 [65].

Tau ID efficiency for DeepTau vs. muon WPs in 2018		
$ \eta $	Tight working point	VLoose working point
(0.0, 0.2)	$0.767 \pm 0.127$	$0.954 \pm 0.069$
(0.2, 0.6)	$1.255 \pm 0.258$	$1.009 \pm 0.098$
(0.6, 1.0)	$0.902 \pm 0.203$	$1.029 \pm 0.075$
(1.0, 1.45)	$0.833 \pm 0.415$	$0.928 \pm 0.145$
(1.45, 2.0)	$4.436 \pm 0.814$	$5.000 \pm 0.377$
(2.0, 2.53)	$1.000 \pm 0.000$	$1.000 \pm 0.000$

Table 5.6: Tau mis-identification efficiency for the DeepTau Tight and Very Loose (VLoose) working points vs. muons in 2018, binned in the muon  $|\eta|$  [65].

1683    For misidentified  $e \rightarrow \tau_h$ , the scale factors are split into barrel and endcap regions,  
 1684    dictated by the ECAL detector geometry, as shown in Table 5.7 for 2018.

Tau ID efficiency for DeepTau vs. electron WPs in 2018		
$ \eta $	Tight working point	VLoose working point
(0.0, 0.73)	$1.47 \pm 0.27$	$0.95 \pm 0.07$
(0.73, 1.509)	$1.509 \pm 0.0$	$1.00 \pm 0.0$
(1.509, 1.929)	$1.929 \pm 0.2$	$0.86 \pm 0.1$
(1.929, 2.683)	$2.683 \pm 0.9$	$2.68 \pm 0.0$

Table 5.7: Tau mis-identification efficiency for the DeepTau Tight and Very Loose (VLoose) working points vs. electrons in 2018, binned in the electron  $|\eta|$  [65].

### 1685 5.3.12 Electron ID and tracking efficiency

1686 Scale factors are applied to MC to correct for differences between MC and data in  
 1687 the performance of electron identification (ID) and tracking.

1688 Electron and photon identification, as discussed earlier, use variables with good  
 1689 signal vs. background discrimination power such as lateral shower shape and ratio  
 1690 of energy deposited in the HCAL to energy deposited in the ECAL at the position  
 1691 of the electron. The cut-based electron identification efficiencies in data and ratio of  
 1692 efficiencies in data to MC are shown in Fig. 5.7a for the multivariate analysis (MVA)  
 1693 identification working point.

1694 The tracking efficiencies in data and the data/MC ratio are shown in Fig. 5.7b  
 1695 for the Gaussian-sum filter (GSF) tracking [79].

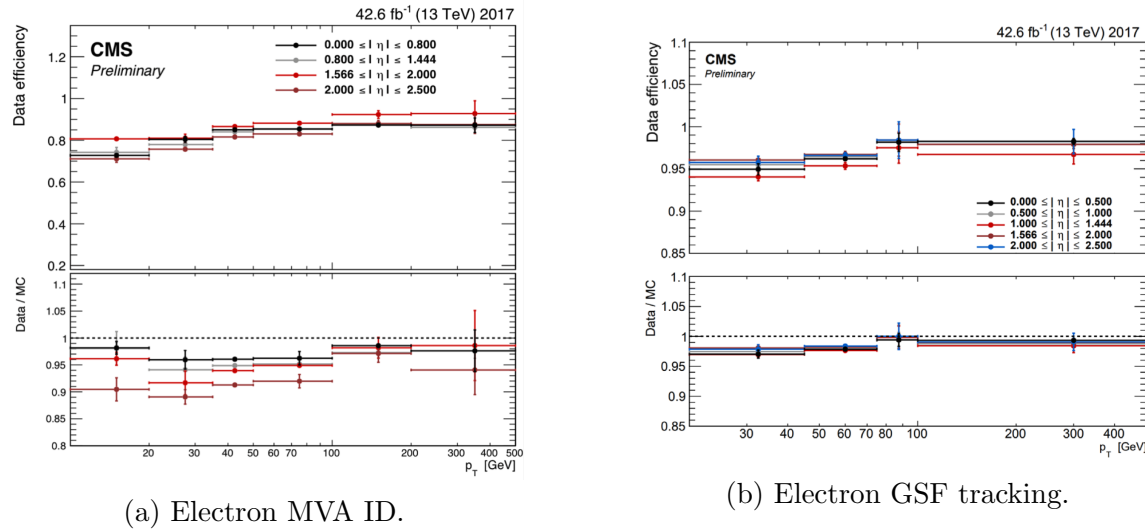


Figure 5.7: Efficiencies in data (*top panels*) and the ratio of efficiencies in data/MC (*bottom panels*), for the electron multivariate analysis (MVA) identification (*left*) and for the Gaussian-sum filter (GSF) tracking (*right*) [79]. Error bars represent statistical and systematic uncertainties.

### 1696 5.3.13 Muon ID, isolation, and tracking efficiencies

1697 Scale factors are applied to MC to correct for differences between MC and data in  
 1698 the performance of muon identification, isolation, and tracking, as detailed below.

1699        The efficiencies for muon identification measured in 2015 data and MC simulation  
 1700    are shown in Figures 5.8a and 5.8b for the loose ID and tight ID respectively [80]. The  
 1701    loose ID is chosen such that efficiency exceeds 99% over the full  $\eta$  range, and the data  
 1702    and simulation agree to within 1%. The tight ID is chosen such that efficiency varies  
 1703    between 95% and 99% as a function of  $\eta$ , and the data and simulation agree to within  
 1704    1-3%. The muon identification working point used in this analysis is the medium ID,  
 1705    which has an efficiency of 98% for all  $\eta$  and an agreement within 1-2% [80].

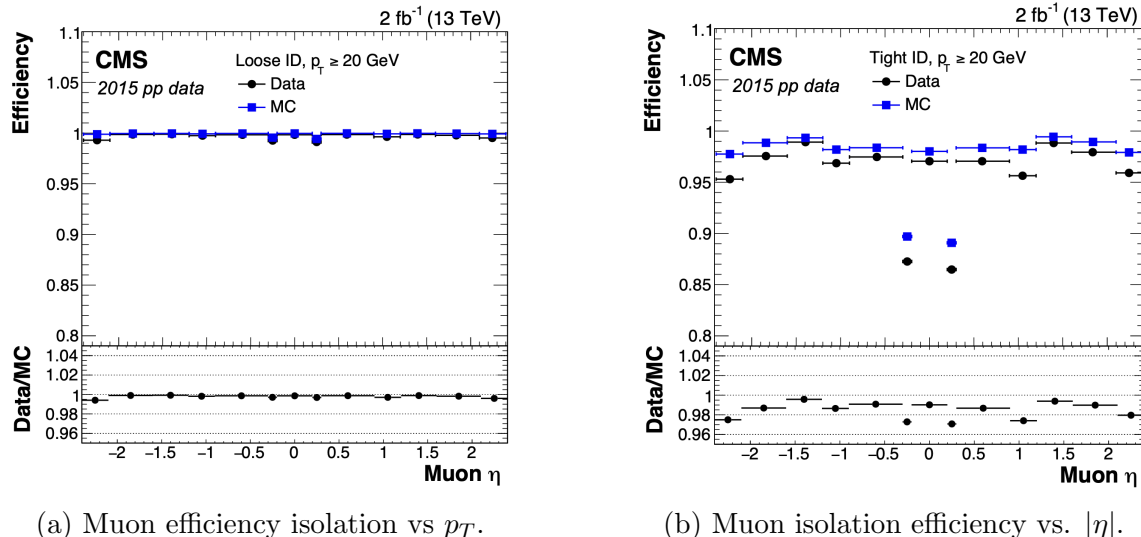
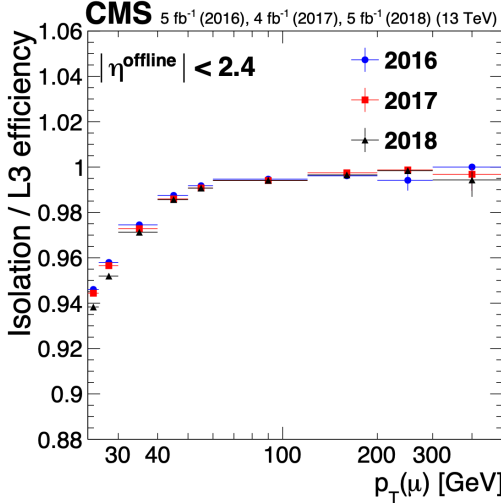


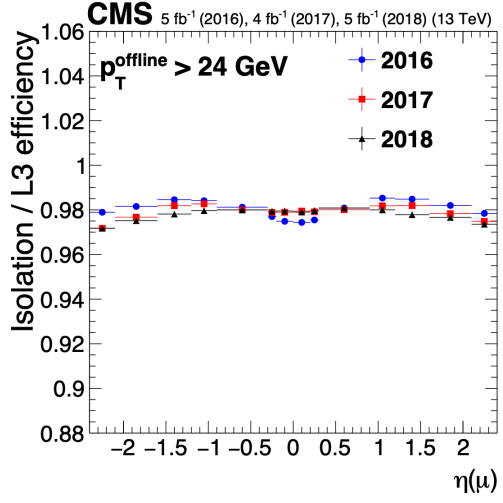
Figure 5.8: Muon identification efficiencies in 2015 data and MC as a function of the muon  $p_T$  for the loose ID (*left*) and tight ID (*right*) working points [80].

1706        The efficiencies in data for the muon isolation, as measured in Level-3 muons  
 1707    (muons in one of the final stages of reconstruction in the HLT), as a function of the  
 1708    muon  $p_T$  and  $|\eta|$  are shown in Figures 5.9a and 5.9b [80]. The HLT muon reconstruc-  
 1709    tion consists of two steps: Level-2 (L2), where the muon is reconstructed in the muon  
 1710    subdetectors only, and Level-3 (L3) which is a global fit of tracker and muon hits (i.e.  
 1711    the global muon reconstruction as described in Section 5.1.2) [81].

1712        The muon tracking efficiencies as a function of  $|\eta|$  for standalone muons (i.e. tracks  
 1713    from only the muon system, i.e. DT, CSC, and RPC, as discussed in Section 5.1.2),  
 1714    is shown for data and simulated Drell-Yan samples in Fig. 5.10 [82].



(a) Muon efficiency isolation vs  $p_T$ .



(b) Muon isolation efficiency vs.  $|\eta|$ .

Figure 5.9: Muon isolation efficiencies in Run-2 data with respect to Level-3 muons (one of the final stages of HLT muon reconstruction) as a function of the muon  $p_T$  (*left*) and  $|\eta|$  (*right*) [80].

### 1715 5.3.14 Recoil corrections

1716 In proton-proton collisions, W and Z bosons are predominantly produced through  
1717 quark-antiquark annihilation. Higher-order processes can induce radiated quarks or  
1718 gluons that recoil against the boson, imparting a non-zero transverse momentum to  
1719 the boson [83]. Recoil corrections accounting for this effect are applied to samples  
1720 with W+jets, Z+jets, and Higgs bosons [68]. The corrections are performed on the  
1721 vectorial difference between the measured missing transverse momentum and the total  
1722 transverse momentum of neutrinos originating from the decay of the W, Z, or Higgs  
1723 boson. This vector is projected onto the axes parallel and orthogonal to the boson  
1724  $p_T$ . This vector, and the resulting correction to use, is measured in  $Z \rightarrow \mu\mu$  events,  
1725 since these events have leptonic recoil that do not contain neutrinos, allowing the  
1726 4-vector of the Z boson to be measured precisely. The corrections are binned in  
1727 generator-level  $p_T$  of the parent boson and also the number of jets in the event.

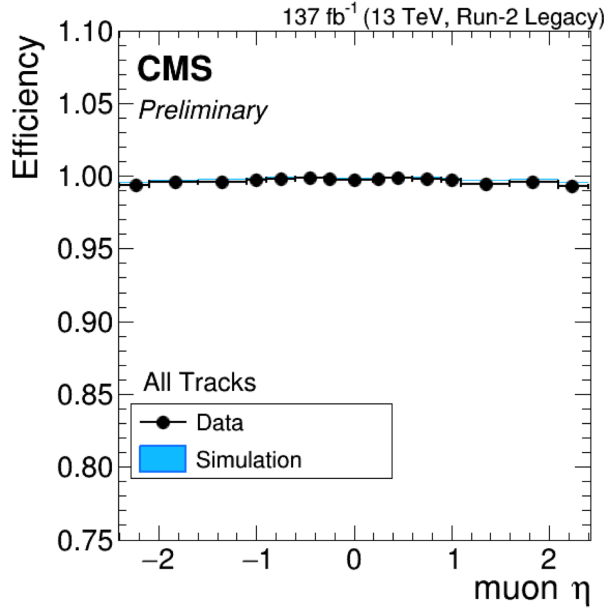


Figure 5.10: Muon tracking efficiencies as a function of  $|\eta|$  for standalone muons in Run-2 data (*black*) and Drell-Yan MC simulation (*blue*) [82]. All Tracks refers to tracks which exploit the presence of muon candidates in the muon system to seed the track reconstruction in the inner tracker, in contrast to tracks that use tracker-only hits for seeding. Uncertainties shown are statistical.

### 5.3.15 Drell-Yan corrections

The Z boson transverse momentum distribution disagrees between leading-order (LO) simulations and data in a  $Z \rightarrow \mu\mu$  control region with at least one b-tag jet [84]. Per-event weights derived by the 2016 data-only version of this analysis [84] are applied to  $Z \rightarrow \tau\tau/\ell\ell$  events, as a function of the generator-level Z boson  $p_T$  to provide better matching of MC to data.

### 5.3.16 Pile-up reweighting

Reweighting is performed to rescale MC events to account for differences between MC and data, in the distribution of the pile-up (number of additional proton-proton interactions per bunch crossing). A tool for calculating the pile-up reweighting for the MC samples used is provided centrally by the Luminosity POG [85].

<sub>1739</sub> **5.3.17 Pre-firing corrections**

<sub>1740</sub> In 2016 and 2017 data-taking, a gradual timing shift of ECAL was not properly  
<sub>1741</sub> propagated to L1 trigger primitives (TPs), resulting in a large fraction of high  $\eta$   
<sub>1742</sub> TPs being incorrectly associated with the previous bunch crossing. L1 trigger rules  
<sub>1743</sub> prevent two consecutive bunch crossings from firing, causing events to be rejected if  
<sub>1744</sub> significant ECAL energy was deposited in  $2.0 < |\eta| < 3.0$ . To account for this issue,  
<sub>1745</sub> MC simulations for 2016 and 2017 are corrected using an event-dependent weight.  
<sub>1746</sub> Embedded samples are not corrected [50].

<sub>1747</sub> **5.3.18 Top  $p_T$  spectrum reweighing**

<sub>1748</sub> In Run-1 and Run-2 it was observed that the  $p_T$  spectra of top quarks in  $t\bar{t}$  data  
<sub>1749</sub> was significantly softer than those predicted by MC simulations [86]. Possible sources  
<sub>1750</sub> of this discrepancy are higher order QCD and/or electroweak corrections, and non-  
<sub>1751</sub> resonant production of  $t\bar{t}$ -like final states. To account for this, corrections derived  
<sub>1752</sub> from Run-2 data by the Top Physics Analysis Group (PAG) are applied to the  $p_T$   
<sub>1753</sub> of the top and anti-top quarks in MC simulations, computed as a function of their  
<sub>1754</sub> generator-level  $p_T$  [86].

<sub>1755</sub> **5.3.19 B-tagging efficiency**

<sub>1756</sub> In order to predict correct b-tagging discriminant distributions and event yields in  
<sub>1757</sub> data, the weight of selected MC events is reweighed according to recommendations by  
<sub>1758</sub> the BTV POG [87]. The reweighing depends on the jet  $p_T$ ,  $\eta$ , and the b-tagging dis-  
<sub>1759</sub> criminant. In this method, there is no migration of events from one b-tag multiplicity  
<sub>1760</sub> bin to another.

### 1761 5.3.20 Jet energy resolution and jet energy smearing

1762 Calibration of jet energies, i.e. ensuring that the energy and momentum of the recon-  
1763 structed jet matches that of the quark/gluon-initiated jet, is a challenging task due  
1764 to time-dependent changes in the detector response and calibration and high pile-  
1765 up [88] [89]. Jet calibration is done via jet energy corrections (JECs) applied to the  
1766  $p_T$  of jets in MC samples, accounting successively for the effects of pile-up, uniformity  
1767 of the detector response, and residual data-simulation jet energy scale differences [90].  
1768 Typical jet energy resolutions reported at  $\sqrt{s} = 8$  TeV in the central rapidities are  
1769 15-20% at 30 GeV and about 10% at 100 GeV [88]. Jet energy corrections are also  
1770 propagated to the missing transverse energy.

1771 Measurements show that the jet energy resolution (JER) in data is worse than  
1772 in simulation, and so the jets in MC need to be smeared to describe the data. JER  
1773 corrections are applied after JEC on MC simulations, and adjust the width of the  $p_T$   
1774 distribution based on pile-up, jet size, and jet flavor [91]. Tools for applying JEC and  
1775 JER are provided centrally by the JER Corrections group.

# 1776 Chapter 6

## 1777 Event selection

1778 This chapter describes how events in data and simulated samples are selected in the  
1779 search for  $h \rightarrow aa \rightarrow bb\tau\tau$ . The event selection is motivated by optimization checks  
1780 aimed at maximizing the final expected limit, and is also based on recommendations  
1781 from CMS Physics Objects Groups. As described in the previous chapter, the tau  
1782 lepton can decay to electrons ( $e$ ), muons ( $\mu$ ), or hadronic states ( $\tau_h$ ). As a result,  
1783 several different final states of the  $\tau\tau$  system are possible, and are here referred to  
1784 as “channels” since they are mutually exclusive. The three  $\tau\tau$  final states studied in  
1785 this analysis are muon and hadronic tau ( $\mu\tau_h$ ), electron and hadronic tau ( $e\tau_h$ ), and  
1786 electron and muon ( $e\mu$ ). The procedure for dividing events into these three channels  
1787 begins with checking the High-Level Trigger paths passed by the events as detailed  
1788 in Section 6.1. Events are further accepted or rejected based on criteria applied to  
1789 the leptons in the event. These event selections are described for the  $\mu\tau_h$  channel in  
1790 Section 6.2, the  $e\tau_h$  channel in Section 6.3, and the  $e\mu$  channel in Section 6.4.

### 1791 6.1 General procedure for all channels

1792 For the search for  $h \rightarrow aa \rightarrow bb\tau\tau$ , three final states of the  $\tau\tau$  system are considered:  
1793  $\mu\tau_h$ ,  $e\tau_h$ , and  $e\mu$ . The  $\tau_h\tau_h$  final state is not considered because signal events in the

1794  $\tau_h\tau_h$  channel would typically produce hadronic taus with momenta below data-taking  
1795 trigger thresholds. In all three final states, events are required to have at least one  
1796 b-tag jet passing the medium working point of the DeepFlavour tagger, with  $p_T > 20$   
1797 GeV, and  $|\eta| < 2.4$ . A second b-tag jet is not required because such a requirement  
1798 would reduce signal acceptance by 80% compared to only requiring one b-tag jet.

1799 Events in MC samples are sorted into one of the three  $\tau\tau$  channels if they pass the  
1800 following trigger requirements and requirements on the offline reconstructed objects  
1801 in the event, first checking the HLT paths for the  $\mu\tau_h$  channel, then  $e\tau_h$ , and finally  $e\mu$ .  
1802 The two leading leptons (e.g. muon and hadronic tau for the  $\mu\tau_h$  channel) that were  
1803 determined to have originated from the  $\tau\tau$  decay, are called the  $\tau\tau$  “legs”. For events  
1804 in data and embedded samples, the HLT paths requirements for the corresponding  
1805 channel are checked.

1806 After sorting events by HLT paths and identifying the leading tau legs in the offline  
1807 reconstructed objects, the  $p_T$  of the offline objects is checked against the online trigger  
1808 thresholds. Trigger matching is also performed, which checks the correspondence  
1809 between each offline reconstructed object used in the analysis (e.g. a muon), and a  
1810 trigger object in the HLT (e.g. a HLT muon). An offline object is considered to be  
1811 matched, if it corresponds to a trigger object of the same object type, with  $\Delta R < 0.5$ .  
1812 This matched trigger object is also required to pass the filter(s) of the HLT trigger.  
1813 The trigger thresholds used for the  $bb\mu\mu$  final state and the  $bb\tau\tau$  final state (the focus  
1814 of this work) are summarized in Tables 6.1.

1815 After checking the HLT paths and trigger objects in each channel, events are  
1816 subject to further selection to ensure that they contain leptons and b-tag jet(s) of in-  
1817 terest. These requirements are summarized in Table 6.2, and detailed in the following  
1818 sections.

Year	Single/dilepton trigger $p_T$	$bb\mu\mu$	$bb\tau\tau$					
			$e\mu$		$e\tau_h$		$\mu\tau_h$	
		$\mu$	$e$	$\mu$	$e$	$\tau_h$	$\mu$	$\tau_h$
2016	Single lepton	24	–	–	25	–	22	–
	$p_T$ -leading lepton	17	23	23	–	–	–	20
	$p_T$ -subleading lepton	8	12	8	–	–	19	–
2017	Single lepton	24	–	–	27, 32	–	24, 27	–
	$p_T$ -leading lepton	17	23	23	–	30	–	27
	$p_T$ -subleading lepton	8	12	8	24	–	20	–
2018	Single lepton	24	–	–	32, 35	–	24, 27	–
	$p_T$ -leading lepton	17	23	23	–	30	–	27
	$p_T$ subleading lepton	8	12	8	24	–	20	–

Table 6.1: Trigger thresholds used for the leptons in the  $bb\mu\mu$  analysis and the  $bb\tau\tau$  analysis (the focus of this work). The thresholds for the three  $bb\tau\tau$  channels ( $e\mu$ ,  $e\tau_h$ , and  $\mu\tau_h$ ) are listed separately, with some channels and years taking the logical OR of two triggers with different thresholds.

## 6.2 Event selection in the $\mu\tau_h$ channel

In all three years, a single muon trigger is used if the muon has sufficiently high  $p_T$ , otherwise a dilepton  $\mu\tau_h$  cross-trigger is used (Tables 6.3, 6.4, and 6.5). For data taken in 2017-2018 (2016), the logical OR of the single muon triggers with online  $p_T$  thresholds 24 and 27 (23) GeV is used, with the corresponding offline muon required to have with  $p_T$  1 GeV above the online threshold. For data taken in 2017-2018 (2016), a dilepton  $\mu + \tau_h$  cross-trigger with  $p_T$  thresholds of 20 (19) and 27 (20) GeV for the muon and tau respectively, is used. The  $\tau_h$  is required to have  $|\eta| < 2.3$  if the single trigger is fired,  $|\eta| < 2.1$ .

The muon and  $\tau_h$  are required to have opposite charge and be separated by  $\Delta R > 0.4$ . The muon is required to have  $|\eta| < 2.4$ , and the  $\tau_h$  is required to have  $|\eta| < 2.3$  unless a cross-trigger is required, in which case we require  $|\eta| < 2.1$  as discussed above.

The muon is required to pass the medium identification (ID) working point [92], which is defined by the Muon POG as a loose muon (i.e. a Particle Flow muon that is either a global or a tracker muon - see Section 5.1.2) with additional requirements

All years (2016, 2017, 2018) and eras				
Kinematic variable	$bb\mu\mu$		$bb\tau\tau$	
	$\mu$	$e\mu$	$e\tau_h$	$\mu\tau_h$
$\Delta R$ between leptons	>0.4	>0.3	>0.4	>0.4
$ \eta $ of electron	-	<2.4	<2.1	-
$ \eta $ of muon	<2.4	<2.4	-	<2.1
$ \eta $ of hadronic tau	-	-	<2.3/< 2.1	<2.3/< 2.1
Relative isolation of electron	-	<0.10	-	<0.15
Relative isolation of muon	<0.25	<0.15	-	<0.15
Leading b-tag jet $p_T$	>15 GeV		>20 GeV	
Leading b-tag jet $ \eta $	<2.4		<2.4	
Leading b-tag jet WP	Tight		Medium	
Sub-leading b-tag jet $p_T$	>15 GeV		-	
Sub-leading b-tag jet $ \eta $	<2.4		-	
Sub-leading b-tag jet WP	Loose		-	
$\Delta R$ between jet(s) and leptons	>0.4		>0.5	

Table 6.2: Summary of requirements applied to the leptons in the  $bb\mu\mu$  analysis and the  $bb\tau\tau$  analysis (the focus of this work).  $\Delta R = \sqrt{(\Delta\eta)^2 + (\Delta\phi)^2}$  is a measure of spatial separation. Relative isolation is defined in Eqn. 5.2 and Section 5.1.2. The b-tag jets are required to pass the listed DeepFlavour working points (WP), which are described in Section 5.1.5. In the  $bb\tau\tau$  analysis, the required  $|\eta|$  of the hadronic taus are listed for the single and cross triggers respectively. The  $bb\mu\mu$  analysis requires two b-tag jets in all events, while the  $bb\tau\tau$  analysis only requires one.

1835 on track quality and muon quality. This identification criteria is designed to be  
1836 highly efficiently for prompt muons and for muons from heavy quark decays. In  
1837 addition to the ID, for prompt muons it is recommended to apply cuts on the impact  
1838 parameter [92]: we apply  $|\Delta(z)| < 0.2$  and  $|\Delta(xy)| < 0.045$ . A cut is applied on the  
1839 muon relative isolation (defined in Section 5.1.2), to be less than 0.15 in a cone size of  
1840  $\Delta R = 0.4$ , which corresponds to the Tight Particle Flow isolation requirement [92].

1841 The  $\tau_h$  is required to pass a cut on its impact parameter of  $|\Delta(z)| < 0.2$ . The  $\tau_h$   
1842 is also required to pass the VLoose (Very Loose) DeepTau working point vs. elec-  
1843 tron, the Tight DeepTau working point vs. muons, and the VVVLoose and Medium  
1844 DeepTau working point vs. jets. Events with taus reconstructed in two of the decay  
1845 modes (labeled 5 and 6) are rejected, since these decay modes are meant to recover  
1846 3-prong taus, but are only recommended for use in analyses where the benefits in final  
1847 significance outweigh the resulting increase in background [65]. Decays reconstructed  
1848 with 2 prongs are not considered as they are only recommended for taus with a very  
1849 high transverse momentum, where the prongs may overlap.

1850 For the estimation of the background from jets faking  $\tau_h$ , which is described in Sec-  
1851 tion 7.7, anti-isolated events are selected, by requiring events to pass all the selections  
1852 described above, except failing the Medium DeepTau working point vs. jets.

### 1853 6.3 Event selection in the $e\tau_h$ channel

1854 The HLT trigger paths for the  $e\tau_h$  channel are summarized in Tables 6.3, 6.4, and  
1855 6.5. Similarly to the  $\mu\tau_h$  channel, a single electron trigger is used if the electron has  
1856 sufficiently high  $p_T$  in 2018 and 2017. For data taken in 2018 (2017), the OR of the  
1857 single electron triggers with online  $p_T$  thresholds at 32 and 35 (27 and 32) GeV are  
1858 used, with the corresponding offline electrons required to have  $p_T$  greater than 33  
1859 (28) GeV. A  $e + \tau_h$  cross-trigger is used for electrons with lower offline  $p_T$  between

1860 25 and 33 GeV (25 and 28 GeV). For the 2016 dataset, there is no cross trigger but  
1861 only a single electron trigger with online  $p_T$  threshold at 25 GeV, which is used if the  
1862 offline electron has  $p_T$  greater than 26 GeV.

1863 The electron and  $\tau_h$  are required to have opposite charge and be separated by  
1864  $\Delta R > 0.4$ . The electron is required to be within  $|\eta| < 2.3$  when no cross trigger is  
1865 used, and  $|\eta| < 2.1$  when the cross trigger is fired. The  $\tau_h$  is required to have  $|\eta| < 2.3$   
1866 if no cross trigger is fired, and have  $|\eta| < 2.1$  if the cross trigger is fired.

1867 The electron is required to have a relative isolation (same definition as in Section  
1868 5.1.2) of less than 0.1 in a cone size of  $\Delta R = 0.3$ , which is the standard recommended  
1869 cone size giving minimal pile-up dependence and reduced probability of other objects  
1870 overlapping with the cone. The isolation quantity used includes an “effective area”  
1871 (EA) correction to remove the effect of pile-up in the barrel and endcap parts of the  
1872 detector [93].

1873 The electron is also required to pass cuts on its impact parameter of  $|\Delta(z)| < 0.2$   
1874 and  $|\Delta(xy)| < 0.045$ . It is also required to pass the non-isolated MVA working point  
1875 corresponding to 90% efficiency. The electron’s number of missing hits, which are  
1876 gaps in its trajectory through the inner tracker [93], must be less than or equal to  
1877 1. The electron must pass a conversion veto, which rejects electrons coming from  
1878 photon conversions in the tracker, which should instead be reconstructed as part of  
1879 the photon [93].

1880 The impact parameter cut for the  $\tau_h$  is  $|\Delta(z)| < 0.2$ . In contrast to the  $\mu\tau_h$  event  
1881 selection, the vs. electron and vs. muon DeepTau working points are flipped, to  
1882 reject muons faking the  $\tau_h$  leg. The  $\tau_h$  is required to pass the Tight DeepTau working  
1883 point vs. electrons, the VLoose DeepTau working point vs. muons, and the Medium  
1884 DeepTau working point vs. jets.

1885 As in the  $\mu\tau_h$  channel, for the estimation of the background from jets faking  $\tau_h$ ,  
1886 which is described in Section 7.7, anti-isolated events are selected, by requiring events

1887 to pass all the selections described above, except failing the Medium DeepTau working  
1888 point vs. jets.

## 1889 6.4 Event selection in the $e\mu$ channel

1890 The HLT trigger paths for the  $e\mu$  channel are summarized in Tables 6.3, 6.4, and  
1891 6.5. Events are selected with the logical OR of two  $e + \mu$  cross triggers, where either  
1892 the electron or muon can have larger  $p_T$ : (1) leading electron, where the electron has  
1893 online  $p_T > 23$  GeV and muon has online  $p_T > 8$  GeV, or (2) leading muon, where  
1894 electron has online  $p_T > 12$  GeV and muon has online  $p_T > 23$  GeV.

1895 The leading and sub-leading leptons are required to have an offline  $p_T$  greater  
1896 than 1 GeV above the online threshold (i.e.  $p_T > 24$  GeV). If the sub-leading lepton  
1897 is the electron, the offline  $p_T$  threshold is 1 GeV above the online threshold ( $p_T > 13$   
1898 GeV), but if it is a muon, the offline  $p_T$  threshold is required to be at least 5 GeV  
1899 greater than the online threshold (i.e.  $p_T > 13$  GeV). This is because of poor data  
1900 and simulation agreement for low- $p_T$  muons with  $p_T$  between 9 GeV and 13 GeV, and  
1901 the higher probability of mis-identifying jets as muons at lower  $p_T$ . With no effect on  
1902 the expected limits, the offline  $p_T$  threshold for muons is raised to 13 GeV instead of  
1903 9 GeV, even though it may lead to loss in signal acceptance. Both the electron and  
1904 muon are required to be have  $|\eta| < 2.4$ .

1905 The electron and muon are required to have opposite charge and be separated  
1906 by  $\Delta R > 0.3$  (note the decreased separation requirement compared to the other  
1907 two channels). The electron is required to pass the non-isolated MVA identification  
1908 working point corresponding to 90% efficiency, and to have a relative isolation less  
1909 than 0.1 for a cone size of  $\Delta R = 0.3$  with the EA pile-up subtraction correction.  
1910 The electron must have one or fewer missing hits and pass the conversion veto (both  
1911 described previously in Section 6.3).

1912      The muon is required to pass the medium identification working point (described  
 1913      earlier in 6.2), and to have a relative isolation less than 0.15 for a cone size of  $\Delta R =$   
 1914      0.4. The muon impact parameter is required to have  $|\Delta(z)| > 0.2$  and  $|\Delta(xy)| < 0.045$ .  
 1915      For the QCD multijet background estimation described in Section 7.8, the same-  
 1916      sign region is selected by requiring all the above selections, except the legs are required  
 1917      to have the same electric charge rather than opposite.

2016 $\mu\tau_h$ trigger paths	
Notes	HLT Path
	HLT_IsoMu22_v
	HLT_IsoMu22_eta2p1_v
	HLT_IsoTkMu22_v
	HLT_IsoTkMu22_eta2p1_v
	HLT_IsoMu19_eta2p1_LooseIsoPFTau20_v
	HLT_IsoMu19_eta2p1_LooseIsoPFTau20_SingleL1_v
2016 $e\tau_h$ trigger paths	
Notes	HLT Path
	HLT_Ele25_eta2p1_WPTight_Gsf_v
2016 $e\mu$ trigger paths	
Notes	HLT Path
runs B-F and MC	HLT_Mu23_TrkIsoVVL_Ele12_CaloIdL_TrackIdL_IsoVL_v
runs B-F and MC	HLT_Mu8_TrkIsoVVL_Ele23_CaloIdL_TrackIdL_IsoVL_v
runs G-H	HLT_Mu23_TrkIsoVVL_Ele12_CaloIdL_TrackIdL_IsoVL_DZ_v
runs G-H	HLT_Mu8_TrkIsoVVL_Ele23_CaloIdL_TrackIdL_IsoVL_DZ_v

Table 6.3: High-Level Trigger (HLT) paths used to select data and simulation events in 2016 for the three  $\tau\tau$  channels.

## 1918      6.5 Extra lepton vetoes in all channels

1919      Events containing a third lepton (electron or muon) that is neither of the leading  $\tau\tau$   
 1920      legs are rejected, and events with di-muons and di-electrons are vetoed, with criteria  
 1921      taken from the Standard Model  $H \rightarrow \tau\tau$  working group [68]. These vetoes on extra  
 1922      leptons also ensure orthogonality of events to analyses such as the  $bb\mu\mu$  final state,  
 1923      whose results are combined with this  $bb\tau\tau$  final state as described in Section 10.2.

2017 $\mu\tau_h$ trigger paths	
Notes	HLT Path
	HLT_IsoMu24_v
	HLT_IsoMu27_v
	HLT_IsoMu20_eta2p1_LooseChargedIso_PFTau27_eta2p1_CrossL1_v
2017 $e\tau_h$ trigger paths	
Notes	HLT Path
	HLT_Ele32_WPTight_Gsf_v
	HLT_Ele35_WPTight_Gsf_v
	HLT_Ele24_eta2p1_WPTight_Gsf_Loose_ChargedIsoPFTau30_eta2p1_CrossL1_v
2017 $e\mu$ trigger paths	
Notes	HLT Path
	HLT_Mu23_TrkIsoVVL_Ele12_CaloIdL_TrackIdL_IsoVL_DZ_v
	HLT_Mu8_TrkIsoVVL_Ele23_CaloIdL_TrackIdL_IsoVL_DZ_v

Table 6.4: High-Level Trigger (HLT) paths used to select data and simulation events in 2017 for the three  $\tau\tau$  channels.

1924        The event is vetoed if a third electron is found with the following properties:  
 1925         $p_T > 10$  GeV,  $|\eta| < 2.5$ , impact parameter  $|\Delta(z)| < 0.2$  and  $|\Delta(xy)| < 0.045$ , passing  
 1926        non-isolation MVA identification with 90% efficiency, conversion veto,  $\leq 1$  missing  
 1927        hits, and relative isolation  $< 0.3$  with cone size  $\Delta R = 0.3$ . The event is also vetoed if  
 1928        a third muon is found with the following properties:  $p_T > 10$  GeV,  $|\eta| < 2.4$ , impact  
 1929        parameter  $|\Delta(z)| < 0.2$  and  $|\Delta(xy)| < 0.045$ , medium ID, and isolation  $< 0.3$  with  
 1930        cone size  $\Delta R = 0.4$ .

1931        A di-muon veto is applied, which rejects events containing a pair of muons with  
 1932        opposite charge and separation of  $\Delta R > 0.15$ , that both pass the following selections:  
 1933         $p_T > 15$  GeV,  $|\eta| < 2.4$ , flag for global muons, flag for tracker muon, flag for Particle  
 1934        Flow muon,  $|\Delta(z)| < 0.2$ ,  $|\Delta(xy)| < 0.045$ , and isolation  $< 0.3$  with cone size  $\Delta R =$   
 1935        0.4. A similar di-electron veto is applied to reject events containing a pair of electrons  
 1936        with opposite charge and separation of  $\Delta R > 0.15$ , that both pass the following  
 1937        selections:  $p_T > 15$  GeV,  $|\eta| < 2.5$ , a dedicated electron ID (cut-based) for vetoing  
 1938        third leptons,  $|\Delta(z)| < 0.2$ ,  $|\Delta(xy)| < 0.045$ , with pile-up corrected relative isolation  
 1939         $< 0.3$  with cone size  $\Delta R = 0.3$ .

2018 $\mu\tau_h$ trigger paths	
Notes	HLT Path
	HLT_IsoMu24_v
	HLT_IsoMu27_v
only data run < 317509	HLT_IsoMu20_eta2p1_ (contd.)
	LooseChargedIsoPFTauHPS27_eta2p1_CrossL1_v
MC and data run $\geq$ 317509	HLT_IsoMu20_eta2p1_ (contd.)
	LooseChargedIsoPFTauHPS27_eta2p1_TightID_CrossL1_v
2018 $e\tau_h$ trigger paths	
Notes	HLT Path
	HLT_Ele32_WPTight_Gsf_v
	HLT_Ele35_WPTight_Gsf_v
only data run < 317509	HLT_Ele24_eta2p1_WPTight_Gsf_ (contd.)
	LooseChargedIsoPFTauHPS30_eta2p1_CrossL1_v
MC and data run $\geq$ 317509	HLT_Ele24_eta2p1_WPTight_Gsf_ (contd.)
	LooseChargedIsoPFTauHPS30_eta2p1_TightID_CrossL1_v
2018 $e\mu$ trigger paths	
Notes	HLT Path
	HLT_Mu23_TrkIsoVVL_Ele12_CaloIdL_TrackIdL_IsoVL_DZ_v
	HLT_Mu8_TrkIsoVVL_Ele23_CaloIdL_TrackIdL_IsoVL_DZ_v

Table 6.5: High-Level Trigger (HLT) paths used to select data and simulation events in 2018 for the three  $\tau\tau$  channels. In 2018 a HLT trigger path using the hadron plus strips (HPS) tau reconstruction algorithm became available.

# <sup>1940</sup> Chapter 7

## <sup>1941</sup> Background estimation

<sup>1942</sup> This section describes methods used to estimate sources of background from Standard  
<sup>1943</sup> Model processes in the search for  $h \rightarrow aa \rightarrow bb\tau\tau$ . Similar background estimation  
<sup>1944</sup> methods are being used for the  $h \rightarrow a_1a_2$  analysis. The background contributions  
<sup>1945</sup> directly taken from MC are described in Sections 7.1 to 7.6. Section 7.7 describes  
<sup>1946</sup> the data-driven method for estimating backgrounds from jets faking hadronic tau  
<sup>1947</sup> decays ( $\text{jet} \rightarrow \tau_h$ ), which is used in the  $\mu\tau_h$  and  $e\tau_h$  channels. Section 7.8 describes  
<sup>1948</sup> the data-driven method for estimating background from quantum chromodynamic  
<sup>1949</sup> (QCD) processes in the  $e\mu$  channel.

### <sup>1950</sup> 7.1 Z+jets

<sup>1951</sup> A major source of background for  $\tau\tau$  analyses is the Drell-Yan (DY) process (Z+jets).  
<sup>1952</sup> The Z boson decays to  $\tau\tau/\mu\mu/ee$  with equal probability of 3.4% each, with the domi-  
<sup>1953</sup> nant decay modes being to hadrons (around 70%) and neutrinos (invisible) (20%) [26].  
<sup>1954</sup> The Drell-Yan contribution with genuine taus,  $Z \rightarrow \tau\tau$ , is estimated using embed-  
<sup>1955</sup> ded samples, described in Section 4.3. To avoid double-counting between embedded  
<sup>1956</sup> and MC samples, in all MC samples, events with legs that originated from genuine  $\tau$   
<sup>1957</sup> are discarded.

1958 The other decays of the  $Z$ ,  $Z \rightarrow ee$  and  $Z \rightarrow \mu\mu$ , are estimated from MC simulation,  
1959 and are hereafter referred to as simply the Drell-Yan background. These MC samples  
1960 are generated to leading order (LO) with different numbers of jets (jet multiplicity) in  
1961 the matrix element:  $Z+1$  jet,  $Z+2$  jets,  $Z+3$  jets,  $Z+4$  jets, and inclusive  $Z+jets$ . The  
1962 cross-sections of the samples with  $\geq 1$  jets are normalized to next-to-NLO (NNLO)  
1963 in QCD.

1964 For the inclusive Drell-Yan sample, two samples are used with different thresholds  
1965 for the di-lepton invariant mass ( $m_{\ell\ell}$ ) at the generator level: one with  $m_{\ell\ell} > 50$  GeV  
1966 and the other with  $10 < m_{\ell\ell} < 50$ .

## 1967 7.2 W+jets

1968 The dominant  $W$  boson decay modes are to hadrons (67.4%),  $e + \nu_e$  (10.7%),  $\mu + \nu_\mu$   
1969 (10.6%), and  $\tau + \nu_\tau$  (11.4%) [26]. The  $W+jets$  background is estimated from MC  
1970 simulation. Similarly to the  $Z+jets$ , the  $W+jets$  samples are generated with different  
1971 jet multiplicities in the matrix element. LO samples are used for greater statistics  
1972 and are normalized to NNLO cross sections.

## 1973 7.3 $t\bar{t} + jets$

1974 In hadron collisions, top quarks are produced singly with the weak interaction, or in  
1975 pairs via the strong interaction, with interference between these leading-order pro-  
1976 cesses possible in higher orders of the perturbation theory. The top quark is the  
1977 heaviest fermion in the Standard Model and has a short lifetime ( $\sim 10^{-25}$  s), decay-  
1978 ing without hadronization into a bottom quark and a  $W$  boson [26], with the decay  
1979 modes of the  $W$  boson as listed in the previous section. With two top quarks, the  
1980 final states of the two resulting  $W$  bosons can be described as fully leptonic, semilep-  
1981 tonic, and fully hadronic. These three final states are modeled separately with MC

1982 simulation in 2018 and 2017, while for 2016 the sample used is inclusive.

## 1983 7.4 Single top

1984 There are three main production modes of the single top in  $pp$  collisions [94]: the  
1985 exchange of a virtual W boson ( $t$  channel), the production and decay of a virtual W  
1986 boson ( $s$  channel), and the associated production of a top quark and W boson ( $tW$ ,  
1987 or W-associated) channel. As the  $s$  channel process is rare and only 3% of the total  
1988 production, the dominant production mode of the  $t$ -channel and the  $tW$  production  
1989 are considered and modeled with MC.

## 1990 7.5 Diboson

1991 In  $pp$  collisions, the production of dibosons (pairs of electroweak gauge bosons, i.e.  
1992 WW, WZ, and ZZ) is dominated by quark-antiquark annihilation, with a small con-  
1993 tribution from gluon-gluon interaction [95]. MC is used to model the pair production  
1994 and decays of VV to  $2\ell 2\nu$ , WZ to  $2q 2\ell$  and  $3\ell\nu$ , and ZZ to  $4\ell$  and  $2q 2\ell$  ( $q$  being  
1995 quarks and  $\ell$  being leptons).

## 1996 7.6 Standard Model Higgs

1997 MC is used to simulate backgrounds from major production modes of the Standard  
1998 Model 125 GeV Higgs boson: gluon-gluon fusion (ggH), vector boson fusion (VBF),  
1999 associated production with a W or Z (WH, ZH), and associated production with a  
2000 top pair (ttH) (see Fig. 7.1 for leading-order diagrams). For these production modes,  
2001 samples with the Higgs decaying to  $\tau\tau$  or to  $WW$  are used. Samples made with  
2002 higher-order diagrams for WH and ZH that include the production of a jet, with the  
2003 Higgs decaying to WW, are also used.

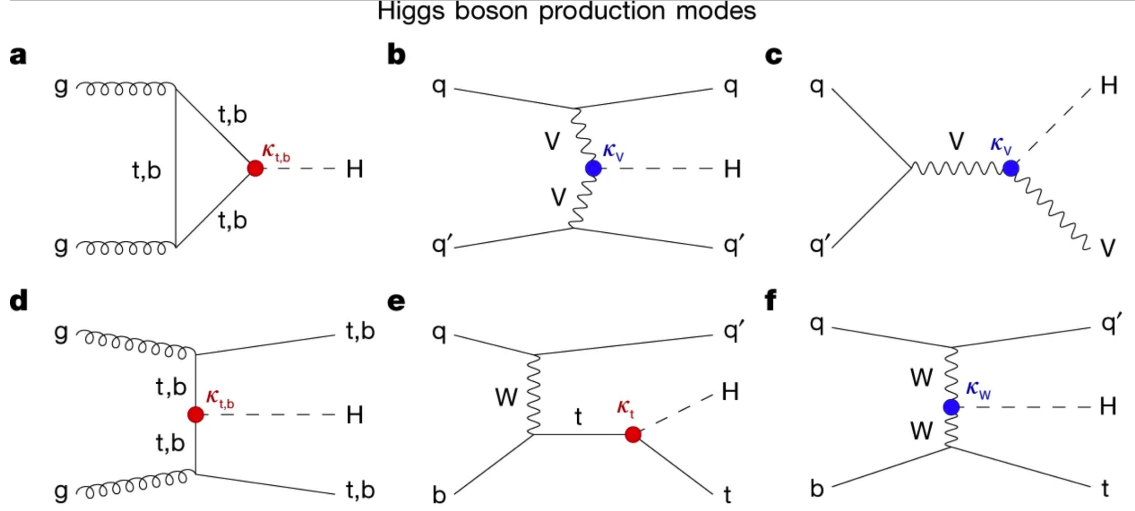


Figure 7.1: Leading-order Feynman diagrams of Higgs production from [96], in ggH (a) and vector boson fusion (VBF; b), associated production with a W or Z (V) boson (VH; c), associated production with a top or bottom quark pair (ttH or bbH); d, and associated production with a single top quark (tH; e, f).

## 2004 7.7 Jet faking $\tau_h$

Events with a jet mis-reconstructed as the hadronic tau leg  $\tau_h$  are a major source of background in the  $\mu\tau_h$  and  $e\tau_h$  channels. The main processes contributing to jet  $\rightarrow \tau_h$  events are QCD multijet, W+jets, and  $t\bar{t}$  production. These events are estimated using a data-driven method adapted from past analyses [50] [84]. This background includes contributions from W+jets, QCD multijets, and  $t\bar{t}$ +jets. To estimate this background, a sideband region is constructed, where events are required to pass all baseline  $\mu\tau_h/e\tau_h$  selection criteria, but fail the  $\tau_h$  isolation criteria. The events in this sideband region are reweighed with a factor  $f/(1 - f)$ , where  $f$  is the probability for a jet to be misidentified as a  $\tau_h$ . The jet  $\rightarrow \tau_h$  background is the anti-isolated, reweighed MC and embedded events subtracted from the anti-isolated, reweighted data events.

The fake factor is measured in  $Z \rightarrow \mu\mu + \text{jets}$  events in data in the  $\mu\mu\tau_h$  final state, as any reconstructed  $\tau_h$  in these events must originate from a jet. The two muons are required to be isolated ( $< 0.15$ ), have opposite electric charge, and have

2019 an invariant mass between 76 and 106 GeV (close to the Z mass). These events are  
2020 selected with a double muon trigger, with the leading muon having offline  $p_T > 20$   
2021 GeV and the subleading muon  $p_T > 10$  GeV. Simulated diboson (ZZ and WZ) events  
2022 are subtracted to avoid contamination from events with real  $\tau_h$ . The denominator of  
2023 the fake rate corresponds to fake taus passing the VVVLoose working point of the  
2024 discriminator vs. jets, while the numerator corresponds to those passing the Medium  
2025 working point, i.e.  $f = N_{\text{jet passing tight}} / N_{\text{jet passing loose}}$ .

2026  $f$  is measured as a function of the  $\tau_h$  transverse momentum and is 8% - 10% in  
2027 each of the data-taking years.  $f$  is derived separately for the  $\mu\tau_h$  and  $e\tau_h$  channels  
2028 because the channels use different anti-lepton identification working points.

## 2029 7.8 QCD multijet background

2030 In the  $e\mu$  channel, events with jets faking electrons or muons originating from QCD  
2031 multijet, is estimated from data events with the same baseline selection as in the  
2032 signal region, except with same-signed (SS) charged  $e + \mu$ , ensuring orthogonality  
2033 with the signal region which requires opposite-sign (OS)  $e\mu$  pairs. All same-sign MC  
2034 events (both events with real and fake  $e + \mu$ ) are subtracted from same-sign data  
2035 events to remove contamination from other backgrounds. i.e.  $\text{QCD}_{\text{SS}} = \text{Data}_{\text{SS}} -$   
2036  $\text{MC}_{\text{SS}}$ .

2037 Three scale factors are applied to the  $\text{QCD}_{\text{SS}}$  events to compute the QCD multijet  
2038 background [84] [40]:

- 2039 • *OS-to-SS scale factor*: This scales the SS QCD to the OS region, and is mea-  
2040 sured from an orthogonal region with an isolated electron and an anti-isolated  
2041 muon. Only the muon is chosen to be anti-isolated because this scale factor was  
2042 observed to depend more strongly on electron isolation than that of the muon.  
2043 This scale factor is treated as a function of the  $\Delta R$  separation of the trajectories

2044 of the electron and muon, and is measured separately for events with 0 jets, 1,  
2045 jet, and greater than 1 jet.

- 2046 • *2D closure correction for the lepton  $p_T$ :* This factor accounts for subleading  
2047 dependencies of the first scale factor on the  $p_T$  of the two leptons. A 2D weight  
2048 is derived in a similar fashion, as a ratio of  $\text{QCD}_{OS}$  events to  $\text{QCD}_{SS}$  events,  
2049 but parameterized by both electron and muon  $p_T$ , where the SS events have the  
2050 previous scale factor applied.
- 2051 • *Isolation correction for the muon:* The third and final factor is an isolation  
2052 correction, which is a bias correction to account for the fact that the fake  
2053 factor was determined for less-isolated muons. This factor is obtained as the  
2054 ratio of the OS-to-SS scale factors measured in two other control regions: (1)  
2055 events where the electron is anti-isolated ( $0.15 < \text{iso} < 0.5$ ) and the muon is  
2056 isolated, and (2) events where both leptons are anti-isolated.

2057

# Chapter 8

2058

## Systematic uncertainties

2059 Uncertainties in the measurement of a physical observable can be statistical or sys-  
2060 tematic in nature. Statistical uncertainties originate from limitations on the number  
2061 of events and experiments that can be performed. Systematic uncertainties arise  
2062 from the dependence of the physical observable on quantities whose exact values are  
2063 unknown and which can only be modeled imperfectly.

2064 The handling of systematic uncertainties is separated into normalization uncer-  
2065 tainties (those that affect the total yield of a variables' distribution) and shape un-  
2066 certainties (those that shift the distribution of events). Normalization uncertainties  
2067 are expressed as multiplicative factors, while shape uncertainties are represented as  
2068 up and down shifts of a variable's distribution.

2069 Up/down shifts of shape uncertainties can change the number of background  
2070 events in a distribution. For instance, hadronic taus receive corrections from the  
2071 nominal tau energy scale, with the nominal, up, and down energy scales provided  
2072 centrally by CMS. For the  $\mu\tau_h$  channel, an event could have a  $\tau_h$  with  $p_T$  just below  
2073 the offline threshold of 20 GeV (for instance, 19.5 GeV), so in the nominal distribution  
2074 of  $m_{\tau\tau}$  (or any other variable for this channel), the event is excluded. However, when  
2075 we build our distributions with the tau energy scale “up” shift, the energy of this  $\tau_h$

2076 may be scaled up to, say, 20.5 GeV, and now the event passes the offline  $p_T$  threshold  
2077 for the single muon trigger, leading to the event’s inclusion in the distributions made  
2078 with the tau energy scale “up” shift.

2079 In evaluating the up and down shifts of a specific source of uncertainty, all other  
2080 corrections and scale factors are held at their nominal values, and the full chain of  
2081 object and event selection and event categorization is performed to obtain the observ-  
2082 able distributions. Any “downstream” variables that depend on the shifted variable,  
2083 e.g. the invariant di-tau mass  $m_{\tau\tau}$ , must be computed for the nominal case, and then  
2084 re-computed separately for each up and down shift of the tau legs’ energy scale. The  
2085 objective of this process is to quantify the effect of a single source of uncertainty on  
2086 the resulting observable distributions. Each scale factor and correction described in  
2087 Section 5.3 has an associated uncertainty. The binning of the uncertainties follows  
2088 that of the nominal scale factor value.

2089 Sections 8.1 to 8.5 describe uncertainties associated with physics objects, and  
2090 Sections 8.6 and 8.7 describe uncertainties associated with sample-level effects. The  
2091 pulls and impacts for the top sixty most important systematics are shown in Section  
2092 8.8.

## 2093 8.1 Uncertainties in the lepton energy scales

2094 The uncertainties in the tau energy scales [65] are binned by the tau decay mode and  
2095 are taken as shape uncertainties treated as uncorrelated across the tau decay modes  
2096 and years. Same as with the application of the nominal scale factor, when applying  
2097 the up or down shifts, the missing transverse energy ( $p_T^{\text{miss}}$ ) of the event is adjusted  
2098 so that the 4-vector sum of the tau  $p_T^{\text{miss}}$  is unchanged.

2099 The uncertainties in the muon energy scale [66] are 0.4% for  $|\eta| < 1.2$ , 0.9% for  
2100  $1.2 < |\eta| < 2.1$ , and 2.7% for  $2.1 < |\eta| < 2.4$ , and are treated as shape uncertainties,

2101 fully uncorrelated between embedded and MC samples.

2102 The uncertainties in the electron energy scale [69] in MC are binned in the electron  
2103  $|\eta|$  and  $p_T$ , and are shown in Fig. 5.2. The uncertainties range from 0.5% to 2.2% in  
2104 the barrel, and 0.3% to 4.1% in the endcap, across the  $p_T$  range. The uncertainties  
2105 for the embedded sample are binned only in  $|\eta|$  and are on the order of 0.5% and  
2106 1.25% for the barrel and endcap [73].

2107 There are also uncertainties in the energy scales for electrons and muons misiden-  
2108 tified as  $\tau_h$ . The uncertainty for muons misidentified as  $\tau_h$  is 1% [65]. For electrons  
2109 misidentified as  $\tau_h$ , the uncertainty is binned in barrel/endcap  $\eta$  and by 1-prong and  
2110 1-prong +  $\pi_0$  decays. The probability for  $e/\mu$  faking a 3-prong decay mode is much  
2111 lower.

## 2112 8.2 Uncertainties from other lepton corrections

2113 Uncertainties associated with the  $\tau_h$  identification efficiencies are treated as shapes,  
2114 uncorrelated across the seven  $p_T$  bins and years. The shape uncertainties in the  
2115 embedded samples are taken as 50% correlated with those of the MC samples.

2116 The uncertainties on electron and muon identification efficiencies are taken as  
2117 normalization uncertainties of 2% each, with a 50% correlation between embedded  
2118 and MC samples.

2119 In the  $e\tau_h$  channel, there is an additional uncertainty for the vs. jet discrimination  
2120 efficiency [65], because the analysis uses a looser anti-lepton working point (VLoose  
2121 WP) than the working points used in the measurement of the efficiency (namely,  
2122 VLoose WP vs e, and Tight WP vs mu). For nominal  $\tau_h p_T < 100$  GeV, an additional  
2123 uncertainty of 3% (5%) is used in MC (embedded), and for high  $p_T$  an uncertainty of  
2124 15% is used for both.

2125 The uncertainties in trigger efficiencies are taken as shapes [65]. In the  $e\tau_h$  and  $\mu\tau_h$

2126 channels, there are uncertainties for the single and cross lepton triggers, and in the  
2127  $e\mu$  channel there is one uncertainty each for the two  $e + \mu$  triggers, and one combined  
2128 uncertainty since their trigger phase spaces are not mutually exclusive.

2129 

### 8.3 Uncertainties from jet energy scale and reso- 2130 lution

2131 The jet energy scale uncertainties are taken as shape uncertainties: there are eleven  
2132 in total, with seven correlated across years (labeled “Year” below) and the remainder  
2133 uncorrelated across years. They affect the b-tag jet  $p_T$  and mass, and hence the  
2134 missing transverse energy  $p_T^{\text{miss}}$ . The shifts are propagated through the b-tagging  
2135 scale factor calculation and b-tag jet counting.

2136 The uncertainties in the jet energy correction and resolution [88] [97] are as follows:

- 2137 • *Absolute, AbsoluteYear*: flat absolute scale uncertainties.
- 2138 • *BBEC1, BBEC1Year*: for sub-detector regions, with barrel “BB” in  $|\eta| < 1.3$   
2139 and endcap region 1 “EC1”:  $1.3 < |\eta| < 2.5$ .
- 2140 • *EC2, EC2 year*: for sub-detector regions, with endcap region 2 “EC2” in  $2.5 <$   
2141  $|\eta| < 3.0$ .
- 2142 • *HF, HF year*: for sub-detector regions, with hadron forward “HF” in  $|\eta| > 3$ .
- 2143 • *FlavorQCD*: for uncertainty in jet flavor (uds/c/b-quark and gluon) estimates  
2144 based on comparing Pythia and Herwig (different MC generator) predictions.
- 2145 • *RelativeBal*: account for difference between log-linear fits of the two methods  
2146 used to study the jet energy response: MPF (missing transverse momentum  
2147 projection fraction) and  $p_T$  balance.

- 2148     • *RelativeSample*: account for  $\eta$ -dependent uncertainty due to a difference be-  
 2149       tween relative residuals, observed with dijet and Z+jets in Run D of 2018 data.
- 2150     • *JetResolution*: uncertainty in the jet energy resolution.

## 2151   8.4 Uncertainties from b-tagging scale factors

2152   The b-tagging scale factor has its own set of associated uncertainties (not to be  
 2153   confused with shifts in the b-tagging scale factor due to the propagation of the jet  
 2154   energy scale uncertainties described in the previous section 8.3). They are:

- 2155     • *hf*: contamination from heavy flavor (b+c) jets in the light flavor region.
- 2156     • *hfstats1, hfstats2*: linear and quadratic statistical fluctuations from b-flavor jets.
- 2157     • *lf*: contamination from light flavor (udsg+c jets) in the heavy flavor region.
- 2158     • *lfstats1, lfstats2*: linear and quadratic statistical fluctuations from udsg jets.
- 2159     • *cferr, cferr2*: uncertainty for charm jets.

2160   The variations for “lf, hf, hfstats1/2, lfstats1/2” are applied to both b and udsg jets.  
 2161   For c-flavor jets, only “cferr1/2” is applied.

## 2162   8.5 Uncertainties from MET

2163   Samples where recoil corrections were applied (Z+jets, W+jets, and Standard Model  
 2164   Higgs, as described in Section 5.3) have uncertainties from the response and resolution  
 2165   of the hadronic recoil against the leptonic system. These are each binned in jet  
 2166   multiplicity.

## 2167 8.6 Uncertainties associated with samples used

2168 Normalization uncertainties related to the samples used are:

2169 • *Cross-section uncertainties*:  $\sigma(t\bar{t})$ : 4.2%,  $\sigma(\text{diboson})$ : 5%,  $\sigma(\text{single top})$ : 5%,  
2170  $\sigma(\text{ggH})$ : 3.2%,  $\sigma(\text{qqH})$ : 2.1%,  $\sigma(\text{WH})$ : 1.9%,  $\sigma(\text{ZH})$ : 1.3%,  $\sigma(\text{ttH})$ : 3.6%

2171 • *Uncertainties in QCD renormalization scale*: QCD scale(qqH): +0.43%-0.33%,  
2172 QCD scale(WH): +0.5%-0.7%, QCD scale(ttH): +5.8%-9.2%

2173 • *Branching ratio uncertainties*:  $\text{BR}(\text{H} \rightarrow \tau\tau)$ : 1.8%, and  $\text{BR}(\text{H} \rightarrow \text{WW})$ : 1.5%.

2174 • *Normalization uncertainties*: 2% for Drell-Yan, 4\$ for embedded, 20% pre-fit  
2175 for the QCD multijet background in the  $e\mu$  channel, 20% pre-fit for the jet  
2176 faking background.

2177 The  $t\bar{t}$  process has additional acceptance uncertainties from QCD scale variation  
2178 and parton shower uncertainties [98]. Parton shower uncertainties originate from  
2179 the modeling of perturbative and non-perturbative QCD effects handled in parton  
2180 shower MC generators. The scale variations are determined from the envelope of the  
2181 6 provided shapes due to variations in the factorization scale, renormalization scale,  
2182 and their combined variation [98].

2183 The Z  $p_T$  reweighting uncertainty in Drell-Yan samples is taken to be 10% of the  
2184 nominal value, taken as a shape uncertainty.

2185 The fake rate uncertainties are taken as shape uncertainties. For the weight ap-  
2186 plied to scale up anti-isolated events in cross-trigger regions, 20% of the nominal  
2187 weight is taken as a shape uncertainty.

## 2188 8.7 Other uncertainties

2189 A 3.6% yield uncertainty in the signal is used to cover uncertainties in the parton  
2190 distribution functions,  $\alpha_s$  (fine structure constant), and QCD scale.

2191      Normalization uncertainties from luminosity are applied to all MC samples, di-  
2192      vided into those uncorrelated across years, those correlated between 2017 and 2018,  
2193      and one for 2018 [85].

## 2194    8.8 Pulls and impacts

2195    The top impacts and pulls computed for the combination of all channels and years is  
2196    shown in Fig. 8.1. The top impacts are related to uncertainty in the signal sample and  
2197    cross-section of the  $t\bar{t}$  cross-section, and also the yields of the jet faking  $\tau_h$  background,  
2198    which is a major background in all channels and expected to be constrained due to  
2199    the yield uncertainty which is taken to be 20% pre-fit.

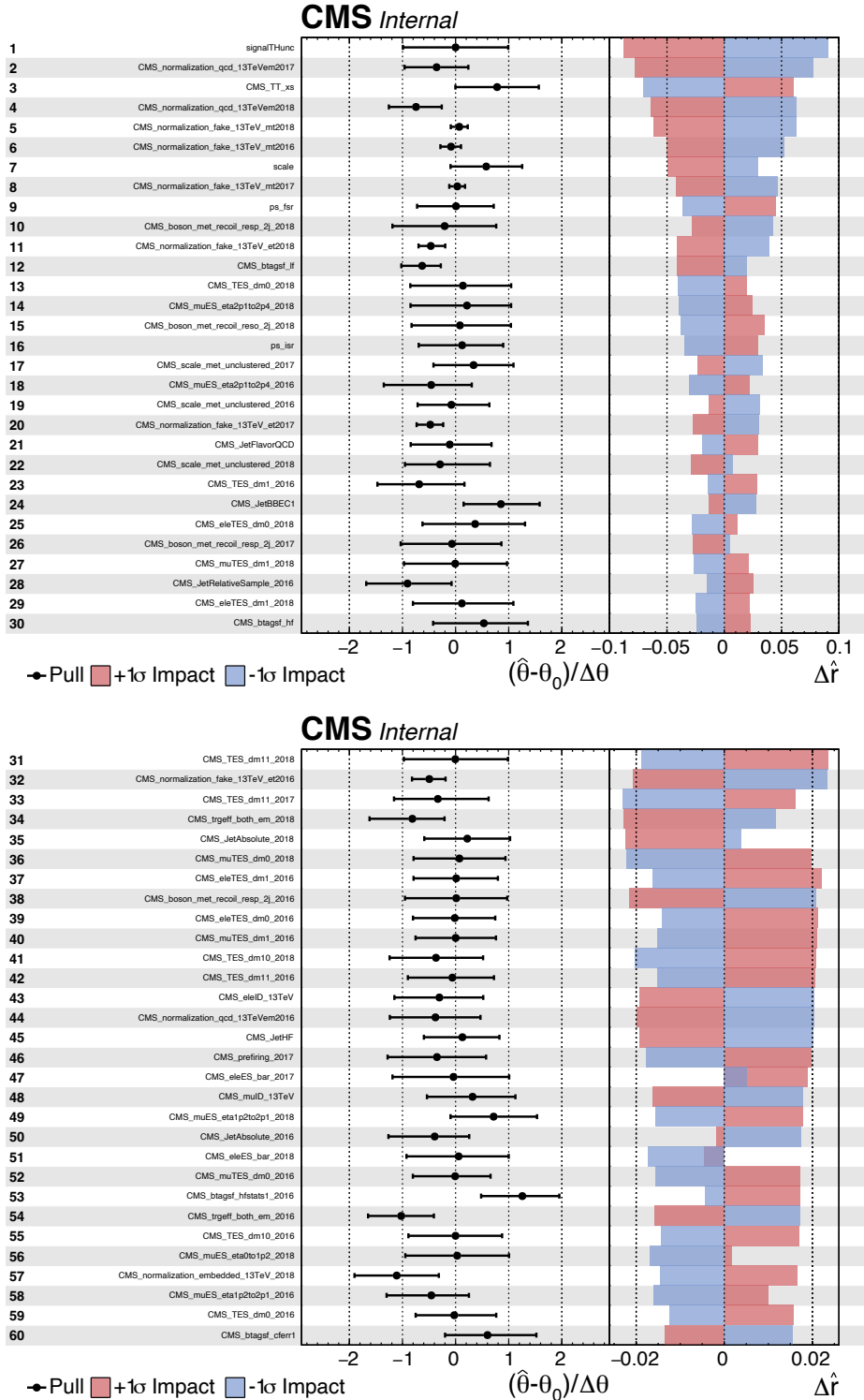


Figure 8.1: Top sixty pulls and impacts for the combination of all channels and years [99].

2200 **Chapter 9**

2201 **Event categorization and signal  
2202 extraction**

2203 Measured events are divided into categories, based on cuts on values of observables  
2204 in the event, or some derived quantity based on the observables in the event. The  
2205 objective of event categorization is to divide events into signal regions, where the  
2206 signal is enhanced and the background is suppressed, and control regions, which are  
2207 signal-poor and used to check that the background estimation methods employed in  
2208 the analysis in fact accurately models the data. In this analysis, events in each tau-tau  
2209 channel are selected to contain one or more b-tag jets reconstructed in the event as  
2210 described in Section 9.1. Events are further divided into signal and control regions  
2211 using a deep learning-based approach described in Section 9.2. The signal is extracted  
2212 from the di-tau mass distribution in the signal region using the statistical procedure  
2213 described in Section 9.3.

2214 **9.1 B-tag jet multiplicity**

2215 The increased statistics of the full Run-2 dataset enables the separation of events into  
2216 events with exactly 1 b-tag jet and events with greater than 1 b-tag jet. Further event

2217 categorization is performed with deep neural networks (DNNs) described below. The  
2218 DNNs are used only for separating events into signal and control regions in the 1  
2219 b-tag and 2 b-tag jets scenarios. The final results are extracted from the statistical  
2220 fitting to the mass of the  $\tau\tau$ ,  $m_{\tau\tau}$ .

## 2221 9.2 DNN-based event categorization

2222 Neural networks for event categorization are trained for each of the  $\mu\tau_h$ ,  $e\tau_h$ , and  $e\mu$   
2223 channels, for 1 and 2 b-tag jets, giving  $3 \times 2 = 6$  networks in total. In the training,  
2224 the signal is taken to be all of the possible pseudoscalar mass  $m_a$  hypotheses together.  
2225 The backgrounds for each DNN are taken to be a representative combination of the  
2226 three major backgrounds:  $Z \rightarrow \tau\tau$ ,  $t\bar{t} + \text{jets}$ , and fake backgrounds. The proportions of  
2227 each background for each channel and b-tag jet multiplicity are taken from the yields  
2228 in the  $m_{\tau\tau}$  distribution. For instance, in the  $\mu\tau_h$  1 b-tag jet category, the composition  
2229 of the background for training is 17.4% from  $Z \rightarrow \tau\tau$ , 42.4% from  $t\bar{t} + \text{jets}$ , and 40.2%  
2230 fakes.

2231 The input variables capture the key differences between the signal and the back-  
2232 ground:

- 2233 • Transverse momentum  $p_T$  of the electron and muon in the  $e\tau_h$  and  $\mu\tau_h$  channels,  
2234 where the signal tends to have a softer  $p_T$  spectrum (lower energy) than the  
2235 background.
- 2236 •  $p_T$  of the b-tag jet(s). The signal sample b-tag jet(s) tend to have softer  $p_T$ .
- 2237 • Invariant masses of the various objects ( $\tau\tau$  legs and the b-tag jet(s)), which  
2238 tend to be smaller for the signal samples.
- 2239 • The angular separation  $\Delta R$  between pairs of the objects, where signal samples  
2240 peak at smaller  $\Delta R$  values.

- 2241     • The transverse mass between the missing transverse energy  $p_T^{\text{miss}}$  and each of  
 2242       the four objects [84], defined as

$$m_T(\ell, p_T^{\text{miss}}) \equiv \sqrt{2p_T^\ell \cdot p_T^{\text{miss}}[1 - \cos(\Delta\phi)]} \quad (9.1)$$

2243       where  $p_T^\ell$  is the transverse momentum of the object  $\ell$ , and  $\Delta\phi$  is the difference  
 2244       in azimuthal angle between the object and the  $p_T^{\text{miss}}$ . Events from  $t\bar{t}$ +jets and  
 2245       jets faking  $\tau_h$  backgrounds have larger  $p_T^{\text{miss}}$  resulting in larger transverse mass  
 2246       values compared to the signal, which tends to have smaller  $p_T^{\text{miss}}$  that is also  
 2247       more aligned with the lepton legs.

- 2248     • The variable  $D_\zeta$  [84], defined as

$$D_\zeta \equiv p_\zeta - 0.85p_\zeta^{\text{vis}} \quad (9.2)$$

2249       where the  $\zeta$  axis is the bisector of the transverse directions of the visible  $\tau$  decay  
 2250       products.  $p_\zeta$  is the component of the  $p_T^{\text{miss}}$  along the  $\zeta$  axis, and  $p_\zeta^{\text{vis}}$  is the sum  
 2251       of the components of the lepton  $p_T$  along the same axis. This variable captures  
 2252       the fact that in signal the  $p_T^{\text{miss}}$  is small and approximately aligned with the  $\tau\tau$ .  
 2253       In contrast, the  $Z \rightarrow \tau\tau$  background tends towards large  $D_\zeta$  values because the  
 2254        $p_T^{\text{miss}}$  is collinear to the  $\tau\tau$ , and the  $t\bar{t}$ +jets events tend to have small  $D_\zeta$  due to  
 2255       a large  $p_T^{\text{miss}}$  not aligned with the  $\tau\tau$ .

- 2256     • For events with 2 b-tag jets, one additional variable is defined to capture the  
 2257       difference in the invariant mass of the  $bb$  and the  $\tau\tau$ :

$$\Delta m_{a_1} \equiv (m_{bb} - m_{\tau\tau})/m_{\tau\tau} \quad (9.3)$$

2258       This variable peaks at zero for the  $h \rightarrow aa \rightarrow 2b2\tau$  signal.

After training, events in data, MC, and embedded are evaluated with the six DNNs and assigned a raw score between 0 and 1 (background-like or signal-like). In order to flatten the distribution of the score and define score thresholds for categorizing events, the raw output scores are transformed with the function  $\tilde{p}(n) = \text{arctanh}(p \times \tanh(n))/n$  where  $n$  is a positive integer. The thresholds of the DNN score used for signal/control region definition are determined using scans that optimize the signal sensitivity and are shown in Tables 9.1 and 9.2.

1bNN $\tilde{p}(n = 1.5)$				
	SR1	SR2	SR3	CR
$\mu\tau_h$ 2018	$> 0.98$	$\in [0.95, 0.98]$	$\in [0.90, 0.95]$	$< 0.90$
$\mu\tau_h$ 2017	$> 0.97$	$\in [0.94, 0.97]$	$\in [0.90, 0.94]$	$< 0.90$
$\mu\tau_h$ 2016	$> 0.97$	$\in [0.94, 0.97]$	$\in [0.89, 0.94]$	$< 0.89$
1bNN $\tilde{p}(n = 1.5)$				
	SR1	SR2	SR3	CR
$e\tau_h$ 2018	$> 0.97$	$\in [0.945, 0.97]$	$\in [0.90, 0.945]$	$< 0.90$
$e\tau_h$ 2017	$> 0.985$	$\in [0.965, 0.985]$	$\in [0.93, 0.965]$	$< 0.93$
$e\tau_h$ 2016	$> 0.985$	$\in [0.965, 0.985]$	$\in [0.93, 0.965]$	$< 0.93$
1bNN $\tilde{p}(n = 2.5)$				
	SR1	SR2	SR3	CR
$e\mu$ 2018	$> 0.99$	$\in [0.95, 0.99]$	$\in [0.85, 0.95]$	$< 0.85$
$e\mu$ 2017	$> 0.985$	$\in [0.95, 0.985]$	$\in [0.85, 0.95]$	$< 0.85$
$e\mu$ 2016	$> 0.99$	$\in [0.95, 0.99]$	$\in [0.85, 0.95]$	$< 0.85$

Table 9.1: Event categorization based on DNN scores for events with exactly 1 b-tag jet (1bNN), for the three  $\tau\tau$  channels and three eras.

### 9.3 Methodology for signal extraction

After events are divided into categories, the data is compared to the expected backgrounds in the signal region categories. Here, we describe the fundamental concepts behind hypothesis testing in high-energy physics, as well as how exclusion limits can be set on parameters whose true values we cannot measure, culminating in the modified frequentist method  $CL_S$  which is used to perform signal extraction in this

	2bNN $\tilde{p}(n = 1.5)$		
	SR1	SR2	CR
$\mu\tau_h$ 2018	> 0.99	$\in [0.96, 0.99]$	< 0.96
$\mu\tau_h$ 2017	> 0.98	$\in [0.94, 0.98]$	< 0.94
$\mu\tau_h$ 2016	> 0.97	$\in [0.93, 0.97]$	< 0.93
	2bNN $\tilde{p}(n = 1.5)$		
	SR1	SR2	CR
$e\tau_h$ 2018	> 0.96	NA	< 0.96
$e\tau_h$ 2017	> 0.985	NA	< 0.985
$e\tau_h$ 2016	> 0.96	NA	< 0.96
	2bNN $\tilde{p}(n = 2.5)$		
	SR1	SR2	CR
$e\mu$ 2018	> 0.98	$\in [0.94, 0.98]$	< 0.94
$e\mu$ 2017	> 0.97	$\in [0.93, 0.97]$	< 0.93
$e\mu$ 2016	> 0.98	$\in [0.94, 0.98]$	< 0.94

Table 9.2: Event categorization based on DNN scores for events with 2 b-tag jets (2bNN), for the three  $\tau\tau$  channels and three eras.

2272 analysis.

### 2273 9.3.1 Model building and parameter estimation

In the frequentist interpretation of probability, an experiment measuring an observable can be repeated, resulting in different values of the observable, e.g. the invariant mass of a candidate Higgs boson in a search for the Higgs [100]. The ensemble of values of the observable  $x$  gives rise to the probability density function (PDF)  $f(x)$ , which has the important property that it is normalized to unity:

$$\int f(x) dx = 1.$$

A parametric family of PDFs

$$f(x|\alpha),$$

2274 read “ $f$  of  $x$  given  $\alpha$ ”, is referred to as a probability model or model. The parameters  $\alpha$   
 2275 typically represent parameters of the theory or an unknown property of the detector’s  
 2276 response. The parameters are not frequentist in nature, unlike  $x$ . Out of all the  
 2277 parameters, typically only a few are of interest, and are called the parameters of  
 2278 interest (POI), labeled  $\mu$  here. The remaining are referred to as nuisance parameters  
 2279 (NP) [100] and are labeled  $\theta$ .

2280  $f(x)$  is the probability density for the observable in one event and we wish to  
 2281 describe the probability density for a dataset with many events,  $\mathcal{D} = \{x_1, \dots, x_n\}$ ,  
 2282 called the total probability model  $\mathbf{f}$ . For instance, if we also have a prediction for  
 2283 the total number of events expected, called  $\nu$ , we also account for the overall Poisson  
 2284 probability for observing  $n$  events given  $\nu$  expected:

$$\mathbf{f}(\mathcal{D}|\nu, \alpha) = \text{Poisson}(n|\nu) \prod_{e=1}^n f(x_e|\alpha) \quad (9.4)$$

The likelihood function  $L(\alpha)$  is numerically equivalent to  $f(x|\alpha)$  for fixed  $x$ , or  
 $\mathbf{f}(\mathcal{D}|\alpha)$  with  $\mathcal{D}$  fixed [100]. The likelihood function is not a probability density for  $\alpha$   
 and is not normalized to unity:

$$\int L(\alpha) d(\alpha) \neq 1.$$

2285 i.e. the likelihood function is the value of  $f$  as a function of  $\alpha$  given a fixed value of  
 2286  $x$ .

2287 To estimate the parameter  $\alpha$  we use an estimator, which is a function of the  
 2288 data. Take for example the measurement of data distributed according to a Gaussian  
 2289 probability density  $f(x|\mu, \sigma) = \text{Gauss}(x|\mu, \sigma)$ . One possible estimator of the mean  $\mu$ ,  
 2290 is the mean of the measured data points  $\bar{x} = \sum_{i=1}^n x_i/n$  [100].

2291 A commonly used estimator in physics is the maximum likelihood estimator  
 2292 (MLE), defined as the value  $\alpha$  which maximizes the likelihood function  $L(\alpha)$ . This

2293 value, labeled  $\hat{\alpha}$ , also maximizes  $\ln L(\alpha)$  and minimizes  $-\ln L(\alpha)$ . By convention the  
2294  $-\ln L(\alpha)$  is minimized, in a process called “fitting”, and the maximum likelihood  
2295 estimate is called the “best fit value”.

2296 **9.3.2 Hypothesis testing**

2297 In this section we next introduce concepts related to hypothesis testing such as the  
2298 test statistic constructed from the ratio of likelihood functions.

2299 The objective of a likelihood analysis is to distinguish different models repre-  
2300 senting the various hypotheses, and determine the one that best explains the ex-  
2301 perimental outcome. In a search for new physics, a signal is additive on top of the  
2302 background. The background-only hypothesis is the null hypothesis, and the signal-  
2303 plus-background hypothesis is the alternative.

2304 As a simple example, take the  $p$ -value test, for an experiment where we count  
2305 events in the signal region,  $n_{SR}$ , and expect  $\nu_B$  background events and  $\nu_S$  events from  
2306 the signal [100]. Then

2307 1. The null hypothesis ( $H_0$ ), i.e. the background-only hypothesis in this experi-  
2308 ment, with the probability modeled by  $\text{Poisson}(n_{SR}|\nu_B)$ .

2309 2. The alternate hypothesis ( $H_1$ ), i.e. signal-plus-background hypothesis, with the  
2310 probability modeled by  $\text{Poisson}(n_{SR}|(\nu_B + \nu_S))$ .

2311 The compatibility of the observed data  $n_{SR}^0$  and the null hypothesis, is quantified as  
2312 the probability that the background-only hypothesis would produce at least as many  
2313 events as was observed. This probability is the  $p$ -value:

$$p = \sum_{n=n_{SR}^0}^{\infty} \text{Poisson}(n|\nu_B). \quad (9.5)$$

2314 If the  $p$ -value is very small, we might reject the null hypothesis. The  $p$ -value is not the

2315 probability of the null hypothesis given the data; rather, it expresses the probability  
 2316 that data with a certain property was obtained, assuming the null hypothesis [100].

2317 The *p*-value is an example of a test statistic  $T$ , which maps the data to a single  
 2318 real number. The Neyman-Pearson lemma states that out of the infinite possibilities  
 2319 of choices of test statistic, the uniformly most powerful test statistic is the likelihood  
 2320 ratio  $T_{NP}$  [100]:

$$T_{NP}(\mathcal{D}) = \frac{L(\mathcal{D}|H_1)}{L(\mathcal{D}|H_0)} \quad (9.6)$$

To reiterate, the test statistic  $T$  is a real-valued function of the data, implying that a particular probability model  $\mathbf{f}(\mathcal{D}|\boldsymbol{\alpha})$  implies a distribution of the test statistic,  $f(T|\boldsymbol{\alpha})$ , which depends on the value of  $\boldsymbol{\alpha}$ . With this distribution in hand, the *p*-value can be evaluated in the following equivalent formulations:

$$p(\boldsymbol{\alpha}) = \int_{T_0}^{\infty} f(T|\boldsymbol{\alpha}) dT \quad (9.7)$$

$$= \int \mathbf{f}(\mathcal{D}|\boldsymbol{\alpha}) \theta(T(\mathcal{D}) - T_0) d\mathcal{D} \quad (9.8)$$

$$= P(T \geq T_0|\boldsymbol{\alpha}) \quad (9.9)$$

2321 where  $T_0$  is the value of  $T$  based on the observed data, and  $\theta()$  is the Heaviside  
 2322 function. The size of the test is conventionally chosen to be 10%, 5%, or 1%. As  
 2323 the *p*-value depends on  $\boldsymbol{\alpha}$  (both the POI and NP), the null hypothesis should not be  
 2324 rejected if the *p*-value is larger than the size of the test for any value of the nuisance  
 2325 parameters.

### 2326 9.3.3 Confidence intervals

2327 In an example of the measurement of the Standard Model Higgs boson,  $\boldsymbol{\alpha}_{\text{POI}} =$   
 2328  $(\sigma/\sigma_{SM}, M_H)$ , with  $\sigma/\sigma_{SM}$  is the ratio of the production cross-section for Higgs with

respect to its value in the SM, and  $M_H$  is the unknown mass of the Higgs, values  
 of these parameters outside specific bounds are said to be “excluded at the 95%  
 confidence level”. These allowed regions are called confidence levels or confidence  
 regions, and the parameter values outside of them are considered excluded [100]. A  
 95% confidence interval does not mean that there is a 95% chance that the true value  
 of the parameter is inside the interval. Rather, a 95% confidence interval covers the  
 true value 95% of the time (even though we do not know the true value).

To construct a confidence interval for a parameter  $\alpha$ , the Neyman Construction  
 is used to invert a series of hypothesis tests; i.e. for each possible value of  $\alpha$ , the null  
 hypothesis is treated as  $\alpha$ , and we perform a hypothesis test based on a test statistic.  
 To construct a 95% confidence interval, we construct a series of hypothesis tests with  
 size of 5%. The confidence interval  $I(\mathcal{D})$  is constructed by taking the set of parameter  
 values  $\boldsymbol{\alpha}$  where the null hypothesis is accepted:

$$I(\mathcal{D}) = \{\boldsymbol{\alpha} | P(T(\mathcal{D}) > k_\alpha | \boldsymbol{\alpha}) < \alpha\}, \quad (9.10)$$

where  $T(\mathcal{D})$  is the test statistic, and the last  $\alpha$  (not bolded) and the subscript  $k_\alpha$   
 refer to the size of the test. A schematic of the Neyman construction is shown in Fig.  
 9.1. In a more generalized case, the  $x$ -axis is the test statistic  $T$ .

### 9.3.4 Profile likelihood ratio

In this section we describe a frequentist statistical procedure based on the profile  
 likelihood ratio test statistic, which is implemented using asymptotic distributions.

With a multi-parameter likelihood function  $L(\boldsymbol{\alpha})$ , the the maximum likelihood of  
 one specific parameter  $\alpha_p$  with other parameters  $\boldsymbol{\alpha}_o$  fixed, is called the conditional  
 maximum likelihood estimate and is denoted  $\hat{\alpha}_p(\boldsymbol{\alpha}_0)$ . The process of choosing specific  
 values of the nuisance parameters for a given value of  $\mu$ ,  $\mathcal{D}_{\text{simulated}}$ , and value of global

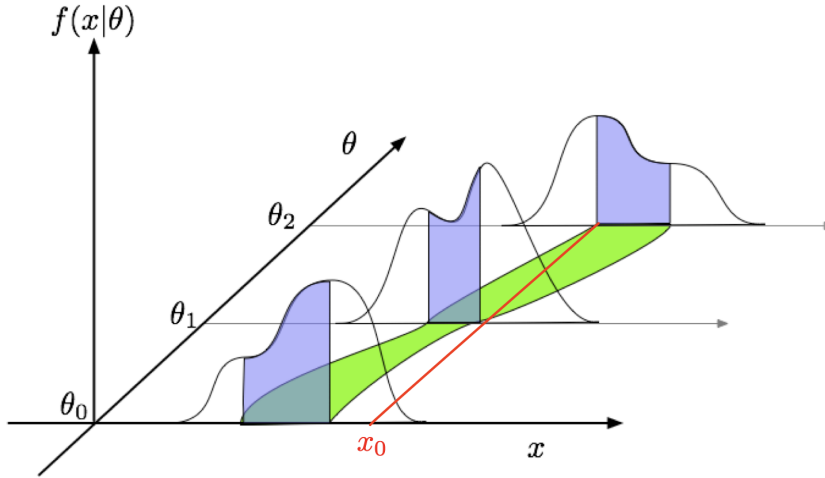


Figure 9.1: Schematic of the Neyman construction for confidence intervals [100]. For each value of  $\theta$ , we find a region in  $x$  where  $\int f(x|\theta)dx$  satisfies the size of the test (blue). These regions form a confidence belt (green). The intersection of the observation  $x_0$  (red) with the confidence belt defines the confidence interval  $[\theta_1, \theta_2]$  [100].

observables  $\mathcal{G}$  is called profiling. From the full list of parameters  $\boldsymbol{\alpha}$ , we denote the parameter of interest  $\mu$ , and the nuisance parameters  $\boldsymbol{\theta}$ .

We construct the profile likelihood ratio,

$$\lambda(\mu) = \frac{L(\mu, \hat{\boldsymbol{\theta}}(\mu))}{L(\mu, \hat{\boldsymbol{\theta}})} \quad (9.11)$$

which depends explicitly on the parameter of interest  $\mu$ , implicitly on the data  $\mathcal{D}_{\text{sim}}$  and global observables  $\mathcal{G}$ , and is independent of the nuisance parameters  $\boldsymbol{\theta}$ , which have been eliminated in profiling [100].

The main conceptual reason for constructing the test statistic from the profile likelihood ratio is that asymptotically (i.e. for measurements with many events) the distribution of the profile likelihood ratio  $\lambda(\mu = \mu_{\text{true}})$  is independent of the values of the nuisance parameters [100].

The following  $p$ -value is used to quantify the consistency with the hypothesis of a signal strength of  $\mu$ :

$$p_\mu = \int_{\tilde{q}_{\mu,\text{obs}}}^{\infty} f(\tilde{q}_\mu | \mu, \hat{\boldsymbol{\theta}}(\mu, \text{obs})) d\tilde{q}_\mu \quad (9.12)$$

2364 **9.3.5 Modified frequentist method:  $CL_S$**

2365 In the modified frequentist method called  $CL_S$ , to test a hypothesis with signal, we  
2366 define  $p'_\mu$  as a ratio of  $p$ -values [100]:

$$p'_\mu = \frac{p_\mu}{1 - p_b} \quad (9.13)$$

2367 where  $p_b$  is the  $p$ -value derived under the background-only hypothesis:

$$p_b = 1 - p_0 \equiv 1 - \int_{\tilde{q}_{\mu,\text{obs}}}^{\infty} f(\tilde{q}_\mu | 0, \hat{\theta}(\mu = 0, \text{obs})) d\tilde{q}_\mu. \quad (9.14)$$

2368 The  $CL_S$  upper limit on  $\mu$ , denoted  $\mu_{up}$ , is obtained by solving for  $p'_{\mu_{up}} = 5\%$ .  
2369 If testing the compatibility of the data with the background-only hypothesis, we  
2370 consider the  $p_b$  value defined above and conventionally convert it into the quantile  
2371 or “sigma” of a unit Gaussian.  $z$  standard deviations (e.g.  $z = 5$  in “ $5\sigma$ ”) means  
2372 that the probability of falling above these standard deviations, equals  $p_b$  (e.g.  $3\sigma$   
2373 corresponds to  $p_b = 2.7 \times 10^{-3}$  or 95.43%, and  $5\sigma$  corresponds to  $p_b = 5.7 \times 10^{-7}$  or  
2374 99.999943%).

2375 **Chapter 10**

2376 **Results**

2377 In this chapter, Section 10.1 presents the results from the  $h \rightarrow aa \rightarrow bb\tau\tau$  analysis  
2378 performed on  $137 \text{ fb}^{-1}$  of data from the full CMS Run-2 dataset in the years 2016 to  
2379 2018, with interpretations provided for different 2HDM+S scenarios. This analysis  
2380 was combined with a different search in the  $h \rightarrow aa \rightarrow bb\mu\mu$  final state, which was  
2381 also performed on the full Run-2 dataset. The combination procedure and results  
2382 from the combined analyses ( $h \rightarrow aa \rightarrow bb\ell\ell$ , with  $\ell = \mu, \tau$ ) are detailed in 10.2.  
2383 The combined analysis places some of the most stringent limits to date at CMS for  
2384 2HDM+S scenarios in the light scalar mass range  $m_a = 12 \text{ GeV}$  to  $60 \text{ GeV}$ .

2385 **10.1 Results from  $bb\tau\tau$**

2386 In each of the three  $\tau\tau$  channels studied ( $\mu\tau_h$ ,  $e\tau_h$ , and  $e\mu$ ), events are divided based  
2387 on whether they contain exactly 1 or 2 b-tag jets, and further divided into signal  
2388 and control regions (SRs and CRs) using the DNN categorization score as described  
2389 in Section 9.2. The control regions demonstrate good agreement between observed  
2390 events in data, and the sum of the contributions from expected backgrounds that  
2391 are modeled in simulated and embedded samples. The signal regions are defined to  
2392 be sensitive to the  $h \rightarrow aa \rightarrow bb\tau\tau$  signal. The postfit final observed and expected

2393 distributions of the di-tau invariant mass  $m_{\tau\tau}$  reconstructed with SVFit (described  
2394 in Section 5.2) are shown in Fig. 10.1 for the  $\mu\tau_h$  channel, Fig. 10.2 for the  $e\tau_h$   
2395 channel, and Fig. 10.3 for the  $e\mu$  channel. In all figures, the hypothesized yield for  
2396 the  $h \rightarrow aa \rightarrow bb\tau\tau$  signal is shown for the pseudoscalar mass  $m_a = 35$  GeV and  
2397 assuming a branching fraction  $B(H \rightarrow aa \rightarrow bb\tau\tau) = 10\%$ .

2398 The 95% CL expected and observed exclusion limits on the signal strength of the  
2399 branching fraction  $B(h \rightarrow aa \rightarrow bb\tau\tau)$  as a function of the pseudoscalar mass  $m_a$   
2400 ranging from 12 GeV to 60 GeV, are shown for the three  $\tau\tau$  channels and all three  
2401 channels combined in Fig. 10.4. The limits are shown as percentages and normalized  
2402 to the production cross-section of the Standard Model Higgs boson. No excess of  
2403 events above the Standard Model expectations is observed. In the limits for the three  
2404  $\tau\tau$  channels combined, expected (observed) limits range from 1.4 to 5.6% (1.7 to  
2405 7.6%) for pseudoscalar masses between 12 and 60 GeV.

2406 The  $e\mu$  channel is the only channel that has signal sensitivity to the  $m_a = 12$   
2407 GeV pseudoscalar mass hypothesis, because the minimum required spatial separation  
2408  $\Delta R = \sqrt{(\Delta\eta)^2 + (\Delta\phi)^2}$  between the two  $\tau$  legs is smaller than the other two channels  
2409 ( $\Delta R < 0.3$  for  $e\mu$ , compared to  $\Delta R < 0.4$  for the other two channels). This decreased  
2410  $\Delta R$  requirement results in better signal acceptance for low mass signals for the  $e\mu$   
2411 channel. The  $\mu\tau_h$  and  $e\tau_h$  channels are most sensitive to the intermediate mass points  
2412 studied, since the analysis targets a resolved signature: at low mass points, the tau  
2413 legs are boosted, and at high mass points, the  $m_{\tau\tau}$  distributions in signal have larger  
2414 overlap with background distributions. In the combination of the three  $\tau\tau$  channels,  
2415 the limit for  $m_a = 12$  GeV comes only from the  $e\mu$  channel, and the best sensitivity  
2416 is attained at intermediate mass points around  $m_a = 20$  GeV to 45 GeV.

2417 To set limits on the branching fraction of the 125 GeV Higgs to the two pseu-  
2418 doscalars,  $B(h \rightarrow aa)$ , we interpret the results in four types of 2HDM+S, which were  
2419 introduced in Section 1.4. In 2HDM+S, the theorized branching fraction of the pseu-

2420 doscalars depends on the 2HDM+S model type, the pseudoscalar mass  $m_a$ , and the  
2421 ratio of the two Higgs doublets' vacuum expectation values  $\tan \beta$ . In Type I models,  
2422 the branching fraction is independent of  $\tan \beta$ , while in Types II, III, and IV, it is  
2423 a function of  $m_a$  and  $\tan \beta$ . Limits for the  $bb\tau\tau$  final state as a function of  $m_a$  for  
2424 2HDM+S Type I (valid for all  $\tan \beta$  values), Type II with  $\tan \beta = 2.0$ , Type III with  
2425  $\tan \beta = 2.0$ , and Type IV with  $\tan \beta = 0.6$  are overlaid and shown in Fig. 10.5a.

## 2426 10.2 Combination with $bb\mu\mu$ final state

2427 Results from this analysis for the  $h \rightarrow aa \rightarrow bb\tau\tau$  final state are combined with the  
2428 analysis for the  $h \rightarrow aa \rightarrow bb\mu\mu$  final state [101]. While the predicted branching ratio  
2429 for  $aa \rightarrow bb\mu\mu$  is comparatively small, the  $bb\mu\mu$  final state has competitive results  
2430 due to the excellent di-muon resolution measured by CMS. The  $bb\mu\mu$  analysis uses  
2431 an unbinned fit to the data using the di-muon mass  $m_{\mu\mu}$  distribution. Details can be  
2432 found in [101].

2433 Combining the results is possible since the  $bb\tau\tau$  analysis explicitly rejects events  
2434 with extra leptons, so there is no overlap between the events studied in the  $bb\tau\tau$   
2435 analysis and the  $bb\mu\mu$  analysis. In the statistical combination, several systematic  
2436 uncertainties are treated as correlated: the integrated luminosity normalization, the  
2437 b-tagging scale factor, the scale factors related to muon reconstruction, identifica-  
2438 tion, and trigger efficiencies, the inefficiency in the ECAL trigger readout, and the  
2439 theoretical uncertainties related to signal modeling.

2440 Since the results in both final states are statistically limited, the combination ben-  
2441 efits from the additional data. For  $m_a = 35$  GeV, all systematic uncertainties amount  
2442 to around 6% of the total uncertainty, with the dominant systematic uncertainties  
2443 coming from jet energy systematics in the  $bb\mu\mu$  final state, theoretical uncertainties  
2444 in the signal, and uncertainties in the QCD multijet backgrounds in the  $e\mu$  channel

2445 of the  $bb\tau\tau$  final state.

2446 The mass distributions of the di-muon and di-tau objects ( $m_{\mu\mu}$  and  $m_{\tau\tau}$ ) are  
2447 compared to the data in a combined maximum likelihood fit to derive upper limits  
2448 on  $B(h \rightarrow aa)$ . The observed limits at 95% CL on  $B(h \rightarrow aa)$  for different 2HDM+S  
2449 scenarios, are shown for the search for  $h \rightarrow aa \rightarrow bb\mu\mu$  in Fig. 10.5b, and the  
2450 combined analyses  $h \rightarrow aa \rightarrow bb\ell\ell$  in Fig. 10.6.

2451 Exclusion limits in a two-dimensional plane as a function of  $\tan\beta$  and  $m_a$  are  
2452 set for 2HDM+S Types II, III, and IV in Fig. 10.7. The most stringent constraints  
2453 are observed for 2HDM+S type III because of large branching fractions predicted in  
2454 theory, with predicted branching fractions between 0.47 and 0.42 for  $\tan\beta = 2.0$  and  
2455 values of  $m_a$  between 15 and 60 GeV, compared to the observed 95% CL upper limits  
2456 which are between 0.08 and 0.03. For 2HDM+S type IV, the predicted branching  
2457 fractions from theory are between 0.26 and 0.20 for  $\tan\beta = 0.6$  for values of  $m_a$   
2458 between 15 and 60 GeV, and the 95% CL observed upper limits are between 0.12 and  
2459 0.05.

2460 The combined results from  $h \rightarrow aa \rightarrow bb\ell\ell$  are compared with CMS results in  
2461 other final states as a function of the pseudoscalar mass  $m_a$ : for 2HDM+S type I in  
2462 Fig. 10.8, type II with  $\tan\beta = 2.0$  in Fig. 10.9, and type III with  $\tan\beta = 2.0$  in Fig.  
2463 10.10. In other scenarios, e.g. type III with  $\tan\beta = 5.0$ , more stringent limits are set  
2464 by analyses in other final states,  $\mu\mu\tau\tau$  in this case. Other summary plots for other  
2465 model types and  $\tan\beta$  values can be found at [102].

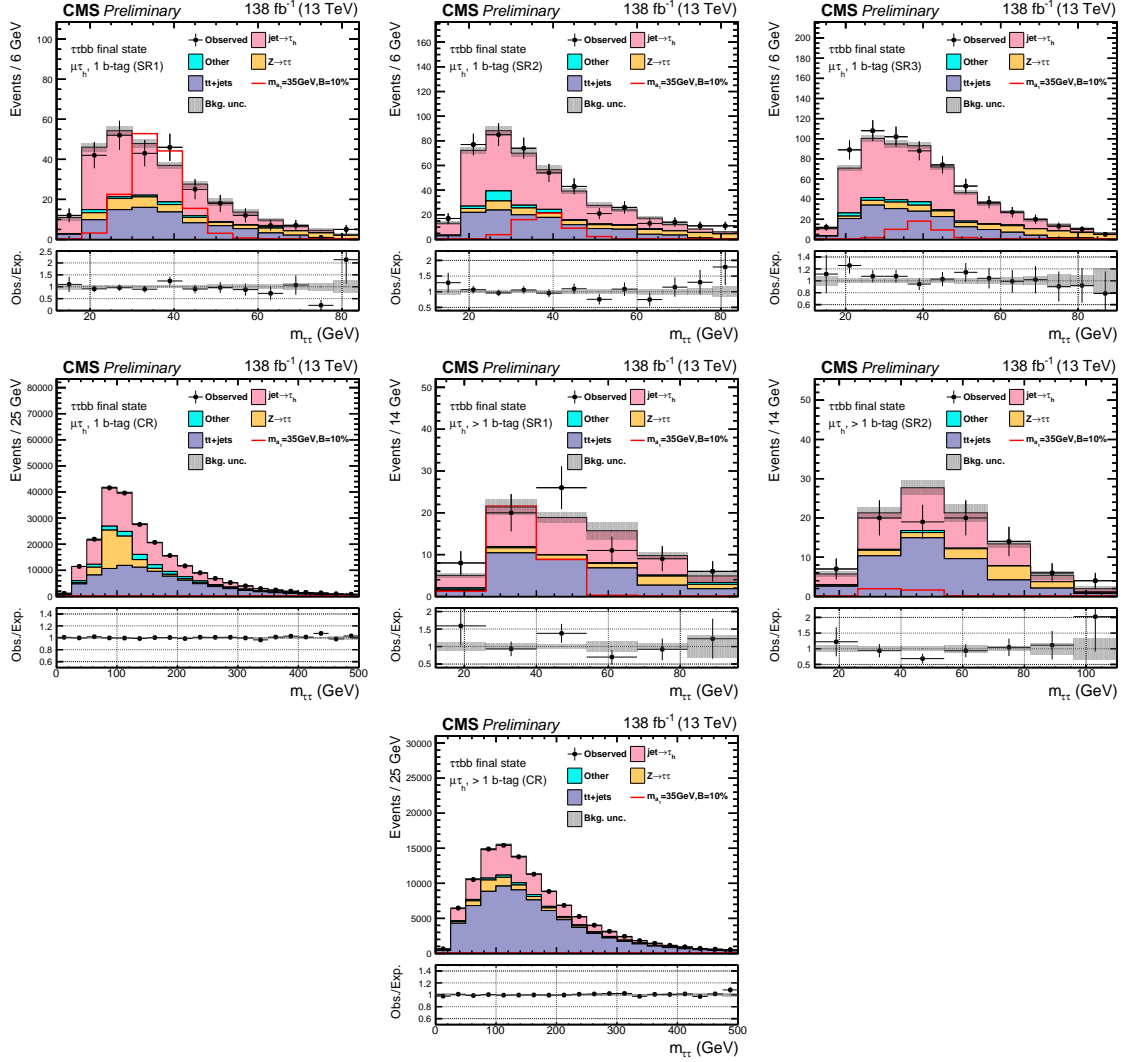


Figure 10.1: Postfit final  $m_{\tau\tau}$  observed and expected distributions, and the observed/expected ratios, in the  $\mu\tau_h$  channel [99]. Events are divided into the 1 b-tag jet signal regions (SR1, SR2, SR3) (*top row*), 1 b-tag jet control region (*middle row*), 2 b-tag jet signal regions (SR1, SR2) (*middle row*), and lastly the 2 b-tag jet control region (CR) (*bottom*). Statistical and systematic sources of uncertainties in the expected events are added in quadrature and labeled “Bkg. unc” (*shaded gray*). The dominant backgrounds in all categories are jets faking the  $\tau_h$  leg (*pink*),  $Z \rightarrow \tau\tau$  (*orange*), and  $t\bar{t}+j$ ets (*purple*). For illustrative purposes, the beyond-Standard Model signal yield from  $h \rightarrow aabb\tau\tau$  is shown for the pseudoscalar mass hypothesis  $m_a = 35$  GeV, assuming a branching fraction  $B(h \rightarrow aa \rightarrow bb\tau\tau) = 10\%$  (*red line*).

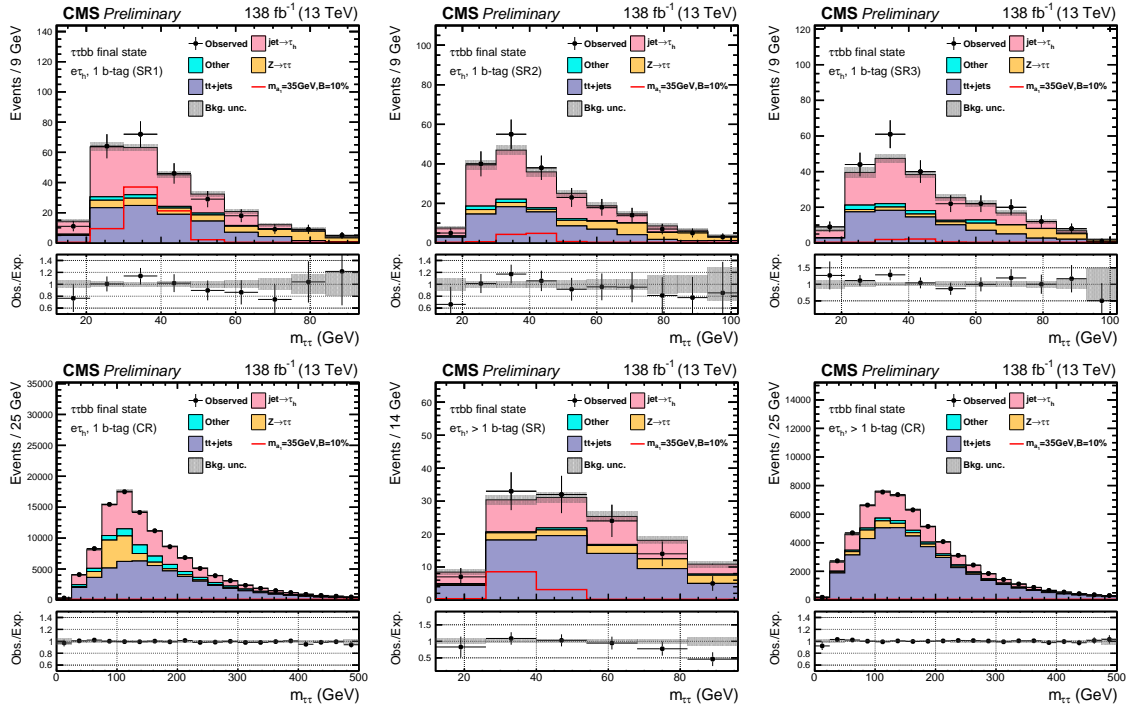


Figure 10.2: Postfit final observed and expected  $m_{\tau\tau}$  distributions, and the observed/expected ratios, in the  $e\tau_h$  channel [99]. Events are divided into the 1 b-tag jet signal regions (SR1, SR2, SR3) (*top row*), the 1 b-tag jet control region (CR) (*bottom row*), and 2 b-tag jet signal region (SR) and control region (CR) (*bottom row*). Statistical and systematic sources of uncertainties in the expected events are added in quadrature and labeled “Bkg. unc” (*shaded gray*). In this channel, the dominant backgrounds are jets faking the  $\tau_h$  leg (*pink*),  $Z \rightarrow \tau\tau$  (*orange*), and  $t\bar{t}+{\rm jets}$  (*purple*). For illustrative purposes, the beyond-Standard Model signal yield from  $h \rightarrow aabb\tau\tau$  is shown for the pseudoscalar mass hypothesis  $m_a = 35$  GeV, assuming a branching fraction  $B(h \rightarrow aa \rightarrow bb\tau\tau) = 10\%$  (*red line*).

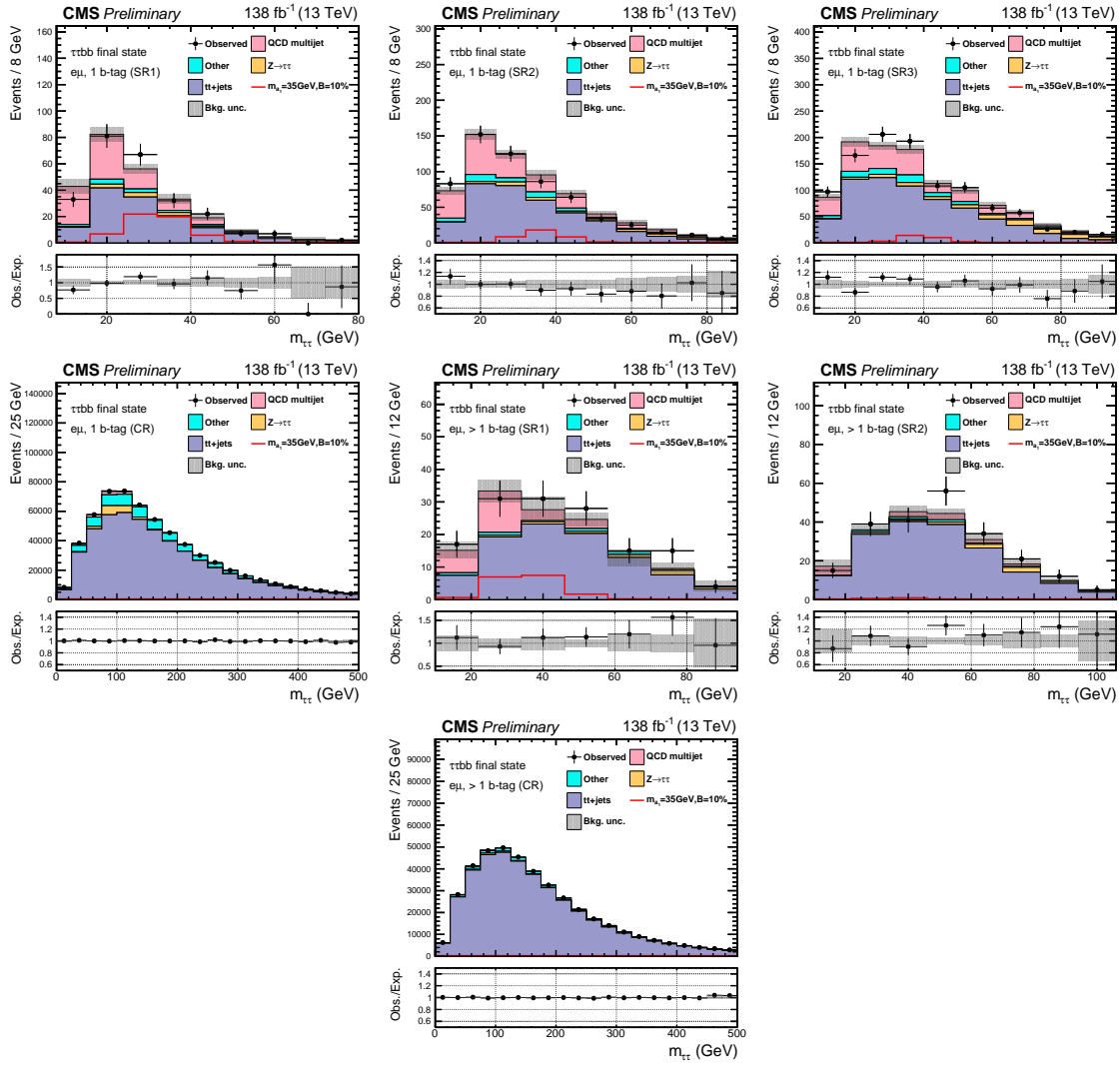


Figure 10.3: Postfit final observed and expected  $m_{\tau\tau}$  distributions, and the observed/expected ratios, in the  $e\mu$  channel [99]. Events are divided into the 1 b-tag jet signal regions (SR1, SR2, and SR3) (*top row*), 1 b-tag jet control region (CR) (*middle row*), 2 b-tag jet signal regions (SR1 and SR2) (*middle row*), and 2 b-tag jet control region (CR) (*bottom row*). Statistical and systematic sources of uncertainties in the expected events are added in quadrature and labeled “Bkg. unc” (*shaded gray*). The  $t\bar{t}+j$  process (*purple*) is a major background, and in the signal regions the QCD multijet (*pink*) is also a major background. For illustrative purposes, the beyond-Standard Model signal yield from  $h \rightarrow aabb\tau\tau$  is shown for the pseudoscalar mass hypothesis  $m_a = 35$  GeV, assuming a branching fraction  $B(h \rightarrow aa \rightarrow bb\tau\tau) = 10\%$  (*red line*).

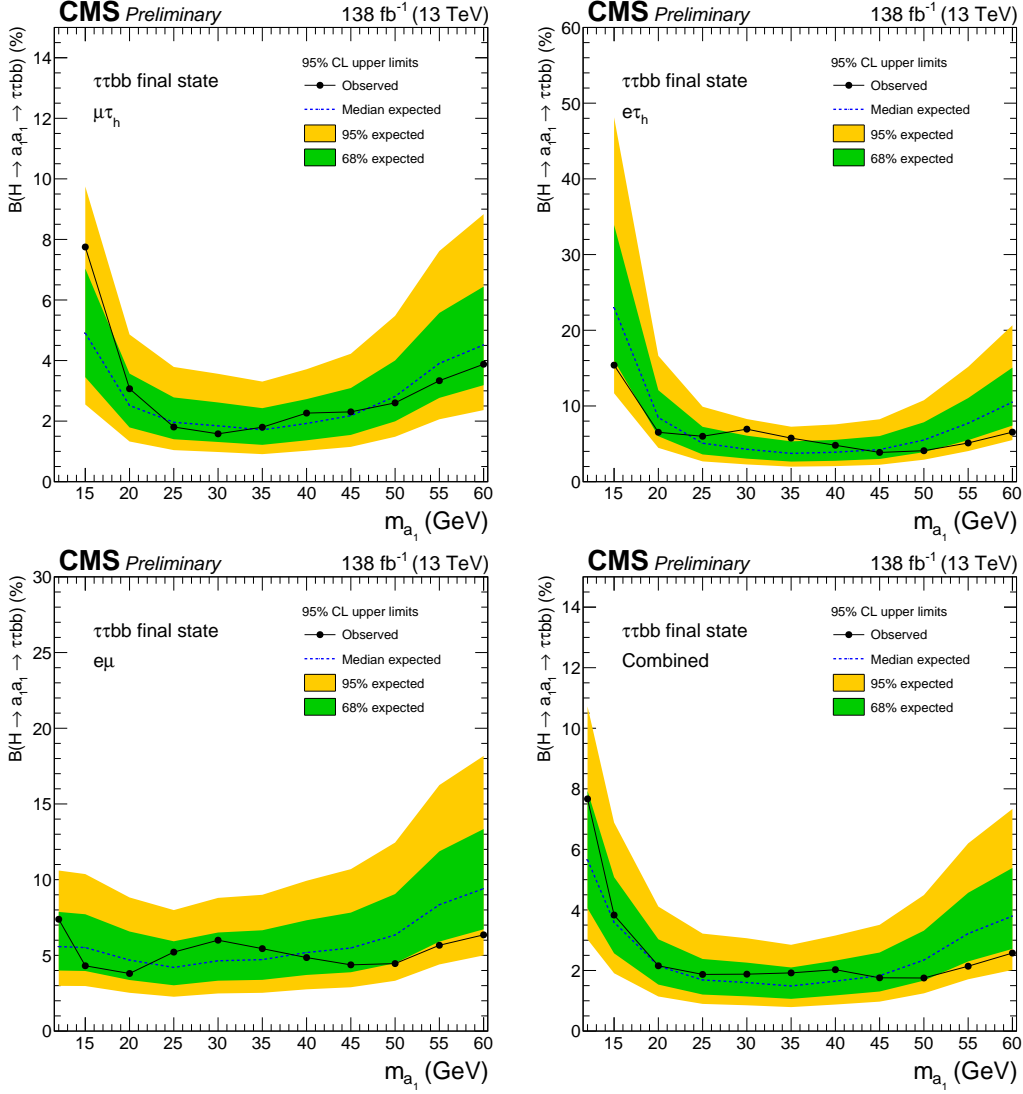
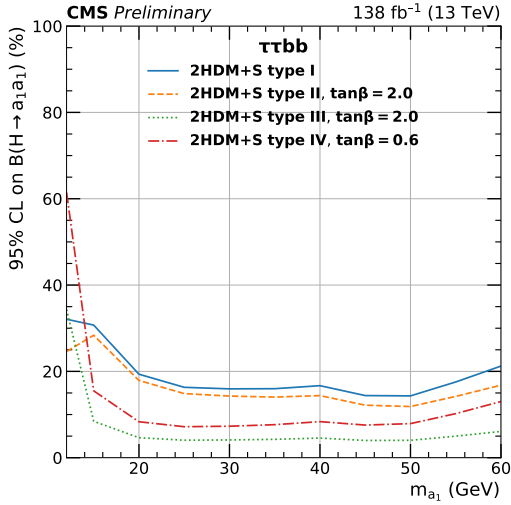
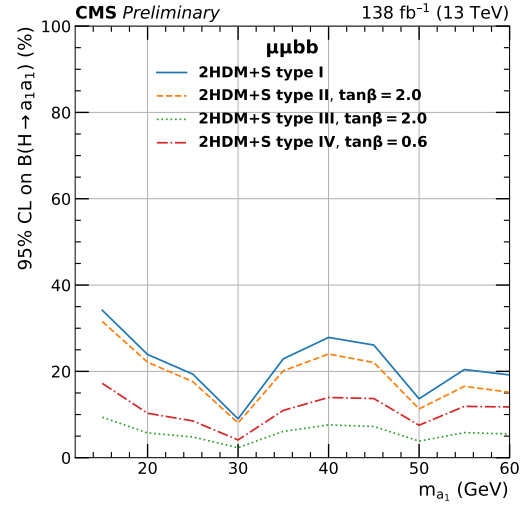


Figure 10.4: Observed 95% CL exclusion limits (*black, solid lines*) and expected 95% CL and 68% CL limits (*shaded yellow and green*) on the branching fraction  $B(h \rightarrow aa \rightarrow bb\tau\tau)$  in percentages, assuming the Standard Model production for the 125 GeV Higgs ( $h$ ). Limits are shown for the  $\mu\tau_h$  channel (*top left*), the  $e\tau_h$  channel (*top right*), and the  $e\mu$  channel (*bottom left*), and lastly the combination of all three channels (*bottom right*) [99]. The dataset corresponds to 138  $\text{fb}^{-1}$  of data collected in the years 2016-2018 at a center-of-mass energy 13 TeV. Only the  $e\mu$  channel has sensitivity to the mass hypothesis  $m_a = 12$  GeV. The best sensitivity is attained at intermediate mass points.



(a)  $bb\tau\tau$  final state.



(b)  $bb\mu\mu$  final state.

Figure 10.5: Observed 95% CL upper limits on  $B(h \rightarrow aa)$  in %, for the  $bb\tau\tau$  final state (*left*) and  $bb\mu\mu$  final state (*right*) using the full Run 2 integrated luminosity of  $138 \text{ fb}^{-1}$  in 2HDM+S type I (blue), type II with  $\tan\beta = 2.0$  (orange dashed), type III with  $\tan\beta = 2.0$  (dotted green), and type IV with  $\tan\beta = 0.6$  (red dashed) [99]. Linear interpolation is used between points in the graphs. The  $\tan\beta$  values chosen here correspond to the most stringent limits in each model.

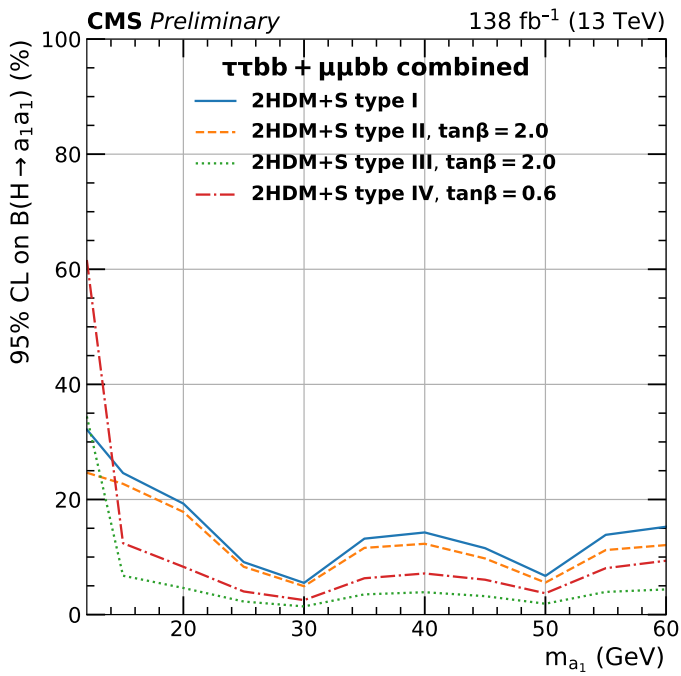


Figure 10.6: Observed 95% CL upper limits on the branching fraction of the 125 GeV Higgs boson to two pseudoscalars,  $B(h \rightarrow aa)$ , in percentages, as a function of the pseudoscalar mass  $m_a$ , in 2HDM+S type I (blue), type II with  $\tan\beta = 2.0$  (orange dashed), type III with  $\tan\beta = 2.0$  (dotted green), and type IV with  $\tan\beta = 0.6$  (red dashed), for the combination of  $bb\mu\mu$  and  $bb\tau\tau$  channels using the full Run 2 integrated luminosity of  $138 \text{ fb}^{-1}$  [99].

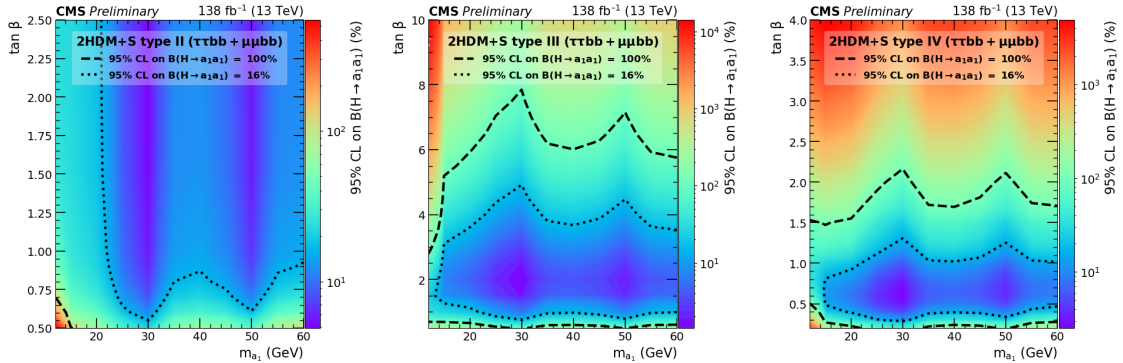


Figure 10.7: Observed 95% CL upper limits on  $\mathcal{B}(h \rightarrow aa)$  in %, for the combination of  $bb\mu\mu$  and  $bb\tau\tau$  channels using the full Run 2 integrated luminosity of  $138 \text{ fb}^{-1}$  for Type II (*left*), Type III (*middle*), and Type IV (*right*) 2HDM+S in the  $\tan \beta$  vs.  $m_a$  phase space. The contours (*dashed black*) correspond to branching fractions of 100% and 16%, where 16% is the combined upper limit on Higgs boson to undetected particle decays from previous Run-2 results. All points inside the contour are allowed within that upper limit. Linear extrapolation has been used between different points on the figures [99].

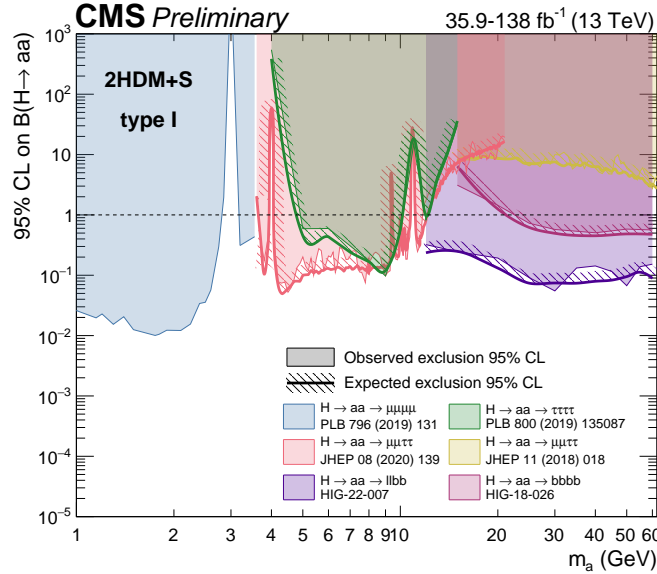


Figure 10.8: Summary plot of current 95% limits on the branching ratio of the 125 GeV Higgs boson to two pseudoscalars, normalized to the Standard Model Higgs production cross-section,  $\frac{\sigma(h)}{\sigma_{\text{SM}}} \times B(H \rightarrow aa)$  in the 2HDM+S type I scenario performed with data collected at 13 TeV [102]. Results from different final states studied at CMS are overlaid on this figure:  $\mu\mu\mu\mu$  (blue),  $\tau\tau\tau\tau$  (green), boosted  $2\mu 2\tau$  (red), resolved  $2\mu 2\tau$  (yellow),  $bbbb$  (magenta), and the combined result for  $\ell\ell bb$  ( $\ell = \mu, \tau$ ) (purple).

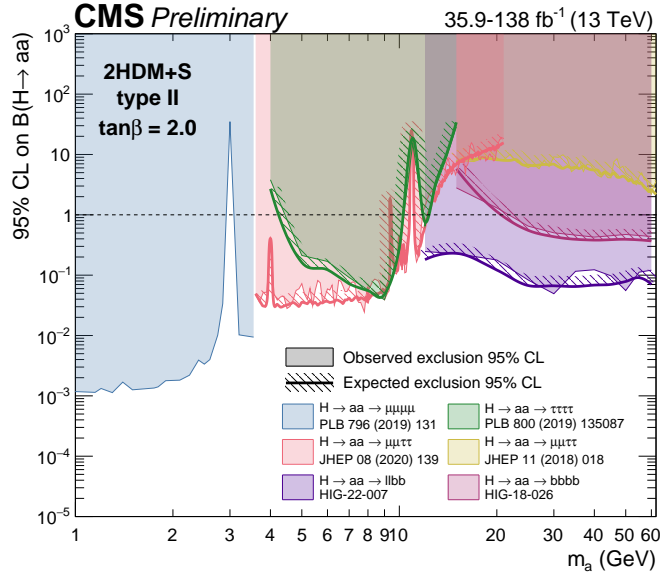


Figure 10.9: Summary plot of current observed and expected 95% CL limits on the branching ratio of the 125 GeV Higgs boson to two pseudoscalars, normalized to the Standard Model Higgs production cross-section,  $\frac{\sigma(h)}{\sigma_{SM}} \times B(h \rightarrow aa)$ , in the 2HDM+S type II scenario with  $\tan \beta = 2.0$ , obtained at CMS with data collected at 13 TeV [102]. Results from different final states studied at CMS are overlaid on this figure:  $\mu\mu\mu\mu$  (blue),  $\tau\tau\tau\tau$  (green), boosted  $2\mu 2\tau$  (red), resolved  $2\mu 2\tau$  (yellow),  $bbbb$  (magenta), and the combined result for  $\ell\ell bb$  ( $\ell = \mu, \tau$ ) (purple).

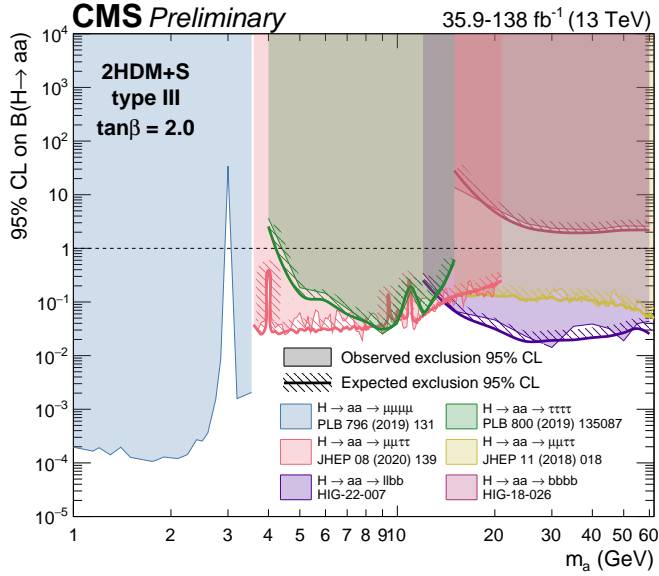


Figure 10.10: Summary plot of current observed and expected 95% CL limits on the branching ratio of the 125 GeV Higgs boson to two pseudoscalars, normalized to the Standard Model Higgs production cross section,  $\frac{\sigma(h)}{\sigma_{SM}} \times B(h \rightarrow aa)$  in the 2HDM+S type-III scenario with  $\tan \beta = 2.0$ , obtained at CMS with data collected at 13 TeV [102]. Results from different final states studied at CMS are overlaid on this figure:  $\mu\mu\mu\mu$  (blue),  $\tau\tau\tau\tau$  (green), boosted  $2\mu 2\tau$  (red), resolved  $2\mu 2\tau$  (yellow),  $bbbb$  (magenta), and the combined result for  $\ell\ell bb$  ( $\ell = \mu, \tau$ ) (purple).

2466 **Chapter 11**

2467 **Asymmetric exotic Higgs decays**

2468 This chapter presents progress towards a search for exotic Higgs decays to two light  
2469 scalars with unequal mass ( $h \rightarrow a_1 a_2$ ) final states with bottom quarks and  $\tau$  leptons,  
2470 with plans to interpret the results in the context of Two Real Singlet Models (TRSMs),  
2471 described in Section 1.5. Compared to the symmetric decay scenario  $h \rightarrow aa$  which  
2472 has been studied in multiple final states at CMS with stringent limits set on the  
2473 various 2HDM+S scenarios, this asymmetric decay scenario has not been directly  
2474 searched for at the CMS experiment. Section 11.1 lists the mass hypotheses of the  
2475 new particles  $a_1$  and  $a_2$  that will be studied. Section 11.2 describes the studies on  
2476 which channels the analysis will be carried out in. Section 11.3 shows the control  
2477 plots produced using the analysis framework that will be used for this analysis.

2478 **11.1 Signal masses**

2479 As discussed in Section 1.5,  $h \rightarrow a_1 a_2$  can result in a “cascade” decay if one of the  
2480 scalars,  $a_2$  is sufficiently heavy ( $m_{a_2} > 2m_{a_1}$ ). The “non-cascade” case is where the  
2481 light scalars decay directly to Standard Model particles.

2482 The mass hypotheses (mass points) ( $m_{a_1}, m_{a_2}$ ) studied here are:

- *Cascade mass points:* (15, 30), (15, 40), (15, 50), (15, 60), (15, 70), (15, 80), (15, 90), (15, 100), (15, 110), (20, 40), (20, 50), (20, 60), (20, 70), (20, 80), (20, 90), (20, 100), (30, 60), (30, 70), (30, 80), and (30, 90) GeV
- *Non-cascade mass points:* (15, 20), (15, 30), (20, 30), (20, 40), (30, 40), (30, 50), (30, 60), (40, 50), (40, 60), (40, 70), (40, 80), (50, 60), and (50, 70) GeV

Samples were produced using the MadGraph5\_aMCatNLO event generator, for each signal mass point in the gluon-gluon fusion (ggF) and vector boson fusion (VBF) production modes of the 125 GeV Higgs boson. In the sample generation, the decays of  $a$  to Standard Model particles were specified to be decays to bottom quarks or  $\tau$  leptons.

## 11.2 Cascade scenario signal studies

Studies of the signal phenomenology in the cascade scenario were performed to determine the viability of the  $4b2\tau$  and/or  $2b4\tau$  channels.

Cross sections and branching fractions of the  $4b2\tau$  and  $2b4\tau$  final states were compared using cross-section predictions provided by the authors of [7]. For an example mass point  $m_{a_2} = 80$  GeV,  $m_{a_1} = 30$  GeV, the branching fractions to  $4b2\tau$  is ten times larger than  $2b4\tau$ :  $B(h \rightarrow a_1 a_2 \rightarrow 3a_1 \rightarrow 4b2\tau) = 0.00857$ , vs.  $B(h \rightarrow a_1 a_2 \rightarrow 3a_1 \rightarrow 2b4\tau) = 0.00068$ . The  $4b2\tau$  final state is chosen for this analysis.

In general the four b-flavor jets have low  $p_T$  at generator level, as illustrated for example mass points (100, 15) GeV and (40, 20) GeV in Fig. 11.1. The  $p_T$  distribution of the sub-leading jet peaks at an energy below 20 GeV, with the third and fourth jets tending to have even softer energies.

An event category with three or more b-tag jets was determined to be infeasible due to low statistics in this category, due to the difficulties in reconstructing the third

2508 and fourth b-flavor jets which have very low transverse momenta  $p_T$ . Event categories  
 2509 with exactly 1 b-tag jet and  $\geq 2$  b-tag jets will be used.

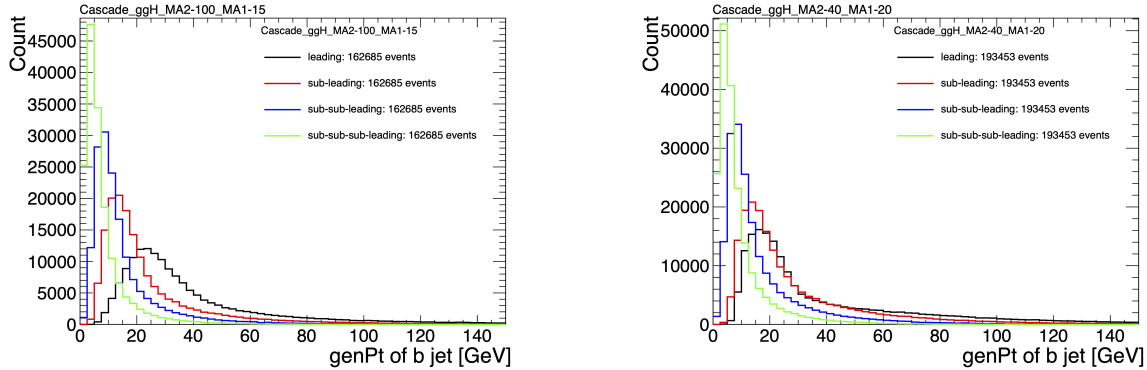


Figure 11.1: Generator-level b-flavor jet transverse momenta  $p_T$ , for  $h \rightarrow a_1 a_2$  cascade scenario in the  $4b2\tau$  final state, for mass hypotheses  $(m_{a_1}, m_{a_2}) = (100, 15)$  GeV (*left*) and  $(40, 20)$  GeV (*right*). In each plot the generator-level  $p_T$  of the leading (*black*), sub-leading (*red*), third (*blue*), and fourth (*light green*) are overlaid.

2510 In the  $4b2\tau$  final state, the possibility of the leading and sub-leading b-tag jets  
 2511 being sufficiently close in  $\Delta R$  to require boosted jet reconstruction techniques was  
 2512 explored. In the  $4b2\tau$  case, the two b-flavor-jets in the generated event that were  
 2513 spatially closest in  $\Delta R$  were considered as one object. This two b-flavor jet object was  
 2514 spatially matched in  $\Delta R$  to the jets reconstructed with the standard AK4 algorithm  
 2515 which uses a cone size of  $\Delta R = 0.4$ . The quality of the  $p_T$  resolution (computed as  
 2516  $(p_{T,\text{reconstructed}} - p_{T,\text{gen}})/p_{T,\text{gen}}$ ) and closeness in distance  $\Delta R$  of the reconstructed jet  
 2517 to the nearest generator-level jets, was seen to depend on the absolute and relative  
 2518 masses of the light scalars. The best (worst) performance occurred in samples with  
 2519 large (small) mass differences between the heavier scalar  $a_2$  and the lighter scalar  $a_1$ ,  
 2520 as illustrated for the mass hypotheses  $(m_{a_1}, m_{a_2})$  (100, 15) GeV and (40, 20) GeV in  
 2521 Fig. 11.2.

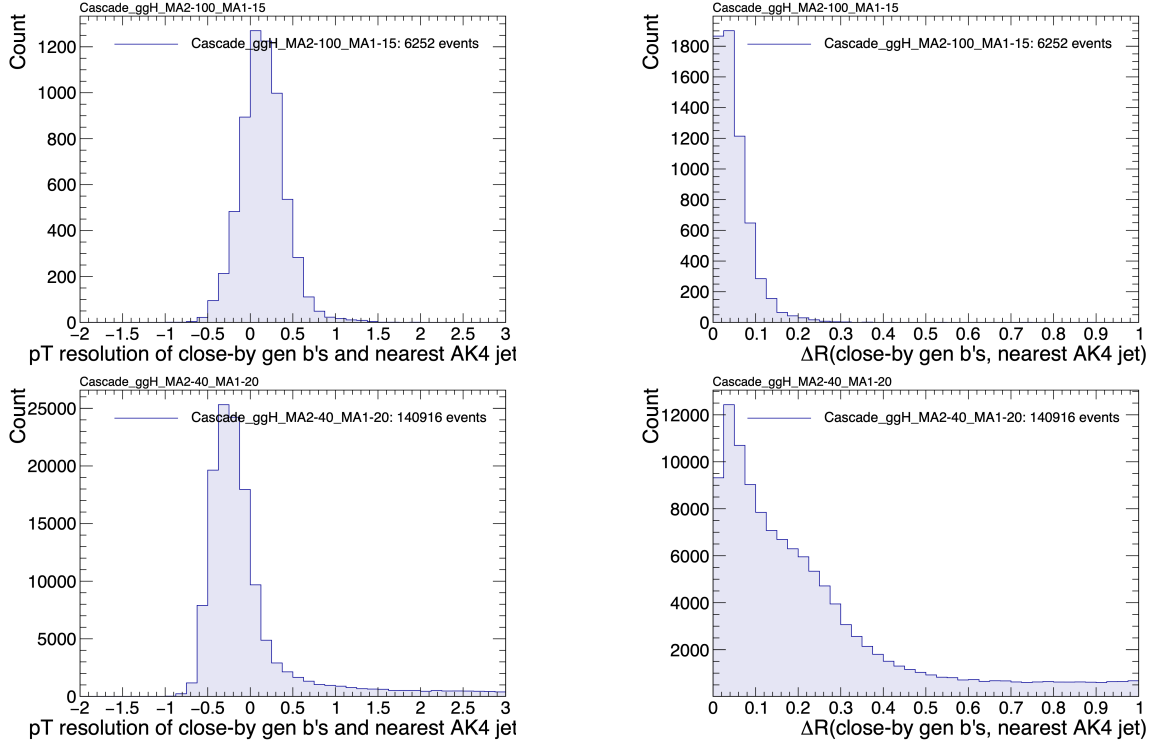


Figure 11.2: Distributions (arbitrary units) of transverse momentum  $p_T$  resolution and  $\Delta R$  between the two closest generator-level  $b$  jets, treated as one object, and the nearest reconstructed AK4 jet, for two different  $h \rightarrow a_1 a_2$  mass hypotheses ( $m_{a_1}, m_{a_2}$ ) = (100, 15) GeV (top left, top right) and (40, 20) GeV (bottom left, bottom right) in the ggH production of the 125 GeV  $h$ . In the (40, 20) GeV mass point, the longer  $p_T$  resolution tail (bottom left) indicates that the reconstructed jet underestimates the generator  $b$ -flavor jets' energy, and the significant fraction of events with larger  $\Delta R$  values (bottom right) indicate worse matching.

### 11.3 Current control plots for $\mu\tau_h$ channel

The  $\tau\tau$  states for the  $h \rightarrow a_1 a_2$  to  $4b2\tau$  analysis will be similar to those studied in  $h \rightarrow aa \rightarrow bb\tau\tau$ . For the  $\mu\tau_h$  channel, histograms of the key kinematic variables are made for data and the sum of the expected backgrounds, which are estimated from Monte Carlo samples, embedded samples, and the data-driven method for estimating jets faking  $\tau_h$  as described in Chapter 7. Nominal values of the scale factors and event reweighting are applied, as described in Chapter ???. The errors shown in the figures only include statistical errors and only several of the full set of systematic errors (only those associated with the lepton energy scales and  $\tau_h$  identification efficiency,

2531 described in Sections 5.3.1, 5.3.2, and 5.3.4).

2532 The  $p_T$ ,  $\eta$ , and  $\phi$  of the leading muon and hadronic tau  $\tau_h$ , and the di-tau visible  
2533 mass  $m_{\text{vis}}$  and momentum  $p_{T,\text{vis}}$ , are shown in Fig. 11.3. The  $p_T$ ,  $\eta$ , and  $\phi$  of the the  
2534 leading and sub-leading b-tag jets, and the missing transverse energy magnitude and  
2535 azimuthal direction, are shown in Fig. 11.4.

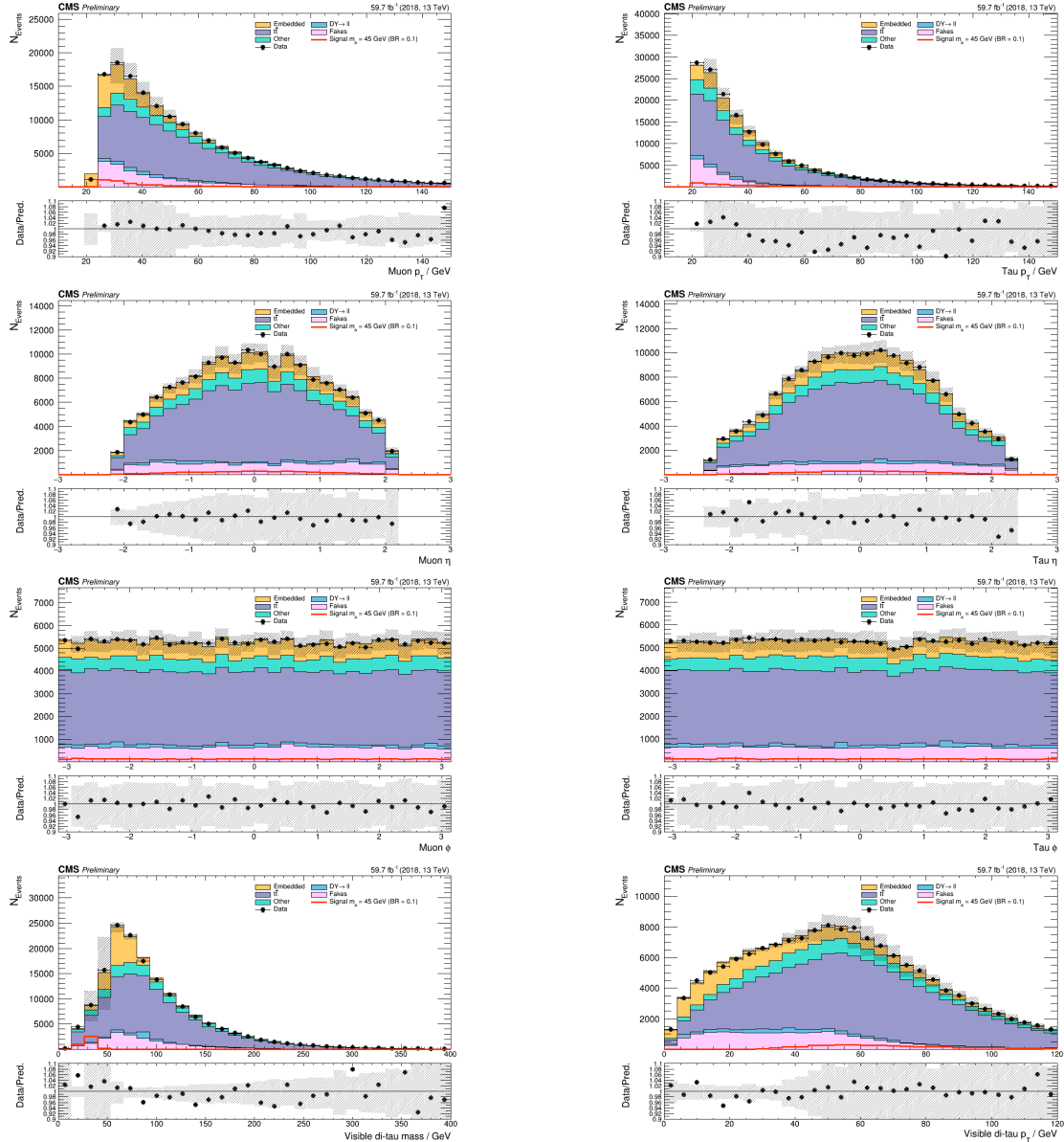


Figure 11.3: Kinematic properties of the leading muon and  $\tau_h$  in the  $\mu\tau_h$  channel:  $p_T$  (top row),  $\eta$  (second row), and  $\phi$  (third row). The visible 4-momenta of the muon and  $\tau_h$  are summed, giving the visible di-tau mass  $m_{\text{vis}}$  and transverse momentum  $p_{T,\text{vis}}$ . The errors shown in the figures only include statistical errors and only several of the full set of systematic errors (only those associated with the lepton energy scales and  $\tau_h$  identification efficiency).

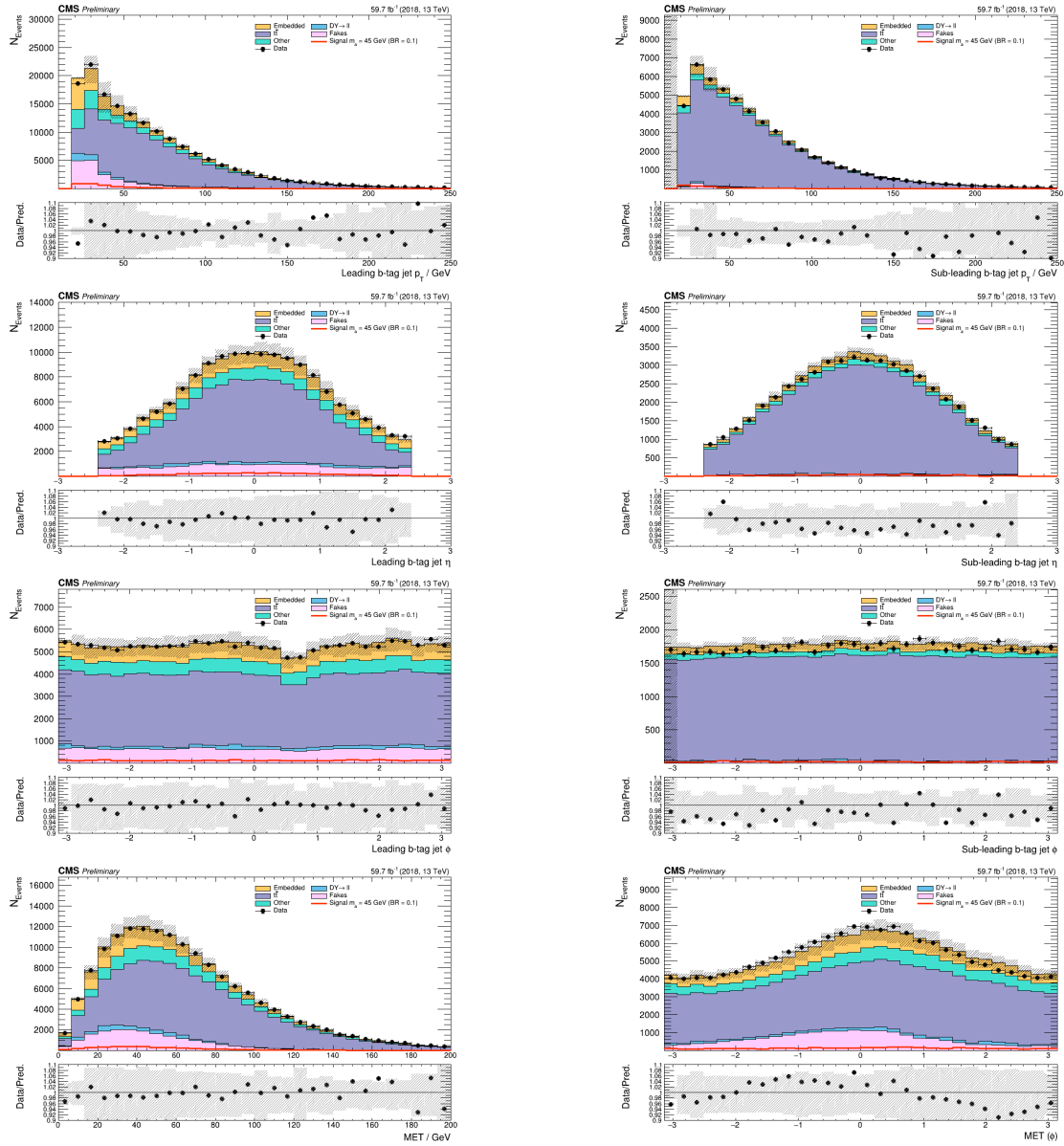


Figure 11.4: Kinematic properties of the leading and sub-leading b-tag jets in the  $\mu\tau_h$  final state: jet  $p_T$  (*top row*),  $\eta$  (*second row*),  $\phi$  (*third row*), as well as the missing transverse energy magnitude and azimuthal direction (*bottom row*). The errors shown in the figures only include statistical errors and only several of the full set of systematic errors (only those associated with the lepton energy scales and  $\tau_h$  identification efficiency).

2536

# Chapter 12

2537

## Conclusion and outlook

2538 With the discovery of a Higgs boson with mass 125 GeV at the LHC in 2012, the LHC  
2539 and CMS physics program has evolved to include the precise characterization of the  
2540 125 GeV Higgs boson and searching for evidence of additional Higgs particles in an  
2541 extended Higgs sector. This thesis presents a direct search at CMS for exotic decays  
2542 of the Higgs boson with mass 125 GeV in data collected in the years 2016-2018 in  
2543 proton-proton collisions at center-of-mass energy 13 TeV, to two light neutral scalar  
2544 particles that decay to two bottom quarks and two tau leptons ( $h \rightarrow aa \rightarrow bb\tau\tau$ ). The  
2545 results are combined with another search that was performed in the  $h \rightarrow aa \rightarrow bb\mu\mu$   
2546 final state, giving the most stringent limits to date for theories with Two Higgs  
2547 Doublet Models extended with a singlet scalar (2HDM+S), for pseudoscalar masses  
2548  $m_a$  ranging from 15 GeV to 60 GeV, in a number of 2HDM+S scenarios such as type  
2549 II and III with  $\tan\beta = 2.0$ .

2550 As the rich physics program of CMS has set stringent limits on the exotic decay  
2551  $h \rightarrow aa$ , we turn our attention to direct searches for decays to light neutral scalars  
2552 with potentially unequal mass,  $h \rightarrow a_1a_2$ , which has not been performed at CMS  
2553 to date. Preliminary studies on  $h \rightarrow a_1a_2$  signals in the Two Real Singlet Model  
2554 (TRSM) are shown, and work is ongoing to develop the analysis for  $h \rightarrow a_1a_2$  in final

2555 states with bottom quarks and tau leptons.

2556 To ensure the continued performance of the CMS detector and to enhance its  
2557 data-taking capabilities in the intense pile-up conditions of the Phase-2 upgrade of  
2558 the High-Luminosity LHC, upgrades of the Level-1 Trigger are paramount for filtering  
2559 the increased data rate of the HL-LHC. This thesis presents work on the standalone  
2560 barrel calorimeter algorithm for reconstructing and identifying electron and photon  
2561 candidates, using high granularity crystal-level information from the ECAL subdetec-  
2562 tor. For Phase-2, the increase in the granularity of information sent from the electro-  
2563 magnetic calorimeter to the Level-1 trigger, from energy sums over towers (which are  
2564  $5 \times 5$  in crystals) to crystal-level information, allows for the implementation of a more  
2565 sophisticated clustering algorithm that can exploit the fact that genuine electrons  
2566 and photons tend to leave energies concentrated a  $3 \times 5$  window in crystals, and use  
2567 shape and isolation information to distinguish genuine electrons and photons from  
2568 noise. Electrons and photons are key to characterizing Standard Model processes and  
2569 performing searches for new physics, and this represents one of the many upgrades of  
2570 the CMS detector in preparation for Phase-2. With the ongoing Run-3 data collecting  
2571 period, and wealth of ongoing and scheduled upgrades, there remains an abundance  
2572 of directions for detector development and physics at CMS heading into Phase-2 of  
2573 the LHC.

# <sup>2574</sup> Appendix A

## <sup>2575</sup> Samples used

<sup>2576</sup> The datasets used in the MiniAOD-based framework for the  $h \rightarrow aa \rightarrow bb\tau\tau$  analysis  
<sup>2577</sup> are listed in this appendix. The NanoAOD-based framework uses the NanoAOD ver-  
<sup>2578</sup> sions of these datasets. The data used for the years 2016-2018 are listed in Tables A.1,  
<sup>2579</sup> A.2, and A.3 respectively. The embedded samples used for the years 2016-2018 are  
<sup>2580</sup> listed in Tables A.4, A.5, and A.6 respectively. The Monte Carlo simulated samples  
<sup>2581</sup> used to estimate backgrounds for the years 2016-2018 are listed in Tables A.7, A.8,  
<sup>2582</sup> and A.9 respectively.

<sup>2583</sup> The  $h \rightarrow aa \rightarrow bb\tau\tau$  signal samples are generated for 11 psuedoscalar masses  
<sup>2584</sup> between 12 GeV and 60 GeV for gluon fusion (ggF) and vector boson fusion (VBF)  
<sup>2585</sup> Higgs production. The 2016-2018 signal samples are listed in Tables A.10, A.11 and  
<sup>2586</sup> A.12 respectively. A filter is applied at the generator level for each  $\tau\tau$  final state:

- <sup>2587</sup> •  $ee$  final state:  $p_T(e_1) > 22$  GeV,  $p_T e_2 > 10$  GeV,  $|\eta(e_1)| < 2.6$ , and  $|\eta(e_2)| < 2.6$ .
- <sup>2588</sup> •  $e\tau_h$  final state:  $p_T(e) > 22$  GeV,  $p_T(\tau_h) > 16$  GeV,  $|\eta(e)| < 2.6$ , and  $|\eta(\tau_h)| < 2.7$ .
- <sup>2589</sup> •  $e\mu$  final state:  $p_T(e) > 11$  GeV,  $p_T(\mu) > 7$  GeV,  $|\eta(e)| < 2.6$ , and  $|\eta(\mu)| < 2.5$ .
- <sup>2590</sup> •  $\tau_h\tau_h$  final state:  $p_T(\tau_{h1}) > 28$  GeV,  $p_T(\tau_{h2}) > 28$  GeV,  $|\eta(\tau_{h1})| < 2.5$ , and  
<sup>2591</sup>  $|\eta(\tau_{h2})| < 2.5$ .

- 2592      •  $\mu\tau_h$  final state:  $p_T(\mu) > 19 \text{ GeV}$ ,  $p_T(\tau_h) > 16 \text{ GeV}$ ,  $|\eta(\mu)| < 2.5$ , and  $|\eta(\tau_h)| <$   
 2593      2.7.

- 2594      •  $\mu\mu$  final state:  $p_T(\mu_1) > 17 \text{ GeV}$ ,  $p_T(\mu_2) > 8 \text{ GeV}$ ,  $|\eta(\mu_1)| < 2.5$ , and  $|\eta(\mu_2)| <$   
 2595      2.5.

2596      The tables also show for each sample the filter efficiencies, which is the percentage  
 2597      of events that pass the above filters, and the number of events that were generated  
 2598      after applying the filters.

Channel	Data sets (2016)	Run range
$e\mu$	/MuonEG/Run2016B-17Jul2018_ver1-v1/MINIAOD	272760-273017
	/MuonEG/Run2016B-17Jul2018_ver2-v1/MINIAOD	273150-275376
	/MuonEG/Run2016C-17Jul2018-v1/MINIAOD	275656-276283
	/MuonEG/Run2016D-17Jul2018-v1/MINIAOD	276315-276811
	/MuonEG/Run2016E-17Jul2018-v2/MINIAOD	276831-277420
	/MuonEG/Run2016F-17Jul2018-v1/MINIAOD	277932-278808
	/MuonEG/Run2016G-17Jul2018-v1/MINIAOD	278820-280385
	/MuonEG/Run2016H-17Jul2018-v1/MINIAOD	281613-284044
$e\tau_h$	/SingleElectron/Run2016B-17Jul2018_ver1-v1/MINIAOD	272760-273017
	/SingleElectron/Run2016B-17Jul2018_ver2-v1/MINIAOD	273150-275376
	/SingleElectron/Run2016C-17Jul2018-v1/MINIAOD	275656-276283
	/SingleElectron/Run2016D-17Jul2018-v1/MINIAOD	276315-276811
	/SingleElectron/Run2016E-17Jul2018-v1/MINIAOD	276831-277420
	/SingleElectron/Run2016F-17Jul2018-v1/MINIAOD	277932-278808
	/SingleElectron/Run2016G-17Jul2018-v1/MINIAOD	278820-280385
	/SingleElectron/Run2016H-17Jul2018-v1/MINIAOD	281613-284044
$\mu\tau_h$	/SingleMuon/Run2016B-17Jul2018_ver1-v1/MINIAOD	272760-273017
	/SingleMuon/Run2016B-17Jul2018_ver2-v1/MINIAOD	273150-275376
	/SingleMuon/Run2016C-17Jul2018-v1/MINIAOD	275656-276283
	/SingleMuon/Run2016D-17Jul2018-v1/MINIAOD	276315-276811
	/SingleMuon/Run2016E-17Jul2018-v1/MINIAOD	276831-277420
	/SingleMuon/Run2016F-17Jul2018-v1/MINIAOD	277932-278808
	/SingleMuon/Run2016G-17Jul2018-v1/MINIAOD	278820-280385
	/SingleMuon/Run2016H-17Jul2018-v1/MINIAOD	281613-284044

Table A.1: Data sets used in the  $h \rightarrow aa \rightarrow bb\tau\tau$  analysis for the 2016 era.

Channel	Data sets (2017)	Run range
$e\mu$	/MuonEG/Run2017B-31Mar2018-v1/MINIAOD	297047-299329
	/MuonEG/Run2017C-31Mar2018-v1/MINIAOD	299368-302029
	/MuonEG/Run2017D-31Mar2018-v1/MINIAOD	302031-302663
	/MuonEG/Run2017E-31Mar2018-v1/MINIAOD	303824-304797
	/MuonEG/Run2017F-31Mar2018-v1/MINIAOD	305040-306460
$e\tau_h$	/SingleElectron/Run2017B-31Mar2018-v1/MINIAOD	297047-299329
	/SingleElectron/Run2017C-31Mar2018-v1/MINIAOD	299368-302029
	/SingleElectron/Run2017D-31Mar2018-v1/MINIAOD	302031-302663
	/SingleElectron/Run2017E-31Mar2018-v1/MINIAOD	303824-304797
	/SingleElectron/Run2017F-31Mar2018-v1/MINIAOD	305040-306460
$\mu\tau_h$	/SingleMuon/Run2017B-31Mar2018-v1/MINIAOD	297047-299329
	/SingleMuon/Run2017C-31Mar2018-v1/MINIAOD	299368-302029
	/SingleMuon/Run2017D-31Mar2018-v1/MINIAOD	302031-302663
	/SingleMuon/Run2017E-31Mar2018-v1/MINIAOD	303824-304797
	/SingleMuon/Run2017F-31Mar2018-v1/MINIAOD	305040-306460

Table A.2: Data sets used in the  $h \rightarrow aa \rightarrow bb\tau\tau$  analysis for the 2017 era.

Channel	Data sets (2018)	Run range
$e\mu$	/MuonEG/Run2018A-17Sep2018-v1/MINIAOD	315257-316995
	/MuonEG/Run2018B-17Sep2018-v1/MINIAOD	317080-319310
	/MuonEG/Run2018C-17Sep2018-v1/MINIAOD	319337-320065
	/MuonEG/Run2018D-PromptReco-v2/MINIAOD	320500-325175
$e\tau_h$	/EGamma/Run2018A-17Sep2018-v2/MINIAOD	315257-316995
	/EGamma/Run2018B-17Sep2018-v1/MINIAOD	317080-319310
	/EGamma/Run2018C-17Sep2018-v1/MINIAOD	319337-320065
	/EGamma/Run2018D-PromptReco-v2/MINIAOD	320497-325175
$\mu\tau_h$	/SingleMuon/Run2018A-17Sep2018-v2/MINIAOD	315257-316995
	/SingleMuon/Run2018B-17Sep2018-v1/MINIAOD	317080-319310
	/SingleMuon/Run2018C-17Sep2018-v1/MINIAOD	319337-320065
	/SingleMuon/Run2018D-PromptReco-v2/MINIAOD	320500-325175

Table A.3: Data sets used in the  $h \rightarrow aa \rightarrow bb\tau\tau$  analysis for the 2018 eras.

Channel	Embedded samples (2016)
$e\mu$	/EmbeddingRun2016B/ElMuFinalState-inputDoubleMu_94X_Legacy_miniAOD-v5
	/EmbeddingRun2016C/ElMuFinalState-inputDoubleMu_94X_Legacy_miniAOD-v5
	/EmbeddingRun2016D/ElMuFinalState-inputDoubleMu_94X_Legacy_miniAOD-v5
	/EmbeddingRun2016E/ElMuFinalState-inputDoubleMu_94X_Legacy_miniAOD-v5
	/EmbeddingRun2016F/ElMuFinalState-inputDoubleMu_94X_Legacy_miniAOD-v5
	/EmbeddingRun2016G/ElMuFinalState-inputDoubleMu_94X_Legacy_miniAOD-v5
	/EmbeddingRun2016H/ElMuFinalState-inputDoubleMu_94X_Legacy_miniAOD-v5
$e\tau_h$	/EmbeddingRun2016B/ElTauFinalState-inputDoubleMu_94X_Legacy_miniAOD-v5
	/EmbeddingRun2016C/ElTauFinalState-inputDoubleMu_94X_Legacy_miniAOD-v5
	/EmbeddingRun2016D/ElTauFinalState-inputDoubleMu_94X_Legacy_miniAOD-v5
	/EmbeddingRun2016E/ElTauFinalState-inputDoubleMu_94X_Legacy_miniAOD-v5
	/EmbeddingRun2016F/ElTauFinalState-inputDoubleMu_94X_Legacy_miniAOD-v5
	/EmbeddingRun2016G/ElTauFinalState-inputDoubleMu_94X_Legacy_miniAOD-v5
	/EmbeddingRun2016H/ElTauFinalState-inputDoubleMu_94X_Legacy_miniAOD-v5
$\mu\tau_h$	/EmbeddingRun2016B/MuTauFinalState-inputDoubleMu_94X_Legacy_miniAOD-v5
	/EmbeddingRun2016C/MuTauFinalState-inputDoubleMu_94X_Legacy_miniAOD-v5
	/EmbeddingRun2016D/MuTauFinalState-inputDoubleMu_94X_Legacy_miniAOD-v5
	/EmbeddingRun2016E/MuTauFinalState-inputDoubleMu_94X_Legacy_miniAOD-v5
	/EmbeddingRun2016F/MuTauFinalState-inputDoubleMu_94X_Legacy_miniAOD-v5
	/EmbeddingRun2016G/MuTauFinalState-inputDoubleMu_94X_Legacy_miniAOD-v5
	/EmbeddingRun2016H/MuTauFinalState-inputDoubleMu_94X_Legacy_miniAOD-v5

Table A.4: Embedded samples used in the analysis for the 2016 era.

Channel	Embedded samples (2017)
$e\mu$	/EmbeddingRun2017B/ElMuFinalState-inputDoubleMu_94X_miniAOD-v2 /EmbeddingRun2017C/ElMuFinalState-inputDoubleMu_94X_miniAOD-v2 /EmbeddingRun2017D/ElMuFinalState-inputDoubleMu_94X_miniAOD-v2 /EmbeddingRun2017E/ElMuFinalState-inputDoubleMu_94X_miniAOD-v2 /EmbeddingRun2017F/ElMuFinalState-inputDoubleMu_94X_miniAOD-v2
$e\tau_h$	/EmbeddingRun2017B/ElTauFinalState-inputDoubleMu_94X_miniAOD-v2 /EmbeddingRun2017C/ElTauFinalState-inputDoubleMu_94X_miniAOD-v2 /EmbeddingRun2017D/ElTauFinalState-inputDoubleMu_94X_miniAOD-v2 /EmbeddingRun2017E/ElTauFinalState-inputDoubleMu_94X_miniAOD-v2 /EmbeddingRun2017F/ElTauFinalState-inputDoubleMu_94X_miniAOD-v2
$\mu\tau_h$	/EmbeddingRun2017B/MuTauFinalState-inputDoubleMu_94X_miniAOD-v2 /EmbeddingRun2017C/MuTauFinalState-inputDoubleMu_94X_miniAOD-v2 /EmbeddingRun2017D/MuTauFinalState-inputDoubleMu_94X_miniAOD-v2 /EmbeddingRun2017E/MuTauFinalState-inputDoubleMu_94X_miniAOD-v2 /EmbeddingRun2017F/MuTauFinalState-inputDoubleMu_94X_miniAOD-v2

Table A.5: Embedded samples used in the analysis for the 2017 era.

Channel	Embedded samples (2018)
$e\mu$	/EmbeddingRun2018A/ElMuFinalState-inputDoubleMu_102X_miniAOD-v1 /EmbeddingRun2018B/ElMuFinalState-inputDoubleMu_102X_miniAOD-v1 /EmbeddingRun2018C/ElMuFinalState-inputDoubleMu_102X_miniAOD-v1 /EmbeddingRun2018D/ElMuFinalState-inputDoubleMu_102X_miniAOD-v1
$e\tau_h$	/EmbeddingRun2018A/ElTauFinalState-inputDoubleMu_102X_miniAOD-v1 /EmbeddingRun2018B/ElTauFinalState-inputDoubleMu_102X_miniAOD-v1 /EmbeddingRun2018C/ElTauFinalState-inputDoubleMu_102X_miniAOD-v1 /EmbeddingRun2018D/ElTauFinalState-inputDoubleMu_102X_miniAOD-v1
$\mu\tau_h$	/EmbeddingRun2018A/MuTauFinalState-inputDoubleMu_102X_miniAOD-v1 /EmbeddingRun2018B/MuTauFinalState-inputDoubleMu_102X_miniAOD-v1 /EmbeddingRun2018C/MuTauFinalState-inputDoubleMu_102X_miniAOD-v1 /EmbeddingRun2018D/MuTauFinalState-inputDoubleMu_102X_miniAOD-v1

Table A.6: Embedded samples used in the analysis for the 2018 era.

Process	Simulated background samples (2016)	Cross section (pb)
DY	/DY1JetsToLL_M-50_TuneCUETP8M1	1012.5 (LO)
	/DY2JetsToLL_M-50_TuneCUETP8M1	332.8 (LO)
	/DY3JetsToLL_M-50_TuneCUETP8M1	101.8 (LO)
	/DY4JetsToLL_M-50_TuneCUETP8M1	54.8 (LO)
	/DYJetsToLL_M-50_TuneCUETP8M1	4963.0 (LO)
	/DY1JetsToLL_M-10to50_TuneCUETP8M1	730.3 (LO)
	/DY2JetsToLL_M-10to50_TuneCUETP8M1	387.4 (LO)
	/DY3JetsToLL_M-10to50_TuneCUETP8M1	95.0 (LO)
	/DY4JetsToLL_M-10to50_TuneCUETP8M1	36.7 (LO)
	/DYJetsToLL_M-10to50_TuneCUETP8M1	16290.0 (LO)
Top	/TTTo2L2Nu_TuneCP5_PSweights	88.29
	/TTToHadronic_TuneCP5_PSweights	377.96
	/TTToSemiLeptonic_TuneCP5_PSweights	365.35
	/ST_t-channel_antitop_4f_inclusiveDecays <sup>†</sup>	26.23
	/ST_t-channel_top_4f_inclusiveDecays <sup>†</sup>	44.07
	/ST_tW_antitop_5f_inclusiveDecays_TuneCUETP8M1	35.6
	/ST_tW_top_5f_inclusiveDecays_TuneCUETP8M1	35.6
VV	/VVTTo2L2Nu_13TeV_amcatnloFXFX_madspin_pythia8	13.84
	/WZTo2L2Q_13TeV_amcatnloFXFX_madspin_pythia8	5.52
	/WZTo3LNu_TuneCUETP8M1_13TeV-amcatnloFXFX-pythia8	4.43
	/ZZTo2L2Q_13TeV_amcatnloFXFX_madspin_pythia8	3.38
	/ZZTo4L_13TeV-amcatnloFXFX-pythia8	1.212
W	/W1JetsToLNu_TuneCUETP8M1	8104.0 (LO)
	/W2JetsToLNu_TuneCUETP8M1	2793.0 (LO)
	/W3JetsToLNu_TuneCUETP8M1	992.5 (LO)
	/W4JetsToLNu_TuneCUETP8M1	544.3 (LO)
	/WJetsToLNu_TuneCUETP8M1	52940.0 (LO)
H	/GluGluHToTauTau_M125	48.58*0.0627
	/GluGluHToWWTo2L2Nu_M125	48.58*0.2137*0.3258*0.3258
	/GluGluZH_HToWW_M125	0.1227*0.2137
	/HWminusJ_HToWW_M125	0.5328*0.2137
	/HWplusJ_HToWW_M125	0.840*0.2137
	/HZJ_HToWW_M125	0.7612*0.2137
	/VBFHToTauTau_M125	3.782*0.0627
	/VBFHToWWTo2L2Nu_M125	3.782*0.2137*0.3258*0.3258
	/WminusHToTauTau_M125	0.5328*0.0627
	/WplusHToTauTau_M125	0.840*0.0627
	/ZHToTauTau_M125	0.7612*0.0627
	/ggZH_HToTauTau_ZToLL_M125	0.1227*0.0627*3*0.033658
	/ggZH_HToTauTau_ZToNuNu_M125	0.1227*0.0627*0.2000
	/ggZH_HToTauTau_ZToQQ_M125	0.1227*0.0627*0.6991
	/ttHToNonbb_M125_TuneCUETP8M2_ttHtranche3	0.5071*(1-0.5824)
	/ttHTobb_M125_TuneCP5	0.5071*0.5824

Table A.7: Background MC samples used in the analysis for the 2016 era. Samples marked with a <sup>†</sup> are generated with the powhegV2-madspin-pythia8 tag.

Process	Simulated background samples (2017)	Cross section (pb)
DY	DY1JetsToLL_M-50_TuneCP5	877.8 (LO)
	DY2JetsToLL_M-50_TuneCP5	304.4 (LO)
	DY3JetsToLL_M-50_TuneCP5	111.5 (LO)
	DY4JetsToLL_M-50_TuneCP5	44.0 (LO)
	DYJetsToLL_M-50_TuneCP5	5343.0 (LO)
	DYJetsToLL_M-10to50_TuneCP5	15810.0 (LO)
Top	TTTo2L2Nu_TuneCP5	88.29
	TTToHadronic_TuneCP5	377.96
	TTToSemileptonic_TuneCP5	365.35
	ST_t-channel_antitop_4f_inclusiveDecays_TuneCP5 <sup>†</sup>	80.94
	ST_t-channel_top_4f_inclusiveDecays_TuneCP5 <sup>†</sup>	136.02
	ST_tW_antitop_5f_inclusiveDecays_TuneCP5	35.85
	ST_tW_top_5f_inclusiveDecays_TuneCP5	35.85
VV	VVTo2L2Nu_13TeV_amcatnloFXFX_madspin_pythia8	13.84
	WZTo2L2Q_13TeV_amcatnloFXFX_madspin_pythia8	5.52
	WZTo3LNu_TuneCP5_13TeV-amcatnloFXFX-pythia8	4.43
	ZZTo2L2Q_13TeV_amcatnloFXFX_madspin_pythia8	3.38
	ZZTo4L_TuneCP5_13TeV-amcatnloFXFX-pythia8	1.212
W	W1JetsToLNu_TuneCP5	8104.0 (LO)
	W2JetsToLNu_TuneCP5	2793.0 (LO)
	W3JetsToLNu_TuneCP5	992.5 (LO)
	W4JetsToLNu_TuneCP5	544.3 (LO)
	WJetsToLNu_TuneCP5	52940.0 (LO)
H	GluGluHToTauTau_M125	48.58*0.0627
	GluGluHToWWTo2L2Nu_M125 <sup>††</sup>	48.58*0.2137*0.3258*0.3258
	GluGluZH_HToWW_M125	0.1227*0.2137
	HWminusJ_HToWW_M125	0.5328*0.2137
	HWplusJ_HToWW_M125	0.840*0.2137
	HZJ_HToWW_M125 <sup>††</sup>	0.7612*0.2137
	VBFHToTauTau_M125	3.782*0.0627
	VBFHToWWTo2L2Nu_M125 <sup>††</sup>	3.782*0.2137*0.3258*0.3258
	WminusHToTauTau_M125	0.5328*0.0627
	WplusHToTauTau_M125	0.840*0.0627
	ZHToTauTau_M125	0.7612*0.0627
	ggZH_HToTauTau_ZToLL_M125	0.1227*0.0627*3*0.033658
	ggZH_HToTauTau_ZToNuNu_M125	0.1227*0.0627*0.2000
	ggZH_HToTauTau_ZToQQ_M125	0.1227*0.0627*0.6991
	ttHToNonbb_M125_TuneCP5	0.5071*(1-0.5824)
	ttHTobb_M125_TuneCP5	0.5071*0.5824

Table A.8: Background MC samples used in the analysis for the 2017 era. All samples use powheg, except the DYJets and WJets samples, which use madgraphMLM. Samples marked with a <sup>†</sup>, <sup>††</sup>, or <sup>†††</sup> had the tags powhegV2-madspin-pythia8, powheg2\_JHUGenV714\_pythia8, or powheg\_jhugen724\_pythia8 respectively.

Process	Simulated background samples (2018)	Cross section (pb)
DY	DY1JetsToLL_M-50_TuneCP5	877.8 (LO)
	DY2JetsToLL_M-50_TuneCP5	304.4 (LO)
	DY3JetsToLL_M-50_TuneCP5	111.5 (LO)
	DY4JetsToLL_M-50_TuneCP5	44.0 (LO)
	DYJetsToLL_M-50_TuneCP5	5343.0 (LO)
	DYJetsToLL_M-10to50_TuneCP5	15810.0 (LO)
Top	TTTo2L2Nu_TuneCP5	88.29
	TTToHadronic_TuneCP5	377.96
	TTToSemiLeptonic_TuneCP5	365.35
	ST_t-channel_antitop_4f_InclusiveDecays_TuneCP5 <sup>†</sup>	80.94
	ST_t-channel_top_5f_TuneCP5 <sup>†</sup>	136.02
	ST_tW_antitop_5f_inclusiveDecays_TuneCP5	35.85
VV	ST_tW_top_5f_inclusiveDecays	35.85
	VVTo2L2Nu_13TeV_amcatnloFXFX_madspin	13.84
	WZTo2L2Q_13TeV_amcatnloFXFX_madspin	5.52
	WZTo3LNu_TuneCP5_13TeV-amcatnloFXFX-pythia8	4.43
	ZZTo2L2Q_13TeV_amcatnloFXFX_madspin	3.38
W	ZZTo4L_TuneCP5_13TeV-amcatnloFXFX-pythia8	1.212
	W1JetsToLNu_TuneCP5	8104.0 (LO)
	W2JetsToLNu_TuneCP5	2793.0 (LO)
	W3JetsToLNu_TuneCP5	992.5 (LO)
	W4JetsToLNu_TuneCP5	544.3 (LO)
H	WJetsToLNu_TuneCP5	52940.0 (LO)
	GluGluHToTauTau_M125	48.58*0.0627
	GluGluHToWWTo2L2Nu_M125 <sup>††</sup>	48.58*0.2137*0.3258*0.3258
	GluGluZH_HToWW_M125	0.1227*0.2137
	HWminusJ_HToWW_M125 <sup>†††</sup>	0.5328*0.2137
	HWplusJ_HToWW_M125 <sup>†††</sup>	0.840*0.2137
	HZJ_HToWW_M125 <sup>††</sup>	0.7612*0.2137
	VBFHToTauTau_M125	3.782*0.0627
	VBFHToWWTo2L2Nu_M125 <sup>†††</sup>	3.782*0.2137*0.3258*0.3258
	WminusHToTauTau_M125	0.5328*0.0627
	WplusHToTauTau_M125	0.840*0.0627
	ZHToTauTau_M125	0.7612*0.0627
	ggZH_HToTauTau_ZToLL_M125	0.1227*0.0627*3*0.033658
	ggZH_HToTauTau_ZToNuNu_M125	0.1227*0.0627*0.2000
	ggZH_HToTauTau_ZToQQ_M125	0.1227*0.0627*0.6991
	ttHTobb_M125_TuneCP5	0.5071*(1-0.5824)
	ttHTobb_M125_TuneCP5	0.5071*0.5824

Table A.9: Background Monte Carlo samples used in the analysis for the 2018 era. All samples listed are generated for 13 TeV collisions and use pythia8. All samples use powheg, except the DYJets and WJets samples, which use madgraphMLM. Samples marked with a <sup>†</sup>, <sup>††</sup>, or <sup>†††</sup>, had the tags powhegV2-madspin-pythia8, powheg2\_JHUGenV714\_pythia8, and powheg\_jhugen724\_pythia8 respectively.

Signal samples (2016)	# events	Filter eff.
/SUSYGluGluToHToAA_AToBB_AToTauTau_M-12_FilterTauTauTrigger	0.4M	3.81%
/SUSYGluGluToHToAA_AToBB_AToTauTau_M-15_FilterTauTauTrigger	0.4M	3.54%
/SUSYGluGluToHToAA_AToBB_AToTauTau_M-20_FilterTauTauTrigger	1M	3.37
/SUSYGluGluToHToAA_AToBB_AToTauTau_M-25_FilterTauTauTrigger	0.2M	3.56%
/SUSYGluGluToHToAA_AToBB_AToTauTau_M-30_FilterTauTauTrigger	0.2M	3.16%
/SUSYGluGluToHToAA_AToBB_AToTauTau_M-35_FilterTauTauTrigger	0.2M	3.30%
/SUSYGluGluToHToAA_AToBB_AToTauTau_M-40_FilterTauTauTrigger	1M	3.30%
/SUSYGluGluToHToAA_AToBB_AToTauTau_M-45_FilterTauTauTrigger	0.2M	3.23%
/SUSYGluGluToHToAA_AToBB_AToTauTau_M-50_FilterTauTauTrigger	0.2M	3.42%
/SUSYGluGluToHToAA_AToBB_AToTauTau_M-55_FilterTauTauTrigger	0.2M	3.65%
/SUSYGluGluToHToAA_AToBB_AToTauTau_M-60_FilterTauTauTrigger	1M	3.73
/SUSYVBFHToAA_AToBB_AToTauTau_M-12_FilterTauTauTrigger	0.2M	7.94%
/SUSYVBFHToAA_AToBB_AToTauTau_M-15_FilterTauTauTrigger	0.2M	7.38%
/SUSYVBFHToAA_AToBB_AToTauTau_M-20_FilterTauTauTrigger	0.2M	7.27%
/SUSYVBFHToAA_AToBB_AToTauTau_M-25_FilterTauTauTrigger	0.2M	7.21%
/SUSYVBFHToAA_AToBB_AToTauTau_M-30_FilterTauTauTrigger	0.2M	6.87%
/SUSYVBFHToAA_AToBB_AToTauTau_M-35_FilterTauTauTrigger	0.2M	6.80%
/SUSYVBFHToAA_AToBB_AToTauTau_M-40_FilterTauTauTrigger	0.2M	6.78%
/SUSYVBFHToAA_AToBB_AToTauTau_M-45_FilterTauTauTrigger	0.2M	6.56%
/SUSYVBFHToAA_AToBB_AToTauTau_M-50_FilterTauTauTrigger	0.2M	6.40%
/SUSYVBFHToAA_AToBB_AToTauTau_M-55_FilterTauTauTrigger	0.2M	6.54%
/SUSYVBFHToAA_AToBB_AToTauTau_M-60_FilterTauTauTrigger	0.2M	6.55%

Table A.10: Signal samples used in the analysis for the 2016 era. All belong to the RunIISummer16MiniAODv3 campaign and are produced with the tags TuneCUETP8M1\_13TeV\_madgraph\_pythia8 PUMoriond17\_94X\_mcRun2\_asymptotic\_v3. The second column is the number of events after the generator-level filter is applied, and the third column is the filter efficiency (percentage of all events that pass the generator-level filter).

Signal samples (2017)	# events	Filter eff.
/SUSYGluGluToHToAA_AToBB_AToTauTau_M-12_FilterTauTauTrigger	0.4M	3.78%
/SUSYGluGluToHToAA_AToBB_AToTauTau_M-15_FilterTauTauTrigger	0.4M	3.55%
/SUSYGluGluToHToAA_AToBB_AToTauTau_M-20_FilterTauTauTrigger	1M	3.40%
/SUSYGluGluToHToAA_AToBB_AToTauTau_M-25_FilterTauTauTrigger	0.2M	3.32%
/SUSYGluGluToHToAA_AToBB_AToTauTau_M-30_FilterTauTauTrigger	0.2M	3.36%
/SUSYGluGluToHToAA_AToBB_AToTauTau_M-35_FilterTauTauTrigger	0.2M	3.27%
/SUSYGluGluToHToAA_AToBB_AToTauTau_M-40_FilterTauTauTrigger	1M	3.03%
/SUSYGluGluToHToAA_AToBB_AToTauTau_M-45_FilterTauTauTrigger	0.2M	3.03%
/SUSYGluGluToHToAA_AToBB_AToTauTau_M-50_FilterTauTauTrigger	0.2M	3.31%
/SUSYGluGluToHToAA_AToBB_AToTauTau_M-55_FilterTauTauTrigger	0.2M	3.56%
/SUSYGluGluToHToAA_AToBB_AToTauTau_M-60_FilterTauTauTrigger	1M	3.95%
/SUSYVBFHToAA_AToBB_AToTauTau_M-12_FilterTauTauTrigger	0.2M	7.73%
/SUSYVBFHToAA_AToBB_AToTauTau_M-15_FilterTauTauTrigger	0.2M	7.35%
/SUSYVBFHToAA_AToBB_AToTauTau_M-20_FilterTauTauTrigger	0.2M	7.33%
/SUSYVBFHToAA_AToBB_AToTauTau_M-25_FilterTauTauTrigger	0.2M	7.23%
/SUSYVBFHToAA_AToBB_AToTauTau_M-30_FilterTauTauTrigger	0.2M	6.84%
/SUSYVBFHToAA_AToBB_AToTauTau_M-35_FilterTauTauTrigger	0.2M	6.97%
/SUSYVBFHToAA_AToBB_AToTauTau_M-40_FilterTauTauTrigger	0.2M	6.17%
/SUSYVBFHToAA_AToBB_AToTauTau_M-45_FilterTauTauTrigger	0.2M	6.67%
/SUSYVBFHToAA_AToBB_AToTauTau_M-50_FilterTauTauTrigger	0.2M	6.61%
/SUSYVBFHToAA_AToBB_AToTauTau_M-55_FilterTauTauTrigger	0.2M	6.51%
/SUSYVBFHToAA_AToBB_AToTauTau_M-60_FilterTauTauTrigger	0.2M	6.71%

Table A.11: Signal samples used in the analysis for the 2017 era. All belong to the RunIIFall17MiniAODv2 campaign and are produced with the tags TuneCP5\_13TeV\_madgraph\_pythia8 and PU2017\_12Apr2018\_94X\_mc2017\_realistic\_v14. The second column is the number of events after the generator-level filter is applied, and the third column is the filter efficiency (percentage of all events that pass the generator-level filter).

Signal samples (2018)	# events	Filter eff.
/SUSYGluGluToHToAA_AToBB_AToTauTau_M-12_FilterTauTauTrigger	0.4M	3.78%
/SUSYGluGluToHToAA_AToBB_AToTauTau_M-15_FilterTauTauTrigger	0.4M	3.49%
/SUSYGluGluToHToAA_AToBB_AToTauTau_M-20_FilterTauTauTrigger	1M	3.36%
/SUSYGluGluToHToAA_AToBB_AToTauTau_M-25_FilterTauTauTrigger	0.2M	3.46%
/SUSYGluGluToHToAA_AToBB_AToTauTau_M-30_FilterTauTauTrigger	0.2M	3.18%
/SUSYGluGluToHToAA_AToBB_AToTauTau_M-35_FilterTauTauTrigger	0.2M	3.28%
/SUSYGluGluToHToAA_AToBB_AToTauTau_M-40_FilterTauTauTrigger	1M	3.10%
/SUSYGluGluToHToAA_AToBB_AToTauTau_M-45_FilterTauTauTrigger	0.2M	3.21%
/SUSYGluGluToHToAA_AToBB_AToTauTau_M-50_FilterTauTauTrigger	0.2M	3.14%
/SUSYGluGluToHToAA_AToBB_AToTauTau_M-55_FilterTauTauTrigger	0.2M	3.56%
/SUSYGluGluToHToAA_AToBB_AToTauTau_M-60_FilterTauTauTrigger	1M	3.38%
/SUSYVBFHToAA_AToBB_AToTauTau_M-12_FilterTauTauTrigger	0.2M	7.78%
/SUSYVBFHToAA_AToBB_AToTauTau_M-15_FilterTauTauTrigger	0.2M	7.52%
/SUSYVBFHToAA_AToBB_AToTauTau_M-20_FilterTauTauTrigger	0.2M	6.87%
/SUSYVBFHToAA_AToBB_AToTauTau_M-25_FilterTauTauTrigger	0.2M	7.21%
/SUSYVBFHToAA_AToBB_AToTauTau_M-30_FilterTauTauTrigger	0.2M	6.51%
/SUSYVBFHToAA_AToBB_AToTauTau_M-35_FilterTauTauTrigger	0.2M	6.95%
/SUSYVBFHToAA_AToBB_AToTauTau_M-40_FilterTauTauTrigger	0.2M	6.81%
/SUSYVBFHToAA_AToBB_AToTauTau_M-45_FilterTauTauTrigger	0.2M	6.62%
/SUSYVBFHToAA_AToBB_AToTauTau_M-50_FilterTauTauTrigger	0.2M	6.56%
/SUSYVBFHToAA_AToBB_AToTauTau_M-55_FilterTauTauTrigger	0.2M	6.64%
/SUSYVBFHToAA_AToBB_AToTauTau_M-60_FilterTauTauTrigger	0.2M	6.75%

Table A.12: Signal samples used in the analysis for the 2018 era. All belong to the RunIIAutumn18MiniAOD campaign and are produced with `_TuneCP5_13TeV_madgraph_pythia8`, with the tag `102X_upgrade2018_realistic_v15`. The second column is the number of events after the generator-level filter is applied, and the third column is the filter efficiency (percentage of all events that pass the generator-level filter).

2599

# Bibliography

- 2600 [1] Paul H. Frampton. Journeys Beyond the Standard Model. 54(1):52–  
2601 52. ISSN 0031-9228. doi: 10.1063/1.1349615. URL <https://doi.org/10.1063/1.1349615>. eprint: [https://pubs.aip.org/physicstoday/article-pdf/54/1/52/11109432/52\\_1\\_online.pdf](https://pubs.aip.org/physicstoday/article-pdf/54/1/52/11109432/52_1_online.pdf).
- 2602
- 2603
- 2604 [2] Meinard Kuhlmann. Quantum Field Theory. In Edward N. Zalta and Uri Nodelman, editors, *The Stanford Encyclopedia of Philosophy*. Metaphysics Research Lab, Stanford University, Summer 2023 edition, 2023.
- 2605
- 2606
- 2607 [3] Steven Weinberg. The Making of the Standard Model. *Eur. Phys. J. C*, 34:  
2608 5–13, 2004. URL <https://cds.cern.ch/record/799984>.
- 2609
- 2610
- 2611 [4] Christopher G. Tully. *Elementary Particle Physics in a Nutshell*. Princeton University Press, Princeton, 2012. ISBN 9781400839353. doi: doi:10.1515/9781400839353. URL <https://doi.org/10.1515/9781400839353>.
- 2612
- 2613 [5] John Ellis. Higgs Physics. In *2013 European School of High-Energy Physics*, pages 117–168, 2015. doi: 10.5170/CERN-2015-004.117.
- 2614
- 2615
- 2616 [6] David Curtin, Rouven Essig, Stefania Gori, and Others. Exotic decays of the 125 GeV Higgs boson. *Phys. Rev. D*, 90:075004, Oct 2014. doi: 10.1103/PhysRevD.90.075004. URL <https://link.aps.org/doi/10.1103/PhysRevD.90.075004>.
- 2617 [7] Tania Robens, Tim Stefański, and Jonas Wittbrodt. Two-real-scalar-singlet

- 2618 extension of the SM: LHC phenomenology and benchmark scenarios. *Eur.*  
2619 *Phys. J. C*, 80(2):151, 2020. doi: 10.1140/epjc/s10052-020-7655-x.
- 2620 [8] CERN. The history of CERN, 2024. URL <https://timeline.web.cern.ch/timeline-header/89>.
- 2621
- 2622 [9] R. Schmidt. Accelerator physics and technology of the LHC. In *ROXIE: Routine*  
2623 *for the Optimiazation of Magnet X-Sections, Inverse Field Calculation and Coil*  
2624 *End Design*, pages 7–17, 1998.
- 2625 [10] J. Vollaire et al. *Linac4 design report*, volume 6/2020 of *CERN Yellow Reports: Monographs*. CERN, Geneva, 9 2020. ISBN 978-92-9083-579-0, 978-92-9083-  
2626 580-6. doi: 10.23731/CYRM-2020-006.
- 2627
- 2628 [11] Antonella Del Rosso. Aerial view of the LHC and the four major experiments.  
2629 2017. URL <https://cds.cern.ch/record/2253966>. General Photo.
- 2630 [12] ATLAS Collaboration. ATLAS: Detector and physics performance technical  
2631 design report. Volume 1. 5 1999.
- 2632 [13] CMS Collaboration. CMS Physics: Technical Design Report Volume 1: Detec-  
2633 tor Performance and Software. 2006.
- 2634 [14] L Musa. Conceptual Design Report for the Upgrade of the ALICE ITS.  
2635 Technical report, CERN, Geneva, 2012. URL <https://cds.cern.ch/record/1431539>.
- 2636
- 2637 [15] S. Amato et al. LHCb technical proposal: A Large Hadron Collider Beauty  
2638 Experiment for Precision Measurements of CP Violation and Rare Decays. 2  
2639 1998.
- 2640 [16] Werner Herr and B Muratori. Concept of luminosity. 2006. doi: 10.5170/  
2641 CERN-2006-002.361. URL <https://cds.cern.ch/record/941318>.

- 2642 [17] Olivier S. Brning and Frank Zimmerman. Parameter space for the LHC lu-  
2643 minosity upgrade. ISBN 978-3-95450-115-1. URL <https://accelconf.web.cern.ch/IPAC2012/papers/moppc005.pdf>.
- 2645 [18] CMS Collaboration. Pileup mitigation at CMS in 13 TeV data. *JINST*, 15(09):  
2646 P09018, 2020. doi: 10.1088/1748-0221/15/09/P09018.
- 2647 [19] CMS Collaboration. Measurement of the inelastic proton-proton cross section  
2648 at  $\sqrt{s} = 13$  TeV. *JHEP*, 07:161, 2018. doi: 10.1007/JHEP07(2018)161.
- 2649 [20] CMS Collaboration. High-Luminosity Large Hadron Collider (HL-LHC): Tech-  
2650 nical design report. 10/2020, 12 2020. doi: 10.23731/CYRM-2020-0010.
- 2651 [21] CMS Collaboration. The CMS Experiment at the CERN LHC. *JINST*, 3:  
2652 S08004, 2008. doi: 10.1088/1748-0221/3/08/S08004.
- 2653 [22] CMS Collaboration. Particle-flow reconstruction and global event description  
2654 with the CMS detector. *JINST*, 12(10):P10003, 2017. doi: 10.1088/1748-0221/  
2655 12/10/P10003.
- 2656 [23] V Karimki, M Mannelli, P Siegrist, H Breuker, A Caner, R Castaldi, K Freudens-  
2657 reich, G Hall, R Horisberger, M Huhtinen, and A Cattai. *The CMS tracker sys-  
2658 tem project: Technical Design Report*. Technical design report. CMS. CERN,  
2659 Geneva, 1997. URL <https://cds.cern.ch/record/368412>.
- 2660 [24] The Phase-2 Upgrade of the CMS Tracker. Technical report, CERN, Geneva,  
2661 2017. URL <https://cds.cern.ch/record/2272264>.
- 2662 [25] CMS Collaboration. CMS Technical Design Report for the Pixel Detector Up-  
2663 grade. 9 2012. doi: 10.2172/1151650.
- 2664 [26] R. L. Workman and Others. Review of particle physics. 2022:083C01. doi:  
2665 10.1093/ptep/ptac097.

- 2666 [27] CMS Technical Design Report for the Phase 1 Upgrade of the Hadron Calorime-  
2667 ter. 9 2012. doi: 10.2172/1151651.
- 2668 [28] CMS Technical Design Report for the Level-1 Trigger Upgrade. 6 2013.
- 2669 [29] S. Dasu et al. CMS. The TriDAS project. Technical design report, vol. 1: The  
2670 trigger systems. 12 2000.
- 2671 [30] Alex Tapper. The CMS Level-1 Trigger for LHC Run II. *PoS*, ICHEP2016:242,  
2672 2016. doi: 10.22323/1.282.0242.
- 2673 [31] A. Zabi, F. Beaudette, L. Cadamuro, O. Davignon, T. Romantreau, T. Strebler,  
2674 M. Cepeda, J.B. Sauvan, N. Wardle, R. Aggleton, F. Ball, J. Brooke, D. New-  
2675 bold, S. Paramesvaran, D. Smith, J. Taylor, C. Foudas, M. Baber, A. Bun-  
2676 dock, S. Breeze, M. Citron, A. Elwood, G. Hall, G. Iles, C. Laner, B. Pen-  
2677 ning, A. Rose, A. Shtipliyski, A. Tapper, I. Ojalvo, T. Durkin, K. Harder,  
2678 S. Harper, C. Shepherd-Themistocleous, A. Thea, T. Williams, S. Dasu,  
2679 L. Dodd, R. Forbes, T. Gorski, P. Klabbers, A. Levine, T. Ruggles, N. Smith,  
2680 W. Smith, A. Svetek, J. Tikalsky, and M. Vicente. The cms level-1 calorimeter  
2681 trigger for the lhc run ii. *Journal of Instrumentation*, 12(01):C01065, jan 2017.  
2682 doi: 10.1088/1748-0221/12/01/C01065. URL <https://dx.doi.org/10.1088/1748-0221/12/01/C01065>.
- 2683 [32] P. Klabbers et al. CMS level-1 upgrade calorimeter trigger prototype develop-  
2684 ment. *JINST*, 8:C02013, 2013. doi: 10.1088/1748-0221/8/02/C02013.
- 2685 [33] CMS Collaboration. The Phase-2 Upgrade of the CMS Data Acquisition and  
2686 High Level Trigger. Technical report, CERN, Geneva, 2021. URL <https://cds.cern.ch/record/2759072>. This is the final version of the document,  
2687 approved by the LHCC.

- 2690 [34] C. Foudas. The CMS Level-1 Trigger at LHC and Super-LHC. In *34th Inter-*  
2691 *national Conference on High Energy Physics*, 10 2008.
- 2692 [35] CMS Software Guide. High Level Trigger (TWiki), 2024. URL <https://twiki.cern.ch/twiki/bin/view/CMSPublic/SWGuideHighLevelTrigger>.
- 2693 [36] The Worldwide LHC Computing Grid. 2012. URL <https://cds.cern.ch/record/1997398>.
- 2694 [37] Douglas Thain, Todd Tannenbaum, and Miron Livny. Distributed computing  
2695 in practice: the Condor experience. *Concurrency and Computation: Practice*  
2696 and *Experience*, 17(2-4):323–356, 2005. doi: <https://doi.org/10.1002/cpe.938>.  
2697 URL <https://onlinelibrary.wiley.com/doi/abs/10.1002/cpe.938>.
- 2700 [38] Alexandre Zabi, Jeffrey Wayne Berryhill, Emmanuelle Perez, and Alexander D.  
2701 Tapper. The Phase-2 Upgrade of the CMS Level-1 Trigger. 2020.
- 2702 [39] Technical proposal for a MIP timing detector in the CMS experiment Phase 2  
2703 upgrade. Technical report, CERN, Geneva, 2017. URL <https://cds.cern.ch/record/2296612>.
- 2704 [40] CMS Collaboration. Search for exotic decays of the Higgs boson to a pair of  
2705 pseudoscalars in the  $\mu\mu bb$  and  $\tau\tau bb$  final states. *European Physical Journal C*,  
2706 2 2024.
- 2708 [41] CMS Collaboration. CMS luminosity measurement for the 2016 data-taking  
2709 period. CMS Physics Analysis Summary CMS-PAS-LUM-17-001, 2017. URL  
2710 <https://cds.cern.ch/record/2257069>.
- 2711 [42] CMS Collaboration. CMS luminosity measurement for the 2017 data-taking  
2712 period at  $\sqrt{s} = 13$  TeV. CMS Physics Analysis Summary CMS-PAS-LUM-17-  
2713 004, 2018. URL <https://cds.cern.ch/record/2621960>.

- 2714 [43] CMS Collaboration. CMS luminosity measurement for the 2018 data-taking  
2715 period at  $\sqrt{s} = 13$  TeV. CMS Physics Analysis Summary CMS-PAS-LUM-18-  
2716 002, 2019. URL <https://cds.cern.ch/record/2676164>.
- 2717 [44] CMS LUMI Group. CMS Luminosity Public Results (TWiki), 2024. URL  
2718 <https://twiki.cern.ch/twiki/bin/view/CMSPublic/LumiPublicResults>.
- 2719 [45] J. Alwall, R. Frederix, S. Frixione, et al. The automated computation of tree-  
2720 level and next-to-leading order differential cross sections, and their matching  
2721 to parton shower simulations. *Journal of High Energy Physics*, 2014(7), July  
2722 2014. ISSN 1029-8479. doi: 10.1007/jhep07(2014)079. URL [http://dx.doi.org/10.1007/JHEP07\(2014\)079](http://dx.doi.org/10.1007/JHEP07(2014)079).
- 2723
- 2724 [46] R. Frederix, S. Frixione, V. Hirschi, et al. The automation of next-to-leading  
2725 order electroweak calculations. *Journal of High Energy Physics*, 2018(7), July  
2726 2018. ISSN 1029-8479. doi: 10.1007/jhep07(2018)185. URL [http://dx.doi.org/10.1007/JHEP07\(2018\)185](http://dx.doi.org/10.1007/JHEP07(2018)185).
- 2727
- 2728 [47] S. Agostinelli, J. Allison, K. Amako, et al. Geant4 - a simulation toolkit. 506(3):  
2729 250–303. ISSN 0168-9002. doi: 10.1016/S0168-9002(03)01368-8. URL <https://www.sciencedirect.com/science/article/pii/S0168900203013688>.
- 2730
- 2731 [48] CMS Collaboration. An embedding technique to determine  $\tau\tau$  backgrounds  
2732 in proton-proton collision data. *JINST*, 14(06):P06032, 2019. doi: 10.1088/  
2733 1748-0221/14/06/P06032.
- 2734
- 2735 [49] CMS Collaboration. Search for neutral MSSM Higgs bosons decaying to a pair  
of tau leptons in pp collisions. *JHEP*, 10:160, 2014. doi: 10.1007/JHEP10(2014)  
2736 160.
- 2737 [50] CMS Collaboration. Measurements of Higgs boson production in the decay

- 2738 channel with a pair of  $\tau$  leptons in proton-proton collisions at  $\sqrt{s} = 13$  TeV.  
2739 *Eur. Phys. J. C*, 83(7):562, 2023. doi: 10.1140/epjc/s10052-023-11452-8.
- 2740 [51] CMS Collaboration. Reconstruction and identification of tau lepton decays to  
2741 hadrons and tau neutrinos at CMS. *Journal of Instrumentation*, 11(01):P01019–  
2742 P01019, January 2016. ISSN 1748-0221. doi: 10.1088/1748-0221/11/01/p01019.  
2743 URL <http://dx.doi.org/10.1088/1748-0221/11/01/P01019>.
- 2744 [52] CMS Collaboration. Performance of  $\tau$ -lepton reconstruction and identification  
2745 in CMS. *Journal of Instrumentation*, 7(01):P01001, jan 2012. doi: 10.1088/  
2746 1748-0221/7/01/P01001. URL <https://dx.doi.org/10.1088/1748-0221/7/01/P01001>.
- 2748 [53] CMS Collaboration. Performance of reconstruction and identification of  $\tau$  lep-  
2749 tons decaying to hadrons and  $\nu_\tau$  in pp collisions at  $\sqrt{s} = 13$  TeV. *JINST*, 13  
2750 (10):P10005, 2018. doi: 10.1088/1748-0221/13/10/P10005.
- 2751 [54] CMS Collaboration. Identification of hadronic tau lepton decays using a deep  
2752 neural network. *JINST*, 17:P07023, 2022. doi: 10.1088/1748-0221/17/07/  
2753 P07023.
- 2754 [55] CMS Collaboration. Performance of CMS muon reconstruction in pp collision  
2755 events at  $\sqrt{s} = 7$  TeV. *Journal of Instrumentation*, 7(10):P10002–P10002,  
2756 October 2012. ISSN 1748-0221. doi: 10.1088/1748-0221/7/10/p10002. URL  
2757 <http://dx.doi.org/10.1088/1748-0221/7/10/P10002>.
- 2758 [56] CMS Collaboration. Performance of electron reconstruction and selection with  
2759 the CMS detector in proton-proton collisions at  $\sqrt{s} = 8$  TeV. *Journal of Instru-*  
2760 *mentation*, 10(06):P06005, 2015. doi: 10.1088/1748-0221/10/06/P06005. URL  
2761 <https://dx.doi.org/10.1088/1748-0221/10/06/P06005>.

- 2762 [57] CMS Collaboration. Identification of b-quark jets with the CMS experiment.  
2763 *Journal of Instrumentation*, 8(04):P04013–P04013, April 2013. ISSN 1748-  
2764 0221. doi: 10.1088/1748-0221/8/04/p04013. URL <http://dx.doi.org/10.1088/1748-0221/8/04/P04013>.
- 2765  
2766 [58] CMS Collaboration. Pileup Removal Algorithms. Technical report, CERN,  
2767 Geneva, 2014. URL <https://cds.cern.ch/record/1751454>.
- 2768 [59] CMS Collaboration. CMS Phase 1 heavy flavour identification performance and  
2769 developments. 2017. URL <https://cds.cern.ch/record/2263802>.
- 2770 [60] CMS Collaboration. Performance of the DeepJet b tagging algorithm using  
2771  $41.9 \text{ fb}^{-1}$  of data from proton-proton collisions at 13 TeV with Phase 1 CMS  
2772 detector. 2018. URL <https://cds.cern.ch/record/2646773>.
- 2773 [61] Lorenzo Bianchini, John Conway, Evan Klose Friis, and Christian Veelken. Re-  
2774 construction of the Higgs mass in  $H \rightarrow \tau\tau$  Events by Dynamical Likelihood  
2775 techniques. *Journal of Physics: Conference Series*, 513(2):022035, jun 2014.  
2776 doi: 10.1088/1742-6596/513/2/022035. URL <https://dx.doi.org/10.1088/1742-6596/513/2/022035>.
- 2777  
2778 [62] CMS Collaboration. Evidence for the 125 GeV Higgs boson decaying to a pair  
2779 of  $\tau$  leptons. *JHEP*, 05:104, 2014. doi: 10.1007/JHEP05(2014)104.
- 2780 [63] CMS Collaboration. Missing transverse energy performance of the CMS detec-  
2781 tor. *JINST*, 6:P09001, 2011. doi: 10.1088/1748-0221/6/09/P09001.
- 2782 [64] Artur Kalinowski. CMS AN-19-032 (internal): Reconstruction of a  $\tau$  pair in-  
2783 variant mass with a simplified likelihood scan, 2019.
- 2784 [65] CMS TAU POG. Tau Physics Object Group: Tau ID Recommendation

- 2785       For Run 2, 2024. URL <https://twiki.cern.ch/twiki/bin/view/CMS/TauIDRecommendationForRun2>.
- 2787       [66] CMS MUO POG. Muon Physics Object Group: Recommendations, 2024. URL  
2788           <https://twiki.cern.ch/twiki/bin/view/CMS/MuonPOG>.
- 2789       [67] CMS MUO POG. Muon Physics Object Group: Reference guidelines and results  
2790           for muon momentum scale and resolution in Run II, 2024. URL <https://twiki.cern.ch/twiki/bin/view/CMS/MuonReferenceScaleResolRun2>.
- 2792       [68] CMS HTT working group. Higgs To Tau Tau Working TWiki for the full Run-  
2793           2 legacy analysis, 2024. URL <https://twiki.cern.ch/twiki/bin/view/CMS/HiggsToTauTauWorkingLegacyRun2>.
- 2795       [69] CMS ELE POG. Electron Physics Object Group: Recommendations,  
2796           2024. URL <https://twiki.cern.ch/twiki/bin/view/CMS/EgammaRunIIRecommendations>.
- 2798       [70] CMS ELE POG. Electron Physics Object Group: Recommendations for  
2799           2016 to 2018 UL, 2024. URL <https://twiki.cern.ch/twiki/bin/view/CMS/EgammaUL2016To2018>.
- 2801       [71] CMS TAU Embedding Group. Tau embedded samples using 2016  
2802           data, 2024. URL <https://twiki.cern.ch/twiki/bin/view/CMS/TauTauEmbeddingSamples2016Legacy>.
- 2804       [72] CMS TAU Embedding Group. Tau embedded samples using 2017  
2805           data, 2024. URL <https://twiki.cern.ch/twiki/bin/viewauth/CMS/TauTauEmbeddingSamples2017>.
- 2807       [73] CMS TAU Embedding Group. Tau embedded samples using 2018

- 2808 data, 2024. URL <https://twiki.cern.ch/twiki/bin/viewauth/CMS/>  
2809 TauTauEmbeddingSamples2018.
- 2810 [74] Tau Lepton Run 2 Trigger Performance. 2019. URL <https://cds.cern.ch/record/2678958>.
- 2811  
2812 [75] CMS Taus High Level Trigger Studies. Tau Lepton Run 2 Trigger Performance  
2813 (CMS DP-2019/012), 2024. URL <https://twiki.cern.ch/twiki/bin/view/CMSPublic/HLTauAllRun2>.
- 2814  
2815 [76] Muon HLT Performance with 2018 Data. 2018. URL <https://cds.cern.ch/record/2627469>.
- 2816  
2817 [77] Single and Double Electron Trigger Efficiencies using the full Run 2 dataset.  
2818 2020. URL <https://cds.cern.ch/record/2888577>.
- 2819 [78] Run II Trigger Performance For  $e\mu$  Triggers. 2019. URL <https://cds.cern.ch/record/2687013>.
- 2820  
2821 [79] Performance of electron and photon reconstruction in Run 2 with the CMS  
2822 experiment. 2020. URL <https://cds.cern.ch/record/2725004>.
- 2823 [80] CMS Collaboration. Performance of the CMS muon detector and muon recon-  
2824 struction with proton-proton collisions at  $\sqrt{s} = 13$  TeV. *JINST*, 13(06):P06015,  
2825 2018. doi: 10.1088/1748-0221/13/06/P06015.
- 2826 [81] Piet Verwilligen. Muons in the cms high level trigger system. *Nuclear  
2827 and Particle Physics Proceedings*, 273-275:2509–2511, 2016. ISSN 2405-6014.  
2828 doi: <https://doi.org/10.1016/j.nuclphysbps.2015.09.441>. URL <https://www.sciencedirect.com/science/article/pii/S240560141500930X>. 37th Inter-  
2829 national Conference on High Energy Physics (ICHEP).
- 2830

- 2831 [82] Muon tracking performance in the CMS Run-2 Legacy data using the tag-and-  
2832 probe technique. 2020. URL <https://cds.cern.ch/record/2724492>.
- 2833 [83] V.M. Abazov, B. Abbott, M. Abolins, et al. A novel method for modeling  
2834 the recoil in W boson events at hadron colliders. *Nuclear Instruments and*  
2835 *Methods in Physics Research Section A: Accelerators, Spectrometers, Detectors*  
2836 *and Associated Equipment*, 609(2):250–262, 2009. ISSN 0168-9002. doi: <https://doi.org/10.1016/j.nima.2009.08.056>. URL <https://www.sciencedirect.com/science/article/pii/S0168900209016623>.
- 2839 [84] CMS Collaboration. Search for an exotic decay of the Higgs boson to a pair of  
2840 light pseudoscalars in the final state with two b quarks and two  $\tau$  leptons in  
2841 proton-proton collisions at  $\sqrt{s} = 13$  TeV. *Phys. Lett. B*, 785:462, 2018. doi:  
2842 [10.1016/j.physletb.2018.08.057](https://doi.org/10.1016/j.physletb.2018.08.057).
- 2843 [85] CMS LUMI POG. Luminosity Physics Object Group: Recommendations, 2024.  
2844 URL <https://twiki.cern.ch/twiki/bin/view/CMS/TWikiLUM>.
- 2845 [86] The modeling of the top quark  $p_T$  (TWiki), 2024. URL <https://twiki.cern.ch/twiki/bin/view/CMS/TopPtReweighting>.
- 2847 [87] CMS BTV group. Methods to apply b-tagging efficiency scale fac-  
2848 tors (TWiki), 2024. URL <https://twiki.cern.ch/twiki/bin/view/CMS/BTagShapeCalibration>.
- 2850 [88] CMS Collaboration. Jet energy scale and resolution in the CMS experiment in  
2851 pp collisions at 8 TeV. *JINST*, 12(02):P02014, 2017. doi: [10.1088/1748-0221/12/02/P02014](https://doi.org/10.1088/1748-0221/12/02/P02014).
- 2853 [89] Garvita Agarwal. Jet Energy Scale and Resolution Measurements in CMS. *PoS*,  
2854 ICHEP2022:652, 2022. doi: [10.22323/1.414.0652](https://doi.org/10.22323/1.414.0652).

- 2855 [90] CMS JERC group. Jet Energy Corrections (TWiki), 2024. URL <https://twiki.cern.ch/twiki/bin/view/CMS/JECDataMC>.
- 2856
- 2857 [91] CMS JERC group. Jet Energy Resolution (TWiki), 2024. URL <https://twiki.cern.ch/twiki/bin/view/CMS/JetResolution>.
- 2858
- 2859 [92] CMS MUO POG. Muon Physics Object Group: Baseline muon selec-
- 2860 tions for Run-II, 2024. URL <https://twiki.cern.ch/twiki/bin/view/CMS/>
- 2861 [SWGuideMuonIdRun2](#).
- 2862 [93] CMS ELE POG. Electron Identification Based on Simple Cuts, 2024. URL
- 2863 <https://twiki.cern.ch/twiki/bin/view/CMSPublic/EgammaPublicData>.
- 2864 [94] Jose Enrique Palencia Cortezon. Single top quark production at CMS. Technical
- 2865 report, CERN, Geneva, 2018. URL <https://cds.cern.ch/record/2640578>.
- 2866 [95] CMS Collaboration. Measurements of the electroweak diboson production cross
- 2867 sections in proton-proton collisions at  $\sqrt{s} = 5.02$  TeV using leptonic decays.
- 2868 *Phys. Rev. Lett.*, 127(19):191801, 2021. doi: 10.1103/PhysRevLett.127.191801.
- 2869 [96] CMS Collaboration. A portrait of the Higgs boson by the CMS experiment
- 2870 ten years after the discovery. *Nature*, 607(7917):60–68, 2022. doi: 10.1038/s41586-022-04892-x.
- 2871
- 2872 [97] CMS JERC group. Jet energy scale uncertainty sources (TWiki), 2024. URL
- 2873 <https://twiki.cern.ch/twiki/bin/view/CMS/JECUncertaintySources>.
- 2874 [98] TOP Systematic Uncertainties (Run 2) (TWiki), 2024. URL <https://twiki.cern.ch/twiki/bin/viewauth/CMS/TopSystematics>.
- 2875
- 2876 [99] Cécile Caillol, Pallabi Das, Sridhara Dasu, Pieter Everaerts, Stephanie Kwan,
- 2877 Isobel Ojalvo, and Ho-Fung Tsoi. CMS AN-20-213 (internal): Search for an

- 2878 exotic decay of the 125 GeV Higgs boson to light pseudoscalars, with a pair of  
2879 b jets and a pair of tau leptons in the final state, 2020.
- 2880 [100] Kyle Cranmer. Practical Statistics for the LHC. In *2011 European School of*  
2881 *High-Energy Physics*, pages 267–308, 2014. doi: 10.5170/CERN-2014-003.267.
- 2882 [101] Elham Khazaie, Maryam Zeinali, Hamed Bakhshiansohi, and Abideh Jafari.  
2883 CMS AN-21-058 (internal): Search for exotic decays of the Higgs boson to a  
2884 pair of new light bosons with two muons and two b jets in the final states at  
2885  $\sqrt{s} = 13$  TeV, 2021.
- 2886 [102] CMS Higgs Physics Analysis Group. Summary of 2HDM+S searches at 13 TeV  
2887 (Run 2), 2024. URL <https://twiki.cern.ch/twiki/bin/view/CMSPublic/Summary2HDMSRun2>.